Trans-Spectral Transfer of Orbital Angular Momentum and Creation of an Ultra High Density Cold Atom Trap

Graeme Walker

Submitted in fufilment of the requirements for the Degree of Doctor of Philosophy School of Physics Astronomy College of Science and Engineering University of Glasgow

July 26, 2013

Author's declaration

The work described in this Thesis was carried at the University of Glasgow under the supervision of Dr. Sonja Franke-Arnold, School of Physics and Astronomy, in the period August 2009 to February 2013. The author hereby declares that the work described in this Thesis is his own, except where specific references are made. It has not been submitted in part or in whole to any other university for a degree.

Author's signature:

.....

Graeme Walker
Glasgow, March 2013

Abstract

In recent years there has been great interest in the applications of the interaction of the phase and intensity of laser light in atomic vapours. The generation of light beams with arbitrary phase and intensity patterns can now be easily achieved by using Spatial Light Modulators (SLMs). The transformation of quantized units of phase information to atomic vapours has implications in the fields of quantum optics for the realisation of sources of entangled photons, optical switching, and quantum information storage. Spatially shaped beams with non-trivial intensity geometries have found use in single atom quantum well traps and for the enhancement of density of standard Magneto Optical Traps.

The work in this thesis is focussed around two main projects, involving the interaction of holographically shaped light beams with cold trapped atoms and with a hot atomic vapour respectively. An enhancement to the previously investigated technique of a SPontaneous force Optical Trap SPOT of ^{87}Rb is presented here which aims to solve various issues which naturally arise from compressing cold atoms in a Magneto Optical Trap (MOT) such as unavoidable heating during the compression. High density/high atom number traps are highly sought after in many experiments for more efficient transfer of atoms to Bose Einstein Condensates and for improved quantum storage capabilities in cold atom traps. The highest density achieved in our SPOT was 2.5×10^{12}atoms cm^{-3} for 2×10^8 atoms at a temperature of approximately 100μK. This represents almost 2 orders of magnitude increase in density from the standard MOT setup with no adverse heating of the trap while maintaining 75% of the atoms.

In the second part of this work hot atomic vapours are utilized for the efficient transfer of orbital angular momentum information from near infrared pump fields, driving from $5S_{1/2}$ to $5D_{5/2}$ on a two-photon transition, to a cascade from $5D_{5/2}$ to $6P_{3/2}$ to $5S_{1/2}$ generating 5230nm light and a coherent blue, 420nm, beam respecitively. This generation is performed using four wave mixing in ^{85}Rb. We observe the complete conversion of all input quantum information, the Orbital Angular Momentum (OAM) from the pump fields to the blue. In addition we show the additional phase coherence effects of this experiment through the use of simple superpositions of Laguerre-Gaussian (LG) modes showing that the process is indeed quantum in nature. A theoretical basis for the transfer of all OAM information to only the 420nm beam is also discussed here.

Acknowledgements [1]

First I would like to thank all of the staff students in the optics group at both Glasgow and Strathclyde Universities for their help and encouragement throughout the past 4 years. The wealth of knowledge throughout both groups has been an invaluable resource in the most challenging times. Especially, I owe my deepest gratitude to the people I have worked with the closest in my time here, my supervisor Dr. Sonja Franke-Arnold who gave me the opportunity to undertake this research, once fellow PhD student Dr Aline Vernier who got me started in this field, and Dr Neal Radwell who guided me into a world where Labview code is occasionally sensible.

I would like to extend my thanks to everyone who played a part in helping me over the last few years including: RIchard, Graham, Tony, Michael, Jon, Steve, Lisa, Matt, Alasdair, Thor, Aline, Martin, Bruce, Reuben, Clint, Johannes, Daniel, and Natasha to name but a few. All and many more have helped in some way ranging from their astonishing knowledge of SLMs and atom optics, to being the easiest going most Danish flatmate I've ever had, to getting the most annoying song possible stuck in my head making thesis writing seem joyful by comparison.

I owe a lifetime of gratitude to Cat who throughout the last few years has been there to listen to any and all physics problems, all of which seemed to

[1]* To be read in a Batman voice

be miraculously resolved by going to the cinema. A problem solving method I hope never fades.

Contents

1 Introduction **1**

1.1 A Brief History of Atom Optics 1

1.2 The Two-Level atom 2

1.2.1 The Susceptibility 6

1.3 Beyond the Two-Level Atom 8

1.4 Four-Wave Mixing 10

1.5 Laguerre-Gaussian Modes 11

1.6 The Work in This Thesis 13

References 15

2 Orbital Angular Momentum Theory and Generation **21**

2.1 Orbital Angular Momentum 21

2.1.1 Superpositions of Laguerre Gaussian Modes 22

2.2 Spatial Light Modulators 23

2.3 SLM Calibration 26

2.3.1 Phase Calibration 26

2.3.2 Intensity Calibration 28

References 30

3 The Magneto-Optical Trap **32**

3.1 Introduction 32

3.2 Theory 34

3.2.1 Doppler Cooling . . . 34
3.2.2 Limit of Doppler Cooling . . . 35
3.2.3 Hyperfine Structure . . . 36
3.2.4 Saturated Absorption Spectroscopy . . . 37
3.2.5 Acousto Optical Modulators AOMs . . . 41
3.2.6 The Scattering Force . . . 43
3.2.7 Zeeman Effect . . . 44
3.2.8 MOT beams - Trapping and Repump . . . 50
3.3 Fluorescence and Absorption measurements . . . 53
3.3.1 Compensation Field . . . 57
3.4 Experiment . . . 60
3.4.1 Frequency Choice of Trap and Repump . . . 60
3.4.2 MOT Temperature Measurements . . . 67
3.5 Summary . . . 68
References . . . 69

4 Dynamic Spontaneous Force Optical Trap 73
4.1 Introduction . . . 73
4.1.1 Theory of Density Limiting Regimes in the MOT . . . 78
4.2 Holograms developed for use in a dark SPOT . . . 81
4.2.1 Circle Intensity Masks . . . 87
4.3 Prediction of SPOT Shape . . . 88
4.3.1 Experimental Setup . . . 90
4.4 Measurement Technique . . . 93
4.5 SPOT Optimization . . . 97
4.5.1 Magnetic Field . . . 97
4.5.2 Depump Power . . . 98
4.5.3 Trap Frequency . . . 98
4.5.4 MOT Load Time . . . 99
4.5.5 SPOT Load Time . . . 100
4.5.6 Circle Radius and l Number . . . 102

4.6 SPOT Temperature 106
4.7 Actual fractional population in the dark state 108
4.8 Summary and Further Work 109
References 112

5 The Blue Light Experiment **115**
5.1 Introduction 115
5.2 Theory - Two-Photon Spectroscopy 119
5.3 Experiment - Gaussian Pump Beams 120
5.3.1 3D map of coherent blue output 124
5.3.2 Gaussian Pump Beams - Kerr Lensing 125
5.3.3 Negative Kerr Lensing 128
5.4 Laguerre-Gaussian Beams in the Blue Light 131
5.4.1 Kerr lensing of OAM modes 142
5.5 LG Mode Superpositions in the Blue 143
5.6 Summary 148
References 150

6 Conclusion **155**
A.1 AOM Driving Electronics and Computer Control 157

Appendix A AOM Types and Frequencies **157**

List of Figures[2]

1.1 The Two-Level Atom 2
1.2 Rabi Oscillations 4
1.3 Damped Rabi Oscillations 5
1.4 Susceptibility 7
1.5 Electromagnetically Induced Transparency 9
1.6 Absorption Profile in EIT 9
1.7 Phase Miss-Match in Four Wave Mixing 10
1.8 Pump and Output field frequencies in Four Wave Mixing . . . 11
1.9 Laguerre-Gaussian Phase and Phase Fronts 12
1.10 Laguerre-Gaussian Intensity and Phase 13

2.1 Helical Phase Fronts 21
2.2 Intensity and Phase of Superpositions of LG Modes 23
2.3 Spatial Light Modulator 24
2.4 Make up of Laguerre-Gaussian Hologram 25
2.5 General SLM Setup 26
2.6 SLM Phase Calibration Setup 27
2.7 SLM Phase Calibration Data 28
2.8 SLM Phase Calibration Data 29

3.1 Doppler Effect in Laser Cooling 35

[2]Unless otherwise stated all figures have been generated by the author.

3.2 Saturated Absorption Spectroscopy Setup 40
3.3 Acousto-Optical Modulator 42
3.4 MOT Coils and Field Lines 46
3.5 Zeeman Effect in the MOT 47
3.6 Force on an atom vs Velocity 49
3.7 Transitions in the MOT 52
3.8 MOT Setup 53
3.9 Absorption Imaging 56
3.10 MOT Setup Photo 58
3.11 Timing Sequence in MOT Absorption Imaging 59
3.12 AOM Control 60
3.13 Compensation and Quantization Fields Effect on Resonance Frequency 61
3.14 Compensation Current and Relative Absorption 62
3.15 Effect of Calibrated Compensation Field with and without Quantization 63
3.16 Double Pass AOM 65
3.17 Trap Detuning and Number of Atoms in the MOT 66
3.18 Coil Current and Number of Atoms in the MOT 66
3.19 MOT Temperature 67

4.1 Transitions in SPontaneous force Optical Trap 76
4.2 Peak Density vs Fractional Population in the Bright State . . 81
4.3 Super Laguerre-Gaussian Modes 84
4.4 Increasing Waist Super Laguerre-Gaussian Modes 85
4.5 Increasing p Component Super Laguerre-Gaussian Modes . . . 86
4.6 Combined Super Laguerre-Gaussian Mode 86
4.7 Circle Hologram and Intensity Patterns 88
4.8 Theoretical SPontaneous force Optical Trap in 2D 89
4.9 3D Theoretical SPontaneous Force Optical Trap Shape 89
4.10 SPontaneous Force Optical Trap Experimental Setup 91

4.11 SPontaneous Force Optical Trap Spatial Light Modulator Alignment . . . 92
4.12 Timing Sequence in the SPOT Experiment . . . 94
4.13 Relative Shape of SPOT and MOT . . . 96
4.14 Magnetic Field vs SPOT parameters . . . 98
4.15 Trap Frequency vs SPOT parameters . . . 99
4.16 MOT Load Time and SPOT Performance . . . 100
4.17 SPOT Load Time and Performance . . . 101
4.18 Long SPOT Load Time and Performance . . . 102
4.19 Circle Radius and SPOT Performance . . . 103
4.20 l Value $\omega = 1$ and SPOT performance . . . 105
4.21 l Value $\omega = 1.5$ and SPOT performance . . . 105
4.22 l Value $\omega = 2$ and SPOT performance . . . 106
4.23 SPOT Temperature . . . 108

5.1 Comparison Between Mach-Zehdner and Atom Interferometer 116
5.2 Transitions in Blue Light Experiment . . . 118
5.3 Two-Photon Spectroscopy in the Blue Light Experiment . . . 119
5.4 Blue Light Experimental Setup 1.0 . . . 121
5.5 Example Data of Blue Output vs 780nm Detuning . . . 123
5.6 Example Data of Two-Photon Absorption vs 776nm Detuning 124
5.7 3D Graphs of Blue Output . . . 126
5.8 Top Down View of 3D Blue Output . . . 127
5.9 Kerr Lensing . . . 128
5.10 Blue Light Experimental Setup 2.0 . . . 129
5.11 Experimental Kerr Lensing Results . . . 130
5.12 Effect of Negative Kerr Lensing . . . 131
5.13 Relative Component in Negatively Lensed Beams . . . 132
5.14 Blue Light Setup 3.0 . . . 134
5.15 Example OAM Transfer Data . . . 135
5.16 Results of OAM Conversion from $l = 0$ to 5 . . . 136

5.17 Prediction of p Component in 5.23μm beam 139
5.18 Prediction of l Component in 5.23μm beam 141
5.19 Kerr Lensing Results 143
5.20 Superposition Beams in the Blue 146

List of Tables

5.1 Input l and Number of Lobes in Output Interferogram 135
5.2 Input pump mode superpositions tested and their possible excitation paths in FWM 144
5.3 Input Superposition, Possible Excitation Paths, and Simulated Modes. 147
5.4 Excitation Paths and Simulated Modes 147

A.1 AOMs and their frequencies used throughout all Glasgow experiments 158

1 | Introduction

1.1 A Brief History of Atom Optics

Atom optics is a relatively new area of physics focussed on the study of light-atom interactions, and the effects of wave-particle duality. The field itself has blossomed in the last 3 decades with the first theoretical predictions of laser cooling [1], and following demonstrations of cooling and trapping of neutral atoms [2, 3]. The most basic and widespread trapping system, known as the Magneto-Optical Trap(MOT) and further adaptations thereof have been implemented in many different atomic elements [4, 5, 6, 7]. Many variations and further steps of cooling have been shown as a direct result of the development of the MOT such as the dark Spontaneous Force Optical Trap (dark SPOT) [8, 9], Compressed MOTs (CMOTs) [10, 11, 12], and optical dipole traps [13]. Perhaps the most famous result from the advent of laser cooling has been the development of Bose Einstein Condensates (BECs) [14, 15] predicted by Einstein and Bose in 1924 [16, 17].

More recent work in atom cooling and trapping suggests we are entering the exciting realm of miniaturization and microfabrication of MOT systems for use in electronic and computing systems [18, 19]. Other interesting developments in recent years are the development of the first atom lasers [20, 21], the many possibilities for quantum information storage in atomic systems [22, 23, 24, 25, 26] and the headline grabbing slowing of light down to 17m/s [27].

1.2 The Two-Level atom

The first step in understanding light-atom interactions is the theory of a two level atom coupled to a classical light field, using the electric dipole approximation [28]. Interaction between light and the two-level atom is typically described using a semiclassical treatment, i.e. the radiation is treated as a classical electric field but quantum mechanics is used to treat the atom. The quantized atom with two energy levels interacting with a classical light field is illustrated in Fig. 1.1. The atom has two states, a ground state, 1, and an excited state, 2, with an energy difference of $\hbar\omega_0 = \hbar(\omega_2 - \omega_1)$, are coupled by an electric dipole transition. The atom interacts with a monochromatic plane wave of frequency ω with a detuning from resonance $\Delta = \omega - \omega_0$, where ω_0 is the transition frequency.

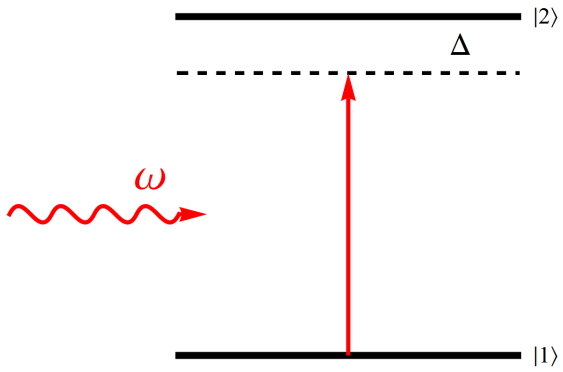

Figure 1.1: The two-level atom with levels separated by a transition with frequency ω_0. The atom is perturbed by a monochromatic plane wave of frequency ω with a detuning from resonance $\Delta = \omega - \omega_0$.

Using Dirac Ket notation to label each state the atomic wavefunction of the two states is described by

$$\Psi \mid \mathbf{r}, t\rangle = c_1 \mid 1\rangle \mathrm{e}^{-i\omega_1 t} + c_2 \mid 2\rangle \mathrm{e}^{-i\omega_2 t}, \tag{1.1}$$

where c_1 and c_2 are the time dependent coefficients describing the populations

of of each level at any one time where

$$\mid c_1 \mid^2 + \mid c_2 \mid^2 = 1. \tag{1.2}$$

The evolution of this system is governed by the time-dependent Schrödinger equation

$$\mathrm{i}\hbar \frac{\partial \Psi}{\partial t} = H\Psi, \tag{1.3}$$

where the Hamiltonian consists of two parts $H = H_0 + H_1(t)$, with H_0 being the unperturbed Hamiltonian. The perturbation caused by the oscillating electric field, $\mathbf{E} = \mathbf{E_0}\cos(\omega t)$ can be described by the Hamiltonian

$$H_1(t) = e\mathbf{r} \cdot \mathbf{E_0}\cos(\omega t), \tag{1.4}$$

where e is the elementary charge and $\mathbf{r}$ is the position of the electron with respect to the atoms centre of mass. The interaction of the atom with the external field mixes ground and excited state populations. Substitution of equation 1.1 into the time-dependent Schrödinger equation gives us, after rearranging

$$i\dot{c_1} = c_2 \left\{ \mathrm{e}^{i(\omega-\omega_0)t} + \mathrm{e}^{-\mathrm{i}(\omega+\omega_0)t} \right\} \frac{\Omega}{2}, \tag{1.5}$$

where Ω is the Rabi frequency which is defined as

$$\Omega = \frac{\langle 1 \mid e\mathbf{r} \cdot \mathbf{E_0} \mid 2 \rangle}{\hbar}. \tag{1.6}$$

The term with $(\omega + \omega_0)$ averages to 0 over typical interaction times due to very fast oscillation, this is known as the rotating wave approximation. This approximation leads to

$$
\begin{aligned}
i\dot{c_1} &= c_2 \mathrm{e}^{i(\omega-\omega_0)t}\frac{\Omega}{2}, \\
i\dot{c_2} &= c_1 \mathrm{e}^{i(\omega-\omega_0)t}\frac{\Omega*}{2}.
\end{aligned}
\tag{1.7}
$$

Combining these two gives us a second order differential equation and by solving for initial conditions, i.e. $c_1(0) = 1$ and $c_2(0) = 0$, we can arrive at the probability of an atom being in the excited state which is

$$
\mid c_2\,(t)\mid^2 = \frac{\Omega^2}{\Omega^2+\Delta^2}\sin^2\left(\frac{\sqrt{\Omega^2+\Delta^2}t}{2}\right). \tag{1.8}
$$

The population oscillates between the two levels with a frequency equal to the Rabi frequency. This population oscillation is known as Rabi Oscillations, Fig. 1.2.

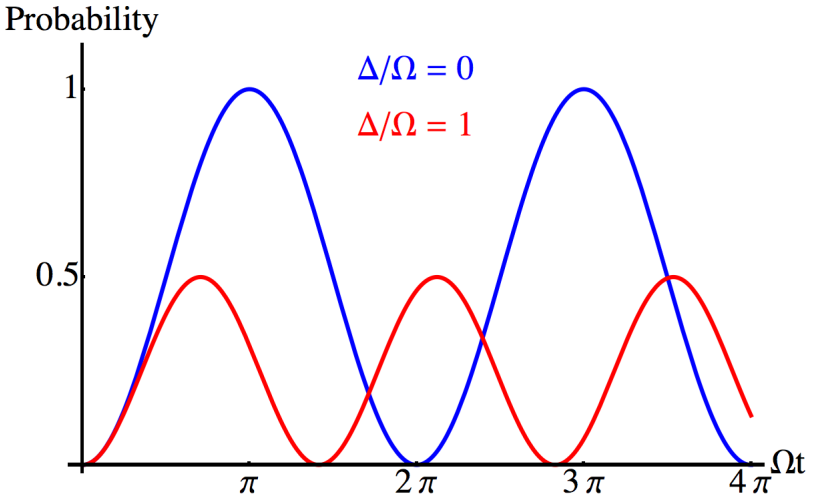

Figure 1.2: Rabi Oscillations in a two-level atom. The probability of an atom being in the excited state are shown for detunings of 0 and Ω in blue and red respectively.

The Rabi oscillations show a completely coherent behaviour in the undamped regime. In terms of energy transfer, the conservation of energy

implies that energy must be transfered to and from the driving field. The processes that exchange this energy are known as absorption and stimulated emission. In the absence of other processes an atom prepared in the excited state at $t = 0$ would remain in the excited state without an external field to drive the atom. However of course atoms have limited excited state lifetimes which decay by way of spontaneous emission which we must include to properly describe atom-light interactions. The symbol γ represents the spontaneous decay rate. By incorporating spontaneous emission into the calculation using the optical bloch equations [29] we can see that it washes out the purely coherent behaviour in Rabi Oscillations, Fig. 1.3. This approximation is correct in the strong coupling limit, i.e. $\Omega \gg \gamma$. This regime is particularly important for the study of coherent atomic interactions.

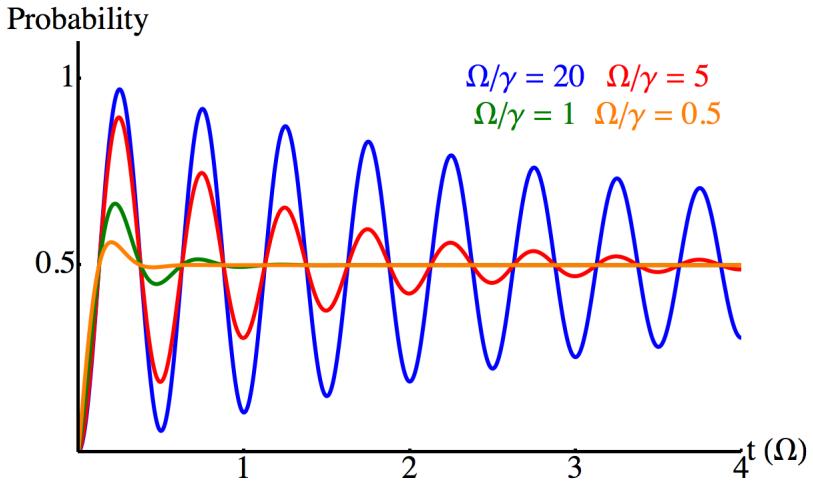

Figure 1.3: Damped Rabi oscillations for varying relative spontaneous emission rate.

1.2.1 The Susceptibility

The response of a two-level atom to an external electric field $\mathbf{E}$ can be written as,

$$\mathbf{P} = \epsilon_0 \chi(\omega) \mathbf{E}, \tag{1.9}$$

where $\mathbf{P}$ is the polarization density. The constant $\chi(\omega)$ is called the susceptibility which is the degree of polarization of the atom or dielectric material in response to the applied electric field. The susceptibility is a complex parameter the imaginary part of which describes the absorption in the material while the real part describes the dispersive properties of the material. These are of the form

$$\begin{aligned} \chi_R &= -\frac{n d_{ge}^2}{\hbar \epsilon_0} \frac{\Delta}{\Delta^2 + \Gamma^2/4 + \Omega^2/2} \\ \chi_I &= -\frac{n d_{ge}^2}{\hbar \epsilon_0} \frac{\Gamma/2}{\Delta^2 + \Gamma^2/4 + \Omega^2/2}, \end{aligned} \tag{1.10}$$

where n is the number density of the material and d_{ge} is the transition dipole moment. The real and imaginary part of the susceptibility are shown in Fig. 1.4.

The absorption takes on a Lorentzian line shape while the dispersion takes on a shape that changes sign from negative detuning to positive.

It is well known that photons have a momentum relative to their frequency of $\hbar k$ [30], which on absorption by an atom causes a corresponding change in the momentum. It is also well known that photons can carry other types of momentum such as Spin Angular Momentum (SAM) and Orbital Angular Momentum (OAM) [31]. The SAM of light is the component of angular momentum of a light beam that is associated with its circular or elliptical polarization. When a light beam is circularly polarized the photons carry

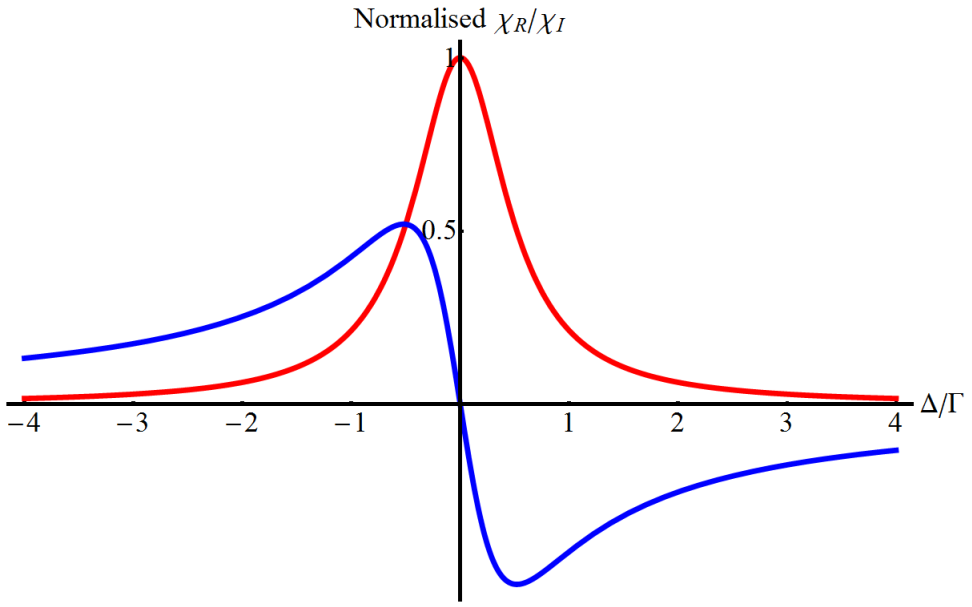

Figure 1.4: Imaginary part of Susceptibility describing absorption shown in red and real part describing dispersion shown in blue.

an angular momentum of $\pm\hbar$. Circularly polarized light may be referred to as left, σ^-, and right handed, σ^+ depending on the direction of which the electric field vector rotates with respect to the propagation direction of the light. When an atom is driven by either σ^- or σ^+ light with the atomic quantization axis aligned with the light propagation direction the light transfers both its linear momentum, $\hbar k$ and SAM, $\pm\hbar$ to the atom. If we were to treat the light field as quantized units of single photons the SAM from one photon transfers the atomic population into the transition with 1 quantized jump in angular momentum. More generally however we have classical light fields where absorption of large numbers of circularly polarized photons cause optical pumping, i.e. the SAM present transfers the atoms to the state with largest angular momentum in the direction defined by the handedness of the polarization.

It has been known for some time that light carrying Orbital Angular Mo-

mentum can also be absorbed by atoms/materials. Conservation and storage of OAM has been observed in a number of processes including the entanglement of OAM modes in Spontaneous Parametric Down Conversion (SPDC) [32, 33], second harmonic generation [34], Four-Wave Mixing (FWM) in semiconductors [35] and in setups such as Optical Tweezers [36]. In atom optics FWM and other closed loop processes have enabled the transfer of phase information to room temperature atomic vapours [37, 38] and optical OAM has been used to manipulate the quantum state of Bose-Einstein condensates via Raman transitions [39, 40]. In these setups we can observe directly the twist in momentum applied to the object. It has been shown theoretically that light carrying OAM can give rise to the violation of the standard dipolar selection rules when absorbed by matter. [41]

1.3 Beyond the Two-Level Atom

Beyond the two-level atom more complex processes appear in atoms, such as Electromagnetically Induced Transparency [42, 43]. In EIT the presence of a strong coupling field ω_c inhibits the absorption of a weak probe ω_p under the condition that one of the transitions is not dipole allowed. The 3 types of EIT setup are shown in Fig. 1.5. The 3 schemes are known as Λ-type, V-type, and cascade type respectively. In all 3 systems the probability amplitude for the atom to transfer between states can interfere destructively in order to render the atom transparent to the probe light in a very narrow frequency window as shown in Fig. 1.6.

EIT was first predicted to enhance non-linear optical processes by Harris et al in 1991 [44] and investigated experimentally by Hakuta et al.In [45] it was shown that the efficiency of four-wave mixing can be increased when the two-photon pump field in four wave mixing (FWM) becomes strong relative to the other fields. Also shown there is the effect of realistic phase matching, described by the ratio of the non-linear and linear susceptibilities,

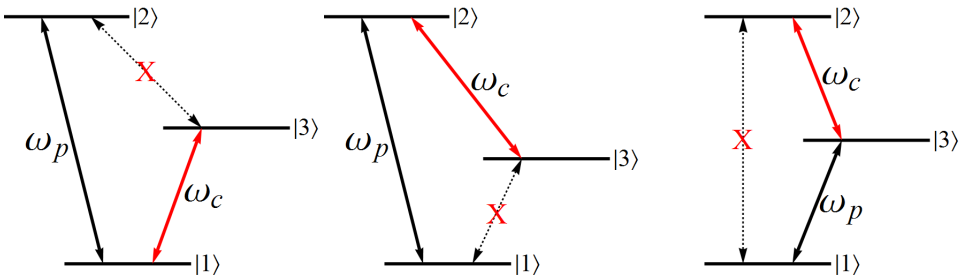

Figure 1.5: Electromagnetically Induced Transparency (EIT) setups. From Left to right: Λ-type, V -type, and cascade-type

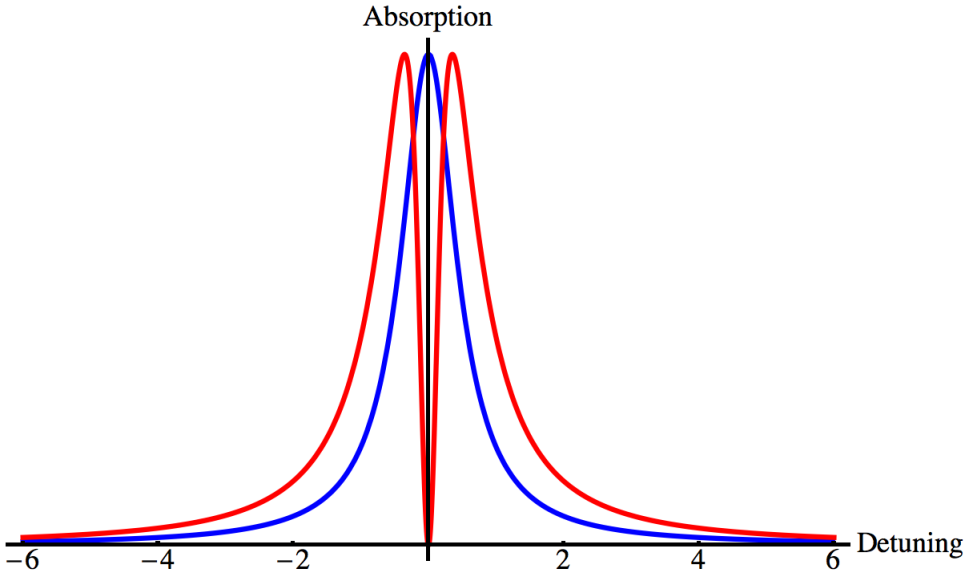

Figure 1.6: Absorption profile of the unaltered state, blue/dashed, and the absorption spectrum, red, vs frequency in units of linewidth Γ. Under EIT conditions a narrow transparency window will be seen in the absorption profile.

$|\chi^{(3)}|/|\chi^{(1)}|$. The effect of EIT in four-wave mixing is to reduce absorption on the generated transition, greatly increasing efficiency of conversion.

1.4 Four-Wave Mixing

Four-wave mixing (FWM) is a nonlinear effect which arises from the third order nonlinear susceptibility, χ^3. In FWM two or three electromagnetic fields interact within a nonlinear medium to produce four fields in total. This process along with other multi level processes such as frequency doubling, sum and difference frequency generation and parametric down conversion, are said to be phase matched[46, 47, 48, 49]. Phase matching in four wave mixing involves the constructive interference of four waves in a medium such that the four wavevectors $\{k_1, k_2, k_3, k_4\}$ multiplied by their associated refractive indices in the nonlinear medium $\{n_1, n_2, n_3, n_4\}$ is equal to zero i.e.

$$k_1 n_1 + k_2 n_2 - k_3 n_3 - k_4 n_4 = 0. \tag{1.11}$$

The above equation is the phase matching condition for four wave mixing in a nonlinear medium. Phase matching is required for high efficiency conversion from input waves to output. A phase mismatch is shown in Fig. 1.7, the efficiency of conversion/translation is determined by the phase mismatch. Only when there is no mismatch $\Delta k = 0$ do the four beams fully constructively interfere.

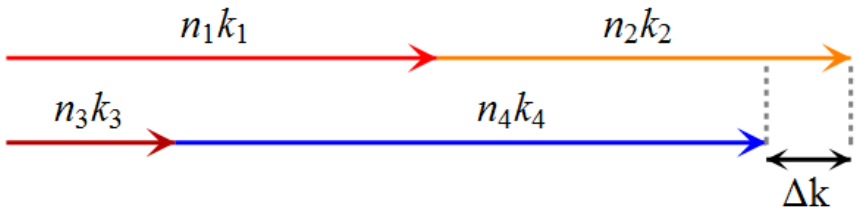

Figure 1.7: Illustration of a phase mis-match in four wave mixing.

When the input frequencies of the pump modes are the same this is called degenerate four wave mixing and when the pump modes do not match it is non-degenerate. The experiments described in this thesis are of this type. Fig 1.8 shows non-degenerate FWM in the frequency domain. Two pump

modes, ν_1 and ν_2, shown in Red and Orange interacting with a nonlinear medium produce two other modes, ν_3 and ν_4 at a lower and higher frequency respectively. These two frequencies can be vastly different from one another and from the pump light itself. Four wave mixing in ^{85}Rb can produce 5230nm and 420nm light form pump light at 780nm and 776nm.

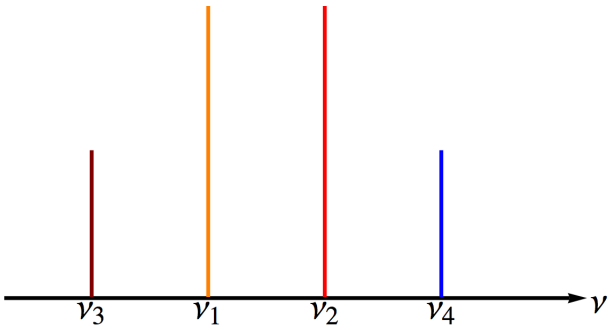

Figure 1.8: Frequency of beams involved in FWM.

1.5 Laguerre-Gaussian Modes

Laguerre-Gaussian (LG) modes are high order solutions to the paraxial approximation to the Helmholtz equation in cylindrical coordinates [50]. These modes have a rotation symmetry along the propagation axis with phase-fronts (surfaces of constant phase) which are helical in form. LG modes are defined by two indices l and p which describe the number of 2π phase cycles and the number of radial modes in the beam profile respectively, as seen in Fig. 1.10. A normalized Laguerre-Gaussian light field can be described in the cylindrical coordinate system as

$$\Phi_p^l = \sqrt{\frac{2p!}{\pi(\mid l \mid + p)!}} \frac{1}{\omega(z)} \left(\frac{\sqrt{2}r}{\omega(z)}\right)^{|l|} L_p^{|l|}\left[\frac{2r^2}{\omega^2(z)}\right] e^{il\phi} \times e^{-r^2/\omega^2} e^{+i(2p+|l|+1)\arctan(z/z_R)} e^{-ikz}. \tag{1.12}$$

Here $L_p^{|l|}$ is an associated Laguerre polynomial and $\omega(z) = \omega_0\sqrt{1+z^2/z_R^2}$ for a beam waist ω_0, with a Rayleigh range $z_R = \pi\omega_0^2/\lambda$. The l index describes not only the orbital angular momentum but also the number of time the phase cycles azimuthally from 0 to 2π in one full cycle as shown in Fig. 1.9, as such the l index is known as the azimuthal index. OAM, unlike SAM which has two modes depending on the handedness of circular polarisation, has the azimuthal index l is unbounded and can take any integer value between $-\infty$ and ∞.

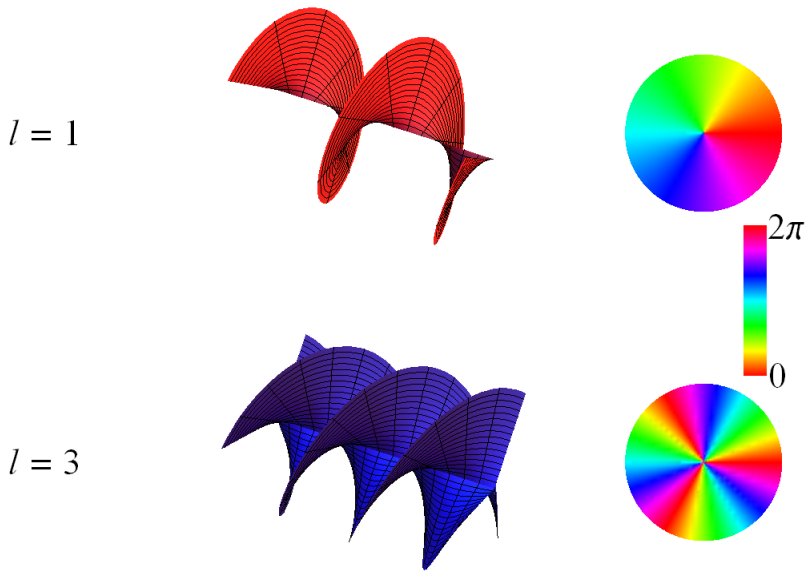

Figure 1.9: Laguerre Gaussian phase fronts and phase profile for $l = 1$ and $l = 3$.

Critically for LG modes the azimuthal rotation of phase around the beam axis leaves the phase undefined in the centre of the beam. As the phase is undefined on-axis, there is complete destructive interference at this point and an optical vortex exists in the distribution with zero intensity at the centre. This creates an intensity profile often referred to as a doughnut (when $p = 0$

and l is nonzero).

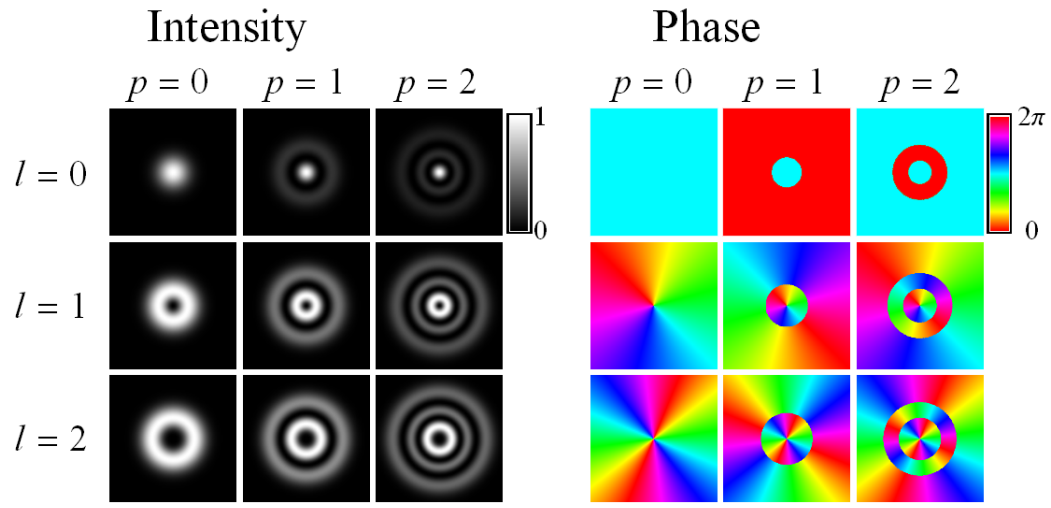

Figure 1.10: LG mode intensity and phase profiles for a number of l and p combinations.

1.6 The Work in This Thesis

The work in this thesis is focussed around two main projects outlined in chapters 4 and 5. An enhancement to the previously investigated technique of a SPontaneous force Optical Trap (SPOT) is presented here which aims to solve various issues which naturally arise from compressing cold atoms in a Magneto Optical Trap (MOT) such as unavoidable heating during the compression. High density/high atom number traps are highly sought after in many experiments for more efficient transfer of atoms to Bose Einstein Condensates and for improved quantum storage capabilities in cold atom traps. Chapter 4 will outline the steps taken to achieve an enhancement from the typical density of a MOT of 4×10^{10} atoms cm^{-3} to 2.5×10^{12}atoms cm^{-3} for 2.5×10^{8} atoms in the SPOT. This chapter will also show that

during the transition between traps the atoms are not heated and remain close to if not colder than the atoms within the MOT at a temperature of 100μK.

In the second part of this work hot atomic vapours are utilized for the efficient transfer of quantum orbital angular momentum information from near infra-red pump fields to a coherent, 420nm, beam. We observe the complete conversion of all input quantum information, the Orbital Angular Momentum (OAM) from the pump fields to the blue. In addition we show the additional phase coherence effects of this experiment through the use of simple superpositions of Laguerre-Gaussian (LG) modes showing that the process is indeed quantum in nature. A theoretical basis for the transfer of all OAM information to only the 420nm beam is also discussed here.

References

[1] T. W. Hänsch and A. L. Schawlow. Cooling of gases by laser radiation. *Optics Communications*, 13:68, January 1975.

[2] Steven Chu, L. Hollberg, J. E. Bjorkholm, Alex Cable, and A. Ashkin. Three-dimensional viscous confinement and cooling of atoms by resonance radiation pressure. *Phys. Rev. Lett.*, 55:48–51, Jul 1985.

[3] E. L. Raab, M. Prentiss, Alex Cable, Steven Chu, and D. E. Pritchard. Trapping of neutral sodium atoms with radiation pressure. *Phys. Rev. Lett.*, 59:2631–2634, Dec 1987.

[4] Antti Pietiläinen, Hanne Ludvigsen, Hannu Talvitie, and Erkki Ikonen. Observation of coherent transient effects in a magneto-optical trap. *Quantum and Semiclassical Optics: Journal of the European Optical Society Part B*, 9(4):615, 1997.

[5] C. Salomon, J. Dalibard, W. D. Phillips, A. Clairon, and S. Guellati. Laser cooling of cesium atoms below 3 μK. *EPL (Europhysics Letters)*, 12(8):683, 1990.

[6] G. Modugno, C. Benkő, P. Hannaford, G. Roati, and M. Inguscio. Sub-doppler laser cooling of fermionic ^{40}K atoms. *Phys. Rev. A*, 60:R3373–R3376, Nov 1999.

[7] Takayuki Kurosu and Fujio Shimizu. Laser cooling and trapping of calcium and strontium. *Japanese Journal of Applied Physics*, 29(Part 2, No. 11):L2127–L2129, 1990.

[8] Wolfgang Ketterle, Kendall B. Davis, Michael A. Joffe, Alex Martin, and David E. Pritchard. High densities of cold atoms in a *dark* spontaneous-force optical trap. *Phys. Rev. Lett.*, 70:2253–2256, Apr 1993.

[9] C. G. Townsend, N. H. Edwards, K. P. Zetie, C. J. Cooper, J. Rink, and C. J. Foot. High-density trapping of cesium atoms in a dark magneto-optical trap. *Phys. Rev. A*, 53:1702–1714, Mar 1996.

[10] Wolfgang Petrich, Michael H. Anderson, Jason R. Ensher, and Eric A. Cornell. Behavior of atoms in a compressed magneto-optical trap. *J. Opt. Soc. Am. B*, 11(8):1332–1335, Aug 1994.

[11] Marshall T DePue, S Lukman Winoto, D.J Han, and David S Weiss. Transient compression of a MOT and high intensity fluorescent imaging of optically thick clouds of atoms. *Optics Communications*, 180(1-3):73 – 79, 2000.

[12] L.-S. Yang, B.-T. Han, D.-S. Hong, T. A. Mohamed, and D. J. Han. Loading and Compression of a Large Number of Rubidium Atoms Using a Semi-Dark Type Magneto-Optical Trap. *Chinese Journal of Physics*, 45:606, December 2007.

[13] Rudolf Grimm, Matthias Weidemüller, and Yurii B. Ovchinnikov. Optical dipole traps for neutral atoms. volume 42 of *Advances In Atomic, Molecular, and Optical Physics*, pages 95 – 170. Academic Press, 2000.

[14] M. H. Anderson, J. R. Ensher, M. R. Matthews, C. E. Wieman, and E. A. Cornell. Observation of Bose-Einstein condensation in a dilute atomic vapor. *Science*, 269(5221):198–201, 1995.

[15] K. B. Davis, M. O. Mewes, M. R. Andrews, N. J. van Druten, D. S. Durfee, D. M. Kurn, and W. Ketterle. Bose-Einstein condensation in a gas of sodium atoms. *Phys. Rev. Lett.*, 75:3969–3973, Nov 1995.

[16] A. Einstein. Quantentheorie des einatomigen idealen Gases. *Sitzungsberichte der Preußischen Akademie der Wissenschaften*, Physikalisch-mathematische Klasse:261–267, 1924.

[17] Bose. Plancks Gesetz und Lichtquantenhypothese. *Zeitschrift fur Physik*, 26:178–181, December 1924.

[18] Matthieu Vangeleyn, Paul F. Griffin, Erling Riis, and Aidan S. Arnold. Laser cooling with a single laser beam and a planar diffractor. *Opt. Lett.*, 35(20):3453–3455, Oct 2010.

[19] Ron Folman, Peter Krúger, Jörg Schmiedmayer, Johannes Denschlag, and Carsten Henkel. Microscopic atom optics: From wires to an atom chip. volume 48 of *Advances In Atomic, Molecular, and Optical Physics*, pages 263 – 356. Academic Press, 2002.

[20] Immanuel Bloch, Theodor W. Hänsch, and Tilman Esslinger. Atom laser with a cw output coupler. *Phys. Rev. Lett.*, 82:3008–3011, Apr 1999.

[21] E. W. Hagley, L. Deng, M. Kozuma, J. Wen, K. Helmerson, S. L. Rolston, and W. D. Phillips. A well-collimated quasi-continuous atom laser. *Science*, 283(5408):1706–1709, 1999.

[22] J. Ahn, T. C. Weinacht, and P. H. Bucksbaum. Information storage and retrieval through quantum phase. *Science*, 287(5452):463–465, 2000.

[23] M. D. Lukin, M. Fleischhauer, R. Cote, L. M. Duan, D. Jaksch, J. I. Cirac, and P. Zoller. Dipole blockade and quantum information processing in mesoscopic atomic ensembles. *Phys. Rev. Lett.*, 87:037901, Jun 2001.

[24] A. B. Matsko, Y. V. Rostovtsev, O. Kocharovskaya, A. S. Zibrov, and M. O. Scully. Nonadiabatic approach to quantum optical information storage. *Phys. Rev. A*, 64:043809, Sep 2001.

[25] C. Monroe. Quantum information processing with atoms and photons. *Nature*, 416:238–246, Mar 2002.

[26] B. Julsgaard, J. Sherson, J. Ignacio Cirac, J. Fíurášek, and E. S. Polzik. Experimental demonstration of quantum memory for light. *Nature*, 432:482–486, Nov 2004.

[27] L. V. Hau, S. E. Harris, Z. Dutton, and C. H. Behroozi. Light speed reduction to 17 metres per second in an ultracold atomic gas. *Nature*, 397:594–598, Feb 1999.

[28] C. J. Foot. *Atomic Physics*. Oxford Master Series in Physics, 2004.

[29] C. J. Foot. *Atomic Physics*. Oxford Master Series in Physics, 2004.

[30] B. H. Bransden and C. J.. Joachain. *Physics of Atoms and Molecules*. Prentice Hall, 2003.

[31] B. H. Bransden and C. J.. Joachain. *Physics of Atoms and Molecules*. Prentice Hall, 2003.

[32] Gregor Weihs Alois Mair1, Alipasha Vaziri and Anton Zeilinger. Entanglement of the orbital angular momentum states of photons. *Nature*, 412(412):313–316, Jul 2001.

[33] D. P. Caetano, M. P. Almeida, P. H. Souto Ribeiro, J. A. O. Huguenin, B. Coutinho dos Santos, and A. Z. Khoury. Conservation of orbital angular momentum in stimulated down-conversion. *Phys. Rev. A*, 66:041801, Oct 2002.

[34] J. Courtial, K. Dholakia, L. Allen, and M. J. Padgett. Second-harmonic generation and the conservation of orbital angular momentum with high-order laguerre-gaussian modes. *Phys. Rev. A*, 56:4193–4196, Nov 1997.

[35] Y. Ueno, Y. Toda, S. Adachi, R. Morita, and T. Tawara. Coherent transfer of orbital angular momentum to excitons by opticalfour-wave mixing. *Opt. Express*, 17(22):20567–20574, Oct 2009.

[36] N. B. Simpson, K. Dholakia, L. Allen, and M. J. Padgett. Mechanical equivalence of spin and orbital angular momentum of light: an optical spanner. *Opt. Lett.*, 22(1):52–54, Jan 1997.

[37] R. Pugatch, M. Shuker, O. Firstenberg, A. Ron, and N. Davidson. Topological stability of stored optical vortices. *Phys. Rev. Lett.*, 98:203601, May 2007.

[38] Alberto M. Marino, Vincent Boyer, Raphael C. Pooser, and Paul D. Lett. Production of entangled imagesby four-wave mixing. *Opt. Photon. News*, 19(12):45–45, Dec 2008.

[39] M. F. Andersen, C. Ryu, Pierre Cladé, Vasant Natarajan, A. Vaziri, K. Helmerson, and W. D. Phillips. Quantized rotation of atoms from photons with orbital angular momentum. *Phys. Rev. Lett.*, 97:170406, Oct 2006.

[40] J. F. S. Brachmann, W. S. Bakr, J. Gillen, A. Peng, and M. Greiner. Inducing vortices in a bose-einstein condensate using holographically produced light beams. *Opt. Express*, 19(14):12984–12991, Jul 2011.

[41] A Picón, A Benseny, J Mompart, J R VÃązquez de Aldana, L Plaja, G F Calvo, and L Roso. Transferring orbital and spin angular momenta of light to atoms. *New Journal of Physics*, 12(8):083053, 2010.

[42] S. E. Harris. Electromagnetically induced transparency with matched pulses. *Phys. Rev. Lett.*, 70:552–555, Feb 1993.

[43] J. E. Field, K. H. Hahn, and S. E. Harris. Observation of electromagnetically induced transparency in collisionally broadened lead vapor. *Phys. Rev. Lett.*, 67:3733–3733, Dec 1991.

[44] K.-J. Boller, A. Imamolu, and S. E. Harris. Observation of electromagnetically induced transparency. *Phys. Rev. Lett.*, 66:2593–2596, May 1991.

[45] J. C. Petch, C. H. Keitel, P. L. Knight, and J. P. Marangos. Role of electromagnetically induced transparency in resonant four-wave-mixing schemes. *Phys. Rev. A.*, 53:543–561, January 1996.

[46] A. Szilagyi, A. Hordvik, and H. Schlossberg. A quasi phase matching technique for efficient optical mixing and frequency doubling. *Journal of Applied Physics*, 47(5):2025–2032, 1976.

[47] Y. Sasaki and Y. Ohmori. Phase matched sum frequency light generation in optical fibers. *Applied Physics Letters*, 39(6):466–468, 1981.

[48] F. Zernike. Temperature-dependent phase matching for far-infrared difference-frequency generation in insb. *Phys. Rev. Lett.*, 22:931–933, May 1969.

[49] Martin E. Smithers and Eugene Y. C. Lu. Quantum theory of coupled parametric down-conversion and up-conversion with simultaneous phase matching. *Phys. Rev. A*, 10:1874–1880, Nov 1974.

[50] L. Allen, M. W. Beijersbergen, R. J. C. Spreeuw, and J. P. Woerdman. Orbital angular momentum of light and the transformation of Laguerre-Gaussian laser modes. *Phys. Rev. A*, 45:8185–8189, Jun 1992.

2 | Orbital Angular Momentum Theory and Generation

2.1 Orbital Angular Momentum

In 1992 Allen et al showed that light beams with an azimuthal phase dependence of the form $e^{il\phi}$ carry an orbital angular momentum (OAM) that is completely distinct from the well known Spin Angular Momentum (SAM), $\pm\hbar$ [1]. This paper also reported that these helically phased beams, shown in Fig. 2.1, carried an OAM quantized in units of $l\hbar$ per photon.

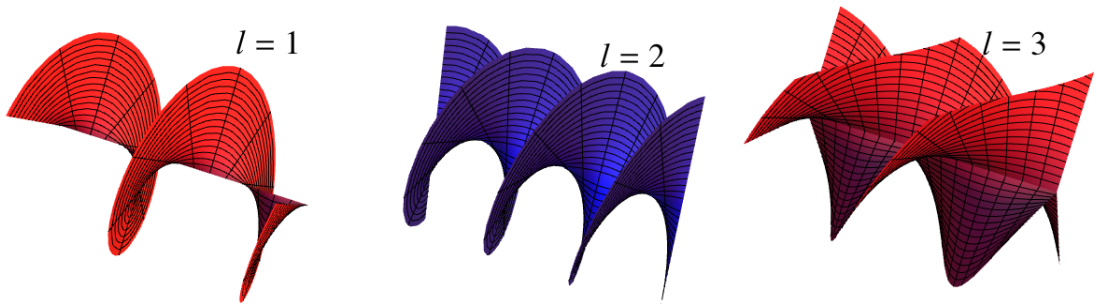

Figure 2.1: Helical Phase Fronts

A property of these helical phase fronts is that they require a phase singularity running along the centre of the beam. The phase singularity requires a

line of zero field in the intensity distribution resulting in the "doughnut" intensity pattern characteristic of Laguerre-Gaussian modes illustrated in Fig. 1.10.

LG modes are a complete basis set for paraxial light beams and are denoted by the notation Φ_p^l where p and l describe the radial and azimuthal indices of the mode. The l value is unbounded and can take any integer value between $-\infty$ and ∞. A normalized Laguerre-Gaussian light field can be described in the cylindrical coordinate system as

$$\begin{aligned}\Phi_p^l =& \sqrt{\frac{2p!}{\pi(\mid l \mid +p)!}} \frac{1}{\omega(z)} \left(\frac{\sqrt{2}r}{\omega(z)}\right)^{|l|} L_p^{|l|}\left[\frac{2r^2}{\omega^2(z)}\right] e^{il\phi} \\ & \times \mathrm{e}^{-r^2/\omega^2} e^{+i(2p+|l|+1)\arctan(z/z_R)} \mathrm{e}^{-ikz}.\end{aligned} \tag{2.1}$$

Here $L_p^{|l|}$ is an associated Laguerre polynomial and $\omega(z) = \omega_0\sqrt{1+z^2/z_R^2}$ for a beam waist ω_0, with a Rayleigh range $z_R = \pi\omega_0^2/\lambda$. A crucial factor for experiments in this thesis is the extra strength factor in the Gouy phase term of $(2p + \mid l \mid + 1)$. This stronger Gouy phase factor can have an adverse effect on achieving good beam quality.

2.1.1 Superpositions of Laguerre Gaussian Modes

When two LG modes of indices l_1 and $l_2 = l_1 + \delta l$ are perfectly overlapped the beams interfere at $\mid \delta l \mid$ azimuthal positions [2]. When two modes of the opposite l value are overlapped at an angle the intensity distribution tends to the same fork like pattern present in the phase hologram used to create LG modes [3]. If $\mid l_1 \mid \neq \mid l_2 \mid$ the radii of the intensity rings differ and dark lattices can be created. Fig. 2.2 illustrates some superpositions of LG modes with intensity and phase of the form

$$
\begin{aligned}
I &= \mid \Phi_0^{l_1} + \sqrt{l_2/l_1}\Phi_0^{l_2} \mid^2 \\
\phi &= \arg\left(\Phi_0^{l_1} + \sqrt{l_2/l_1}\Phi_0^{l_2}\right).
\end{aligned}
\tag{2.2}
$$

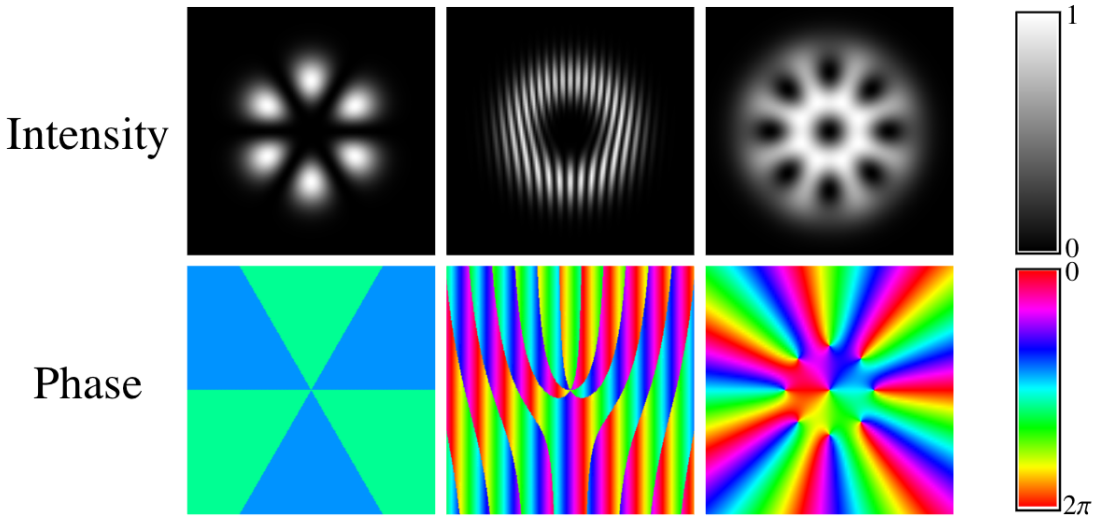

Figure 2.2: From left to right: A superposition of l = 3 and l = -3 at zero angle showing 6 bright lobes. In the centre the same superposition with the beams overlapping at an angle of 18°. On the right a superposition of l = -1 and l = 7 showing a central vortex and 8 surrounding vortexes.

2.2 Spatial Light Modulators

Both the dark SPOT and frequency translation experiments in the following chapters make use of Spatial Light Modulators (SLMs) to shape our light beams with different patterns of phase and intensity. SLMs have already been well established as invaluable tools in other fields such as in

holographic optical tweezers [4, 5]. SLMs have also been utilized in many atom optics experiments [6, 7, 8]. Here we discuss the well known steps used to generate LG beams using SLMs however this technique can be extended to the creation of more complex patterns. OAM beams can be generated in a number of ways such as with Spiral Phase Plates [9], cylindrical lens mode converters [1], or Spatial Light Modulators (SLMs) [10]. SLMs offer much greater flexibility over the other two methods and importantly are commercially available making them particularly appealing for generation of OAM modes and indeed other beams. Spatial Light Modulators are Liquid Crystal Devices (LCDs) where the phase change associated with each individual pixel can be programmed using a standard monitor cable to a computer. The spatial light modulator used in all experiments in this thesis is the Hamamatsu Liquid Crystal on Silicon (LCOS) SLM X10468-02. This SLM has a resolution of 800x600 over a 16x12mm effective area centred on 780nm.

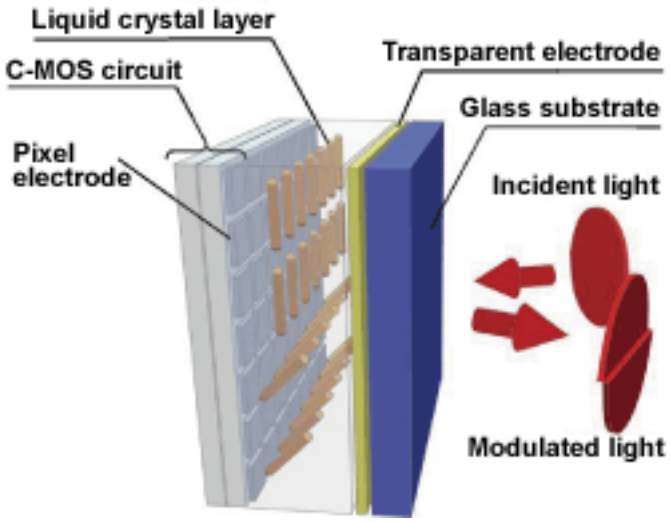

Figure 2.3: Makeup of Spatial Light Modulator. (From Hamamatsu website)

An LG beam can be created with an SLM by "displaying" the helical phase structure of the desired LG mode, as in Fig. 1.10, added to a modulated linear phase ramp between 0 and 2π on the SLM surface. The result of this

is a diffraction grating with l extra lines in one half of the grating as shown in Fig. 2.4. This is often referred to as a "fork" diffraction grating [3]. In addition to the forked diffraction pattern accurate holograms must contain the intensity mask of the desired mode, making the desired hologram the complex far-field diffraction pattern of the desired object. Defining the phase and intensity of the desired mode allows us to eliminate the contribution of higher order p modes present when illuminating a simple forked diffraction pattern with a gaussian laser mode. (A simple forked diffraction grating on its own will only create a pure Laguerre Gaussian beam free of higher order p modes under illumination of a uniform intensity distribution) Another method of generating LG beams with an SLM is by using a spiral Fresnel lens as discussed in [11].

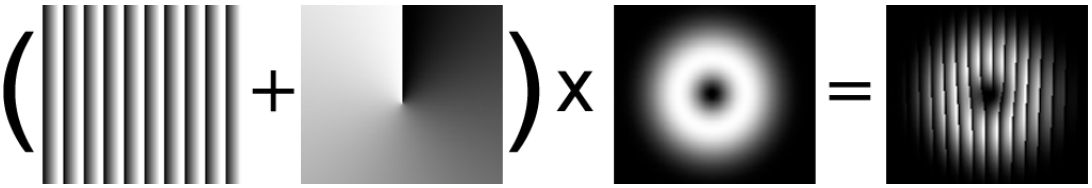

Figure 2.4: Makeup of a typical Laguerre-Gaussian Hologram for use on a spatial light modulator. The hologram consists of firstly a ramped diffraction grating between 0 and 2π which is used to separate out the desired mode/modes from the direct reflection (0th order from the grating). The ramp is then added to the phase profile of an LG mode, shown above for $l = 1$. This combination is then multiplied by the Intensity of the desired LG mode creating the final hologram shown on the right.

The desired mode output from the SLM can be optimized in any of the diffracted orders but is typically the 1st order is chosen for maximum diffraction efficiency, as shown in Fig. 2.5. The desired order is chosen using a fourier filter setup where all of the orders reflected off of the SLM are focussed by a long focal length lens with an aperture placed in the focal plane. The aperture is large enough to only let the first order beam through but small enough to block all other orders.

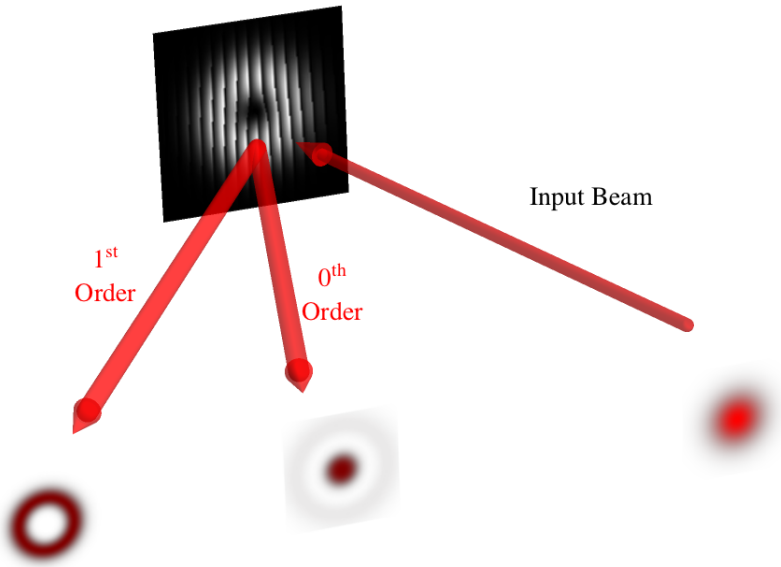

Figure 2.5: Typical setup of an SLM with an input Gaussian laser beam. The input beam diffracts off of the ramped diffraction pattern producing several diffracted orders. (2 are shown here for simplicity) The desired mode is typically chosen to be in the 1st diffracted order to maximize diffraction efficiency. In most cases many more diffraction lines are used than shown in the diagram so it is necessary to use a fourier filter setup to remove the undesired diffracted orders from the beam. (not shown here)

2.3 SLM Calibration

2.3.1 Phase Calibration

For optimum SLM operation we must determine the relationship between the SLM input from the computer, any integer value between 0 and 255, and the phase shift between 0 and 2π in the output beam. Typically commercially bought SLMs arrive with greater than 2π phase modulation possible at the desired wavelength to ensure the full range of phase shift is possible. Firstly we wish to ensure that the end points of the signal from the computer are calibrated such that they produce a maximum phase shift of 2π in the beam

(i.e. the signal from the computer should be capped somewhere below 255). Additionally we want to ensure that the modulation between 0 and 2π is linear with computer signal. Secondly any intensity mask applied over the phase pattern must also have a linear response in the output beam intensity

Our phase calibration method chosen is illustrated in Fig. 2.6. The laser beam is sent through a polarizing beam splitter and polarizer set to 45° The SLM is birefringent and will only apply a phase change to the horizontal component of the incoming beam. When a flat phase change is programmed across the SLM surface, the net effect is a rotation of the input polarization. After reflection from the SLM surface the beam polarization is rotated in the opposite direction to before by the polarizer and the polarizing beamsplitter converts the polarization modulation from the SLM to amplitude modulation in the beam path detected by the power meter.

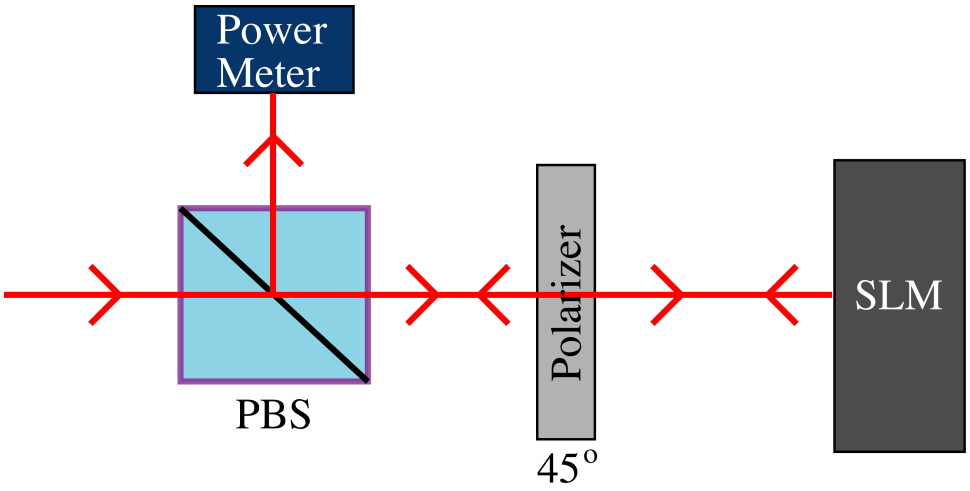

Figure 2.6: SLM Phase Calibration. A Polariser is placed before the SLM at 45°. The SLM is birefringent and will only apply a phase change to one polarization. A range of flat phase changes are applied across the SLM surface in succession, this phase change is converted to amplitude modulation which can be read by the power meter.

The data from the phase calibration experiment is shown in Fig. 2.7 in

black along with a theoretical, cosine, fit shown in red. The peak of this graph represents a phase modulation of π while the two troughs represent a phase change of 0 and 2π respectively. The two troughs were then taken as the limits of the signal sent to the SLM and the points between there used as a look up table.

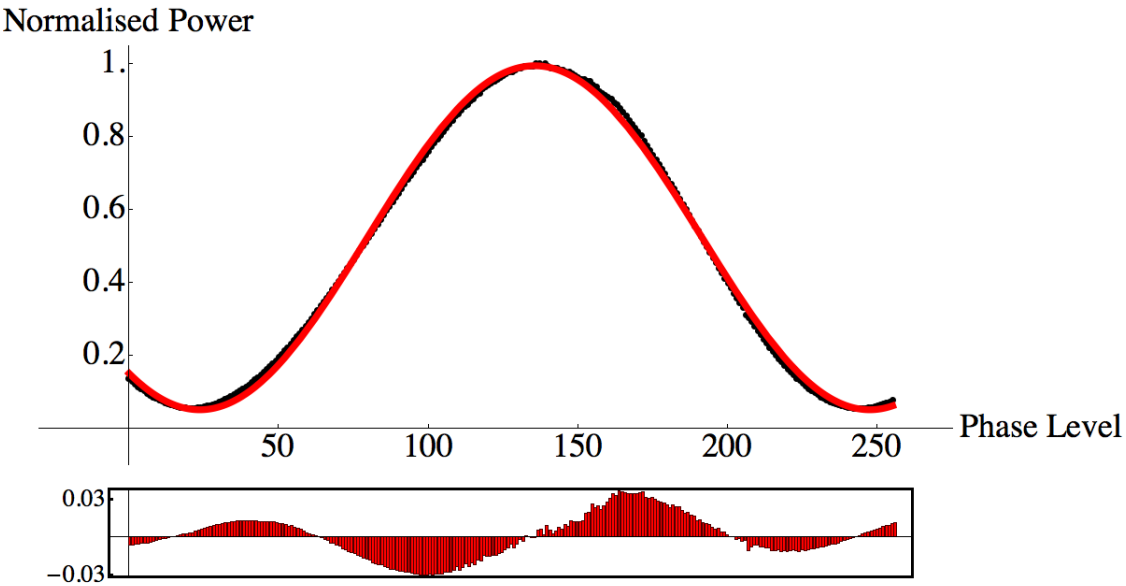

Figure 2.7: Normalised Power as a function of phase level on the SLM is shown in Black. A fit of this data of the form of a Cosine is shown in red and residuals of this fit shown in the inset below the graph.

2.3.2 Intensity Calibration

Reflection from a phase hologram of an LG mode alone tends to excite extra p modes in addition to the beam we are interested in. To counter this effect we must consider the intensity as well as the phase of the beam we wish to create when designing the holograms. While the SLM cannot directly modulate intensity we can add an intensity mask over the phase hologram to select only the modes of propagation we want. This addition of intensity

results in the hologram shown in Fig. 2.4. The conversion from phase grating maximum level between 0 and 255 on the SLM does not vary linearly with intensity in the first order diffraction pattern. The measurement of this effect is shown in Fig. 2.8. The variation is approximately linear in the centre and tails off at the two extrema. This variation is characteristic and unique to each SLM and can be used as a look up table to ensure the response is linear over the entire range.

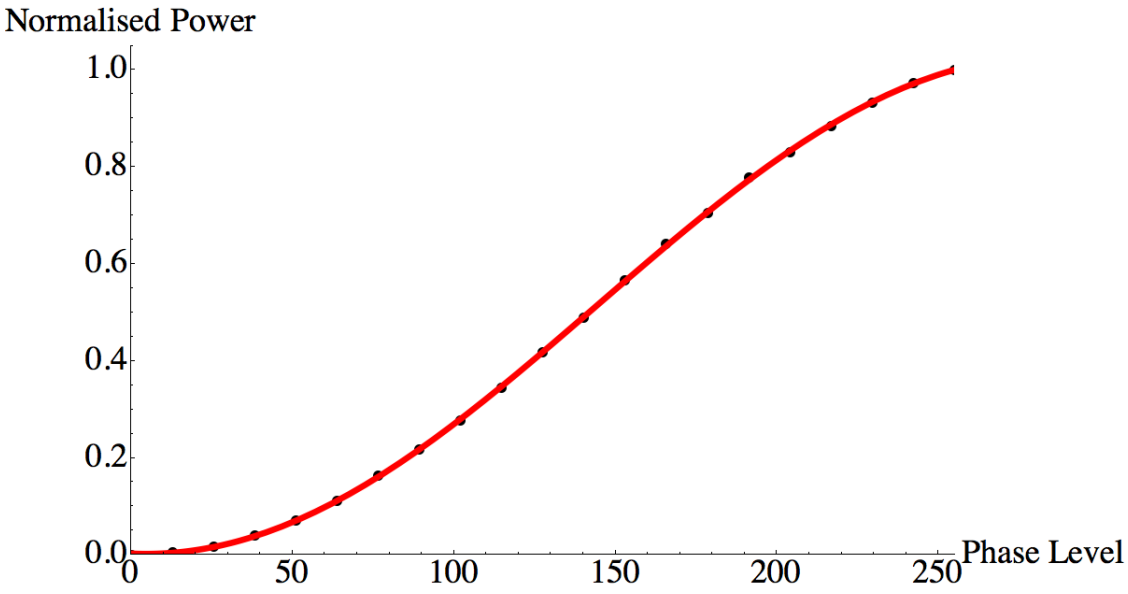

Figure 2.8: Normalised Power in the first diffracted order as a function of phase grating maximum on the SLM is shown in Black. A fit of this data of the form of a Cosine is shown in red.

References

[1] L. Allen, M. W. Beijersbergen, R. J. C. Spreeuw, and J. P. Woerdman. Orbital angular momentum of light and the transformation of laguerre-gaussian laser modes. *Phys. Rev. A*, 45:8185–8189, Jun 1992.

[2] S. Franke-Arnold, J. Leach, M. J. Padgett, V. E. Lembessis, D. Ellinas, A. J. Wright, J. M. Girkin, P. Ohberg, and A. S. Arnold. Optical ferris wheel for ultracold atoms. *Opt. Express*, 15(14):8619–8625, Jul 2007.

[3] M. V. Vasnetsov V. Y. Bazhenov and M. S. Soskin. Laser beams with screw dislocations in their wavefronts. *Optical Angular Momentum*, (52(8):152), 1990.

[4] Jennifer E. Curtis, Brian A. Koss, and David G. Grier. Dynamic holographic optical tweezers. *Optics Communications*, 207(1-6):169 – 175, 2002.

[5] David G. Grier. A revolution in optical manipulation. *Nature*, 424:810–816, 2003.

[6] David McGloin, G. Spalding, H. Melville, W. Sibbett, and K. Dholakia. Applications of spatial light modulators in atom optics. *Opt. Express*, 11(2):158–166, Jan 2003.

[7] L. Brandt, C. Muldoon, T. Thiele, J. Dong, E. Brainis, and A. Kuhn. Spatial light modulators for the manipulation of individual atoms. *Applied Physics B*, 102(3):443–450, 2011.

[8] Graham D Bruce, James Mayoh, Giuseppe Smirne, Lara Torralbo-Campo, and Donatella Cassettari. A smooth, holographically generated ring trap for the investigation of superfluidity in ultracold atoms. *Physica Scripta*, 2011(T143):014008, 2011.

[9] M.W. Beijersbergen, R.P.C. Coerwinkel, M. Kristensen, and J.P. Woerdman. Helical-wavefront laser beams produced with a spiral phaseplate. *Optics Communications*, 112(5-6):321 – 327, 1994.

[10] Alison M. Yao and Miles J. Padgett. Orbital angular momentum: origins, behavior and applications. *Adv. Opt. Photon.*, 3(2):161–204, Jun 2011.

[11] N. R. Heckenberg, R. McDuff, C. P. Smith, and A. G. White. Generation of optical phase singularities by computer-generated holograms. *Opt. Lett.*, 17(3):221–223, Feb 1992.

3 | The Magneto-Optical Trap

3.1 Introduction

In 1987 Raab et al reported the confinement and cooling of an optically dense cloud of neutral sodium. The trap was created through radiation pressure from the combination of 3 retroreflected laser beams propagating in orthogonal axes in combination with a weak magnetic field [1]. The ability to cool and trap neutral atoms had previously been shown theoretically[2] and experimentally in a magnetic trap [3], optical molasses [4] and a combination magnetic and optical trap [5]. The 1987 paper was the first report of the experimental creation of a Magneto Optical Trap (MOT). The MOT has become the powerhouse of many cold atom optics experiments. The MOT has served as the base of a number of major scientific breakthroughs such as the observation of Bose-Einstein Condensates (BEC) in 1995 [6], the development of Cesium atomic fountains now used as the international standard of time [7] and the earliest efforts to construct an atom laser [8].

Magneto Optical Traps cool down an ensemble of Rubidium atoms to temperatures of the order of 100μK [9, 10] at peak densities of the order of 10^{10} atoms cm^{-3} [11]. Such low temperatures in atom ensembles offer long coherence time compared to room temperature and heated atomic vapours due to a reduced collision rate, Doppler width, and a longer interaction time with excitation fields. Cold atom traps are particularly useful as a source of cold dense samples of atomic ensembles. While heated, denser, collections

of atoms are also suitable for interaction with various properties of resonant light such as spin/orbital angular momentum [12], and phase, cold atomic clouds offer much lower collisional loss rates and the possibility for direct manipulation and measurement of the bulk atomic population in various hyperfine states [13, 14].

The operation of a MOT relies on radiation pressure, the force exerted by a light beam resonant with an atomic transition, being absorbed and reemitted. This radiation pressure exerts a change in momentum to the atom of $\hbar k$ each time a photon is absorbed or when the atom spontaneously decays, reemitting a photon in the process. In creating a confined trap of atoms it is preferential to create system where the atoms absorb only the photons which are traveling opposite to their direction. One method for achieving this effect is called Doppler cooling, where a light beam is red-detuned from atomic resonance by an amount, δ. When a atom travels towards a light beam it experiences an effective frequency from the light beam of $\omega_D = \omega_0(1 + v/c)$. For the red detuned beam to be resonant with this atom it must have a detuning, $\delta = -\omega_0 v/c$. Atoms traveling in the opposite direction will see an effective frequency from the beam of $\omega_D = \omega_0(1 - v/c)$. In this case the beam appears to the atom to be much further detuned from resonance causing a bias in the radiation pressure force towards atoms traveling towards the beam. This method of Doppler assisted cooling is called optical molasses [15]. While this method does create cooling it is independent of the spatial position of the atoms and is therefore not sufficient to create a confining potential.

A confining potential can be created by utilizing the Zeeman effect with a spatially varying magnetic field. The level structure of Rubidium is particularly sensitive to magnetic field gradients. They are sensitive enough such that a sufficient separation between the magnetic sublevels can be created to make distinct transitions with relatively weak magnetic field gradients easily generated in the lab. Typically in our lab magnetic field gradients necessary

for MOT operation range between 1 and 15 G/cm.

The scope of this chapter is to give an overview of the mechanisms and techniques necessary for the creation of a MOT mostly focussing on a one dimensional theoretical view. Also in this chapter is the description and results of the various parameters optimized in the creation of our MOT at Glasgow.

3.2 Theory

3.2.1 Doppler Cooling

The simplest atom cooling scheme utilizes the Doppler effect and was first suggested in 1975 by Hänsch and Schawlow [2]. The system of Doppler cooling is easily modeled in 1 dimension, first we consider an atom in free space interacting with two-counterpropagating light beams as in Fig. 3.1. The two beams have the same frequency and are red detuned from atomic resonance, ω_0. For an atom at rest there is no Doppler effect and both beams remain detuned from resonance, reducing the probability of absorption equally in both directions. If we consider an atom moving with a velocity v in the direction of one of the beams then the doppler effect means that the atom "sees" an effective frequency of the beams of $\omega(1+v/c)$ and $\omega(1-v/c)$ for the beam it is traveling towards and away from respectively. The wave the atom is traveling towards is therefore shifted towards resonance, when the beam is red detuned, while the oppositely propagating wave is shifted further away from resonance. The red detuned laser is exactly on resonance when its detuning is $\omega v/c$. The Doppler effect in this case creates an imbalance in the probability of absorption from the two beams with a bias towards the atom absorbing photons from the beam which opposes its direction. With sufficiently intense beams the atoms' velocity can be kept within a few centimetres per second using this method. This cooling scheme with no external magnetic fields

is known as optical molasses and is typically implemented with 6 beams at orthogonal angles in 3 dimensions. Although when combined with magnetic fields configurations with only 4 beams in a tetrahedral shape have been implemented [16], and recently the 4 beam MOT has been implemented with 1 beam and a diffraction grating for the purposes of miniaturization. [17] In Doppler cooling as the speed of the atoms decreases the beams become less resonant with the atom transition frequency thus reducing the probability of absorption. The confining potential of the Magneto Optical Trap addresses this issue by introducing a spatial dependence to the cooling effect.

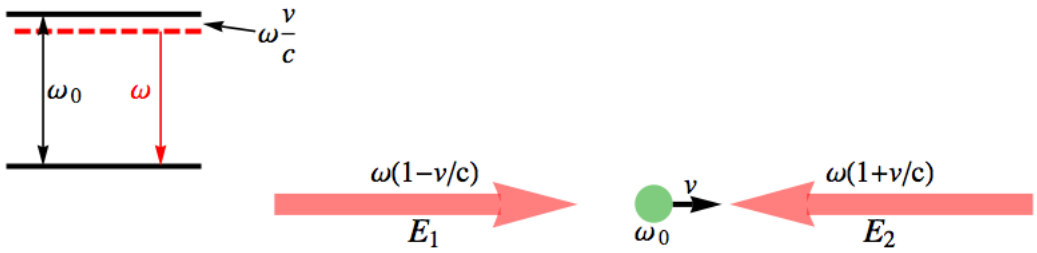

Figure 3.1: Doppler effect for a single atom traveling at velocity v in 1 dimension. The doppler effect causes the red detuned beam which opposes the atoms movement to be shifted closer to resonance than the one traveling in the opposite direction creating an imbalance of forces biased towards slowing the atom down.

3.2.2 Limit of Doppler Cooling

To discover the limits of Doppler cooling we first consider the kinetic energy of the atoms in one dimension. Generally for an atom interacting with two counter-propagating light beams, the radiation forces from the light beams tend to cancel. The effect of fluctuations however leads to a finite temperature. The atom has an equal probability of absorbing a photon from either beam so on each impulse it receives the atom is randomly walked to the right or left. This effect gives the atom a finite velocity and therefore a finite temperature. By the equipartition theorem the kinetic energy is related to

the temperature simply by $\frac{1}{2}m_{\mathrm{Rb}}\bar{v}^2 = \frac{1}{2}k_{\mathrm{B}}T$. Substitutions detailed in [18] give

$$k_{\mathrm{B}}T = \frac{\hbar\Gamma}{2}\frac{1+(2\delta/\Gamma)^2}{-2\delta\Gamma}. \tag{3.1}$$

This function is minimized when $\delta = \omega - \omega_0 = -\Gamma/2$ giving

$$k_{\mathrm{B}}T_D = \frac{\hbar\Gamma}{2}, \tag{3.2}$$

where T_D is the Doppler temperature. This is referred to as the Doppler cooling limit for energy, where the lowest temperature expected in optical molasses is the Doppler temperature, T_D. For Rubidium 87 this temperature is 145μK giving a doppler velocity, $v_D = 2.8\mathrm{cm\ s}^{-1}$. These theoretical descriptions were originally thought to describe the optical molasses technique fully. Experimental observations in the first sodium trap surprisingly found much lower temperatures than this proposed limit. The two-level model of an atom cannot explain this sub-Doppler cooling however more refined descriptions of the cooling process based on the dressed atom picture were developed to explain this effect [19, 10, 20, 21].

3.2.3 Hyperfine Structure

The fine structure in atomic energy levels arises as a result of the coupling between orbital angular momentum **L** of the outer electron and its spin angular momentum **S**. The total electron angular momentum is $\mathbf{J} = \mathbf{L} + \mathbf{S}$ where the quantum number J must lie in the range

$$|\ \mathbf{L} - \mathbf{S}\ | \leq \mathbf{J} \leq \mathbf{L} + \mathbf{S}. \tag{3.3}$$

The fine structure between the D_1 and D_2 lines in Rubidium is relatively large (15nm) and so we can treat the two lines separately.

The hyperfine structure then comes as a result of the coupling of **J** with

the total nuclear angular momentum **I**. The total angular momentum **F** is **F** = **J** + **I** where the magnitude of **F** must lie in the range

$$| \mathbf{J} - \mathbf{I} | \leq \mathbf{F} \leq \mathbf{J} + \mathbf{I}. \tag{3.4}$$

For example in the ground state of Rubidium87, **J** = 1/2 and **I** = 3/2 meaning **F** = 1 or 2 and the splitting between the two states is defined in [22]. In the excited state of ^{87}Rb **J** = **I** = 3/2 so **F** can take any value of 0, 1, 2, or 3.

3.2.4 Saturated Absorption Spectroscopy

Saturated absorption spectroscopy is a technique used in atom optics primarily for precise frequency locking to transitions in the atom. The typical setup for saturated absorption spectroscopy in our experiment is shown in Fig. 3.2 and is based on the setup described in detail in [23]. A 780nm diode laser is mounted together with a collimating lens and an 1800 lines/mm diffraction grating set to 45 degrees to the beam propagation direction. Typically diode current levels are in the range of 100-150mA while being cooled to approximately 14°C in order to preserve diode lifetime. This grating setup forming an extended cavity is known as the Littrow configuration. In the Littrow configuration the first diffracted order from the grating is directed back into the diode creating feedback. The precise angle at which the grating lies, and hence the frequency of light fed back into the grating can be controlled either by standard mirror mount screws or by a voltage driven piezo attached to the horizontal axis. The piezo is used for precise control and locking of the frequency of the laser. The control signal for frequency locking is created using a saturated absorption technique. A small portion of the overall intensity of the beam, typically 1mW with a beam radius of 1.1mm, is taken from the main beam by way of a beamsplitter and a half wave plate. This beam, often referred to as the pump beam, is sent into a room temperature vapour

of Rubidium. Atoms will tend to be in the two hyperfine ground states when not interacting with external fields.

While the name given to this technique is Saturated absorption spectroscopy, in most systems of this type the effect of Hyperfine pumping is much more dominant. Hyperfine pumping is the optical pumping of atoms between the ground state hyperfine levels via the excited states. In hyperfine pumping a pump beam which for example is resonant with the $\mathbf{F} = 1$ to $\mathbf{F'} = 1$ transition will pump atoms to the $\mathbf{F'} = 1$ excited state at which point they can decay to either the $\mathbf{F} = 1$ or $\mathbf{F} = 2$ hyperfine ground states. If the pump beam is sufficiently intense atoms will in general be pumped to the $\mathbf{F} = 2$ hyperfine ground state giving a large population imbalance between $\mathbf{F} = 1$ and $\mathbf{F} = 2$. After the cell the beam is directly reflected, counter-propagating over the path of the pump beam, this beam is known as the probe beam This beam encounters a diminished population of atoms in the $\mathbf{F} = 1$ ground state resulting in diminished absorption of the probe beam from this state. When a piezo is scanned at 30Hz the laser frequency of a doppler broadened section, approximately 500MHz wide, we see distinct peaks in the absorption trace as seen in the inset of Fig. 3.2. These thin peaks in the spectrum, approximately 6MHz wide in Rubidium, are well defined enough to allow locking to frequencies of transitions within the atom extremely accurately. Somewhat counter-intuitively we also observe peaks in the absorption trace exactly midway between two transitions from the ground state to two hyperfine excited states. For more detailed discussion see [24]

The less pronounced effect of saturated absorption is as follows. In the vapour the pump beam burns a hole in the lower state population of the atoms by excitation to the excited state. As we know from the Doppler effect described above the pump beam interacts primarily with atoms that have velocity $v = (\omega - \omega_0)/k$. The hole burnt into the ground state population has a width

$$\Delta\omega_{\text{hole}} = \Gamma\left(1 + \frac{I}{I_S}\right)^{1/2}. \tag{3.5}$$

After passing through the cell a second time the probe beam is reflected off of a beamsplitter onto a photodiode where the absorption trace can be measured. When the frequency of the laser is far detuned from resonance, i.e. $\mid \omega - \omega_0 \mid \gg \Delta\omega_{\text{hole}}$ the pump and probe beams interact with the same velocity class of atoms but oppositely detuned by the doppler effect, $\omega' = \omega \pm kv$. (e.g. if red detuned both beams will preferentially absorb atoms traveling towards them in their frame of reference and therefore traveling in opposite directions in the cell) Close to resonance, $\omega \approx \omega_0$, both beams interact with atoms with zero velocity so the hole burnt in the ground state population by the pump beam reduces the absorption in the probe beam.

Somewhat counter-intuitively we also observe peaks in the absorption trace exactly midway between two transitions from the ground state to two hyperfine excited states. This is due to the fact that when the laser frequency is somewhere between two resonances hole burning will occur for red and blue detuning due to absorption to two upper energy states, one higher and one lower respectively. The effect of such strong hole burning between the two states and the symmetry of the hole burning causes a larger peak to appear exactly midway between the two resonances. These are called cross-over peaks and are typically used for frequency locking due to their magnitude. For more detailed information and derivations see [18].

To frequency lock the laser a modulation signal of approximately 10kHz is added to the, typically 30Hz, scanning signal sent to the piezo. The 10kHz signal is generated by a lock-in amplifier which then multiplies the reference 10kHz signal by the photodiode trace and integrates over several periods. An error signal is generated such that if the laser trace drifts above the desired level the error signal goes negative with a steep gradient and if the laser trace drifts in the opposite direction the error signal goes positive with a steep gradient. This technique provides very stable locking conditions such

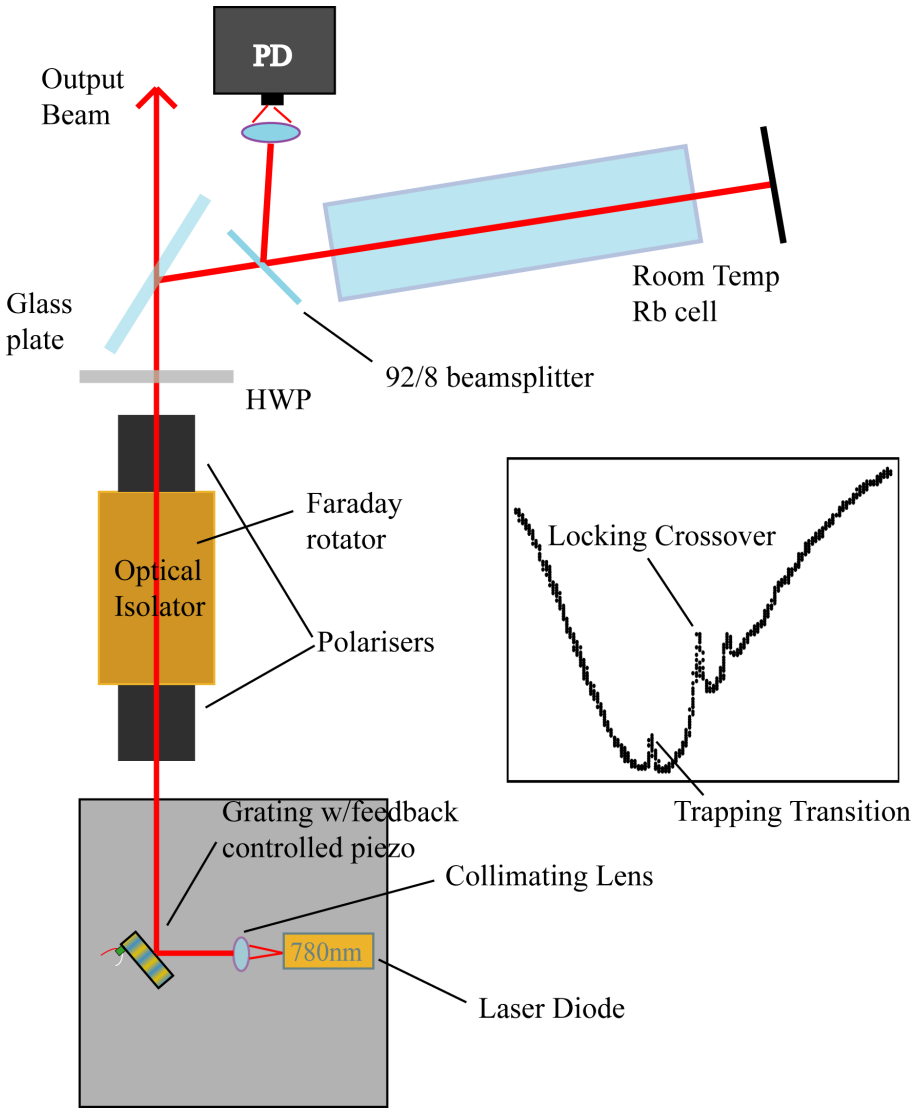

Figure 3.2: Saturated Absorption Spectroscopy Setup: A collimated beam from a laser diode reflects off of a grating in the Littrow configuration with the 1st order being diffracted back into the diode. The grating angle can be modulated with the use of a piezo for precise frequency locking. The beam passes through an optical isolator to prevent feedback before a small portion just above saturation intensity, I_S is sent into a glass cell of room temperature Rb. The beam is then retro-reflected along the same path before being focussed onto a photodiode. The inset shows an example of the resulting absorption trace. Additionally the temperature of the diode is also controlled to be cooled to around 14°C

that the lasers can stay at the desired frequency for many hours.

Additionally in this setup an optical isolator is utilized to prevent unwanted reflections from returning to the laser cavity. Light input into the isolator can be linearly polarised in any direction, typically horizontal in our setup. The strong magnets in the isolator rotate the polarisation 45 degrees as the beam propagates through by utilizing the Faraday effect [25]. The output polariser axis is set to 45 degrees to allow output light in the desired direction. Any light reflected back along the axis of propagation towards the isolator will first enter the output polariser which polarises the light at 45 degrees with respect to the input polariser. Then the light rotates 45 degrees while propagating through the device and when reaching the input polariser has now rotated to 90 degrees with respect to the input polariser, and therefore, the light cannot pass through to the laser.

3.2.5 Acousto Optical Modulators AOMs

In this experiment we typically lock our lasers to crossover resonances in the saturated absorption spectrum as they are the largest peaks and therefore the most stable to lock to. The beams are shifted afterwards to the desired frequency through use of Acousto Optic Modulators (AOMs). An AOM consists of a crystal which is modulated by a piezo electric transducer at frequencies in our case between 70 and 130 MHz depending on the laser in use and the desired transition of the particular beam. Various AOMs were used in our MOT setup and are shown in Appendix A. The vibration in the crystal causes areas of alternating increased and decreased refractive index in the crystal. Input light on this pattern diffracts into orders with increasing and decreasing frequency either side of the 0th order. Orders diffracted in the same direction as the input acoustic wave are diffracted into higher frequency modes while the opposite is true for negative orders. The additional energy necessary for introducing this frequency shift comes from phonon excitations in the material. Scattering into an angle of θ corresponds to the absorption

or destruction of m phonons. The change in frequency of the input light is

$$\Delta f = \frac{mE_{\text{phonon}}}{h}. \tag{3.6}$$

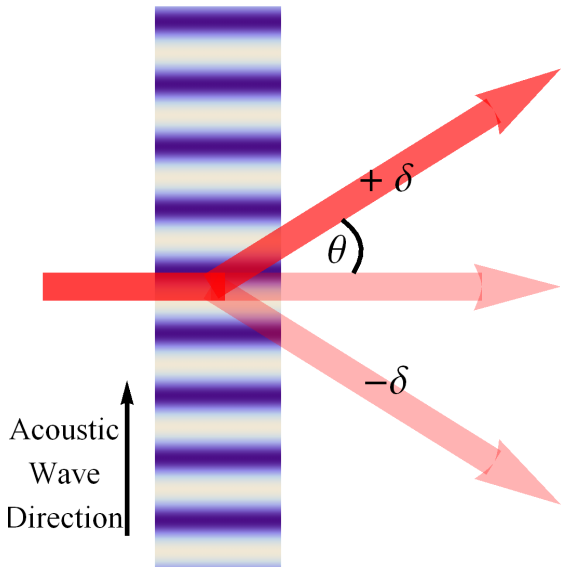

Figure 3.3: Acousto Optical Modulator: A beam input at the correct angle (dependent on the desired order) to the input of an AOM will diffract into multiple diffraction orders. The 0th order remains on the same path at the same frequency as the input beam. The order which is diffracted in the same direction as the acoustic wave is traveling in the crystal will gain energy and hence will output at a higher frequency while the opposite is true on negative diffraction orders. Careful alignment of the AOM can optimize the intensity into the desired diffraction order.

3.2.6 The Scattering Force

It is well known that when an atom absorbs a photon from a resonant light field that the atom's momentum changes by the photon momentum $\hbar k$. Force is defined as the rate of change of momentum. The radiation force that light can exert on an atom is

$$\mathrm{F}_{\mathrm{rad}} = \frac{IA}{c}. \tag{3.7}$$

For atoms the rate of change of momentum, i.e. force, is simply the individual photon momentum times the scattering rate which is [22]

$$R = \frac{\Gamma}{2}\frac{\Omega^2/2}{\delta^2 + \Omega^2/2 + \Gamma^2/4}. \tag{3.8}$$

As is well known, the individual photon momentum is $\hbar k$ and therefore the force due to photon scattering is equal to

$$\mathrm{F}_{\mathrm{scatt}} = \hbar k\frac{\Gamma}{2}\frac{\Omega^2/2}{\delta^2 + \Omega^2/2 + \Gamma^2/4}. \tag{3.9}$$

Ω can be defined in terms of the Intensity as $\Omega = \Gamma\sqrt{\frac{I}{I_S}}$. As $\mathrm{I} \to \infty$ the scattering force tends towards a maximum value of $\hbar k\Gamma/2$ leading to a maximum theoretical acceleration on an atom of mass M of

$$a_{\max} = \frac{\hbar k}{M}\frac{\Gamma}{2}\frac{\Omega^2/2}{\delta^2 + \Omega^2/2 + \Gamma^2/4}. \tag{3.10}$$

For ^{87}Rb this results in a maximum acceleration of $1 \times 10^5 \mathrm{ms}^{-2}$. This shows clearly the possibility for the scattering force to have a significant effect on the velocity of an ensemble of atoms and the MOT takes advantage of this fact.

3.2.7 Zeeman Effect

Each of the hyperfine sublevels contains $2\mathbf{F} + 1$ magnetic sublevels which are degenerate in the absence of a large enough magnetic field gradient. An external field can break this degeneracy, and this behaviour is essential to the workings of the MOT. In the limit of weak fields the magnetic sublevels split linearly, with an energy level splitting given by

$$\Delta E_{m_F} = \mu_B g_F m_F B_z. \tag{3.11}$$

where m_F is the magnetic sublevel, B_z is the magnetic field strength, and g_F is the hyperfine Landé g-factor given approximately by

$$g_F \simeq g_J \frac{\mathbf{F}(\mathbf{F}+1) - \mathbf{S}(\mathbf{S}+1) + \mathbf{J}(\mathbf{J}+1)}{2\mathbf{F}(\mathbf{F}+1)}. \tag{3.12}$$

where $\mathbf{J}$, $\mathbf{S}$, and $\mathbf{L}$ are the Total, Spin, and Orbital electron angular momentum respectively and g_J is the Landé factor defined in [22]. For a detailed discussion and derivation of this equation see [22].

The MOT takes advantage of the absorption of σ^+ and σ^- light. σ^+ and σ^- light is a convenient notation for circularly polarized beams with the atomic quantization axis aligned with the light propagation direction. The MOT achieves this with an external magnetic field. When absorbed, $\sigma^\pm$ light transfers its associated spin angular momentum to the atom which drives the atomic population into a state with higher or lower angular momentum depending on the handedness of the circular polarization of the driving light field. In the case of absorption of many photons by the atom the atomic population tends towards the highest or lowest angular momentum transition possible. In the MOT trapping transition, $|\ \mathbf{F} = 2 \rightarrow \mathbf{F}' = 3\rangle$, a σ^+ light field will drive the atomic population towards the $|\ \mathbf{F} = 2, m_F = 2\rangle \rightarrow |\ \mathbf{F}' = 3, m'_F = 3\rangle$ transition after on average absorption of 5 photons. This transition is known as the the stretched or closed loop transition. The transition is referred to as such, as when the atom is excited to the $|\ \mathbf{F}' = 3, m'_F = 3\rangle$ state,

the only state it can decay to due to selection rules is the $\mid \mathbf{F} = 2, m_F = 2\rangle$ state. Atoms are only lost to the trapping transition from off resonant excitation to other excited states that can decay to the lower ground state or through collisional losses. This steady state situation of the atom-light field interaction aids the efficiency of which the MOT can trap and cool atoms from a room temperature vapour.

The Zeeman effect is utilized in the MOT setup using two coils with opposing currents in the anti-Helmholtz configuration that produce a quadrupole magnetic field. A 2D view of the field shape created by the coils is shown in Fig. 3.4. The field is zero at the centre of the coils and, close to the centre of the field, its magnitude increases linearly from the trap centre creating a linear shift in the magnetic sublevel energy, the example for $m_F = \pm 1$ is shown in the left of Fig. 3.5.

The quadrupole coils in our setup are 5cm in diameter and separated by 10cm, with N = 130 turns and a current, the optimization of which is shown in Fig. 3.18, of 2.4A. These settings produce a field gradient of approximately 10G/cm.

As can be seen in Fig. 3.5 the magnetic sublevels split linearly and in opposing directions either side of the trap centre. An imbalance in the scattering forces in the MOT is created by circularly polarizing the trapping beams. When a circularly polarized beam is absorbed by an atom in a particular m_F state with a well defined quantization axis in the propagation direction, the atom is excited to an upper state sublevel with $m_{F'} = m_F +$ or -1 for σ^+ and σ^- light respectively as dictated by selection rules. The circularly polarized beams are referred to as σ^+ and σ^- light, however strictly this refers to the transitions within the atoms between two m_F states. The beams however are typically referred to as σ^+ and σ^- for conceptual simplicity.

Taking the example of an atom displaced a distance -x from the trap centre as an example, we see in Fig. 3.5 that the positive $m_{F'}$ states have been shifted up in energy and therefore away from resonance with the red

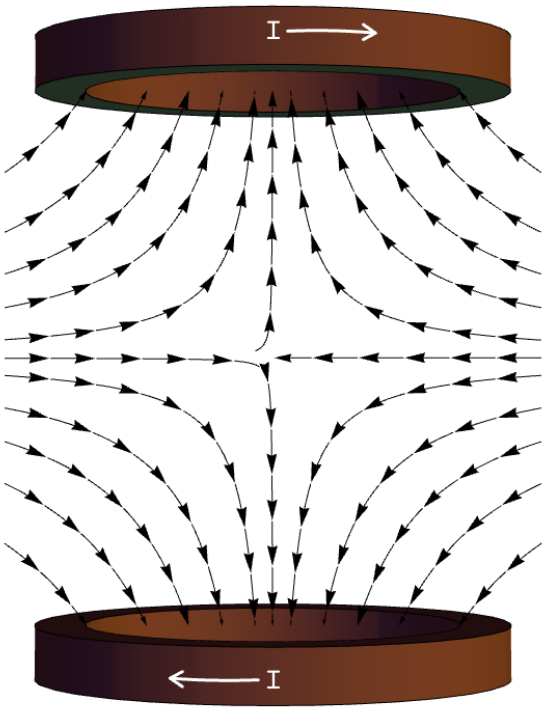

Figure 3.4: Field lines from the MOT coils. A pair of coils with opposing currents, in the anti-Helmholtz configuration, produces a quadrupole magnetic field. The field is zero at the centre of the coils and its magnitude increases linearly from the trap centre producing the desired Zeeman effect in Fig. 3.5

detuned trapping beams. The negative $m_{F'}$ states have been shifted down in energy and therefore closer to resonance with the σ^- trapping light giving much greater probability of absorption from a σ^- beam over a σ^+ beam resulting in the imbalance of force from the two beams shown in the right hand side of Fig. 3.5.

The Zeeman shift at a displacement z_0 from the trap centre is

$$\beta_z = \frac{g\mu_B}{\hbar}\frac{dB}{dz}z_0, \tag{3.13}$$

where g is the Landè g-factor which is

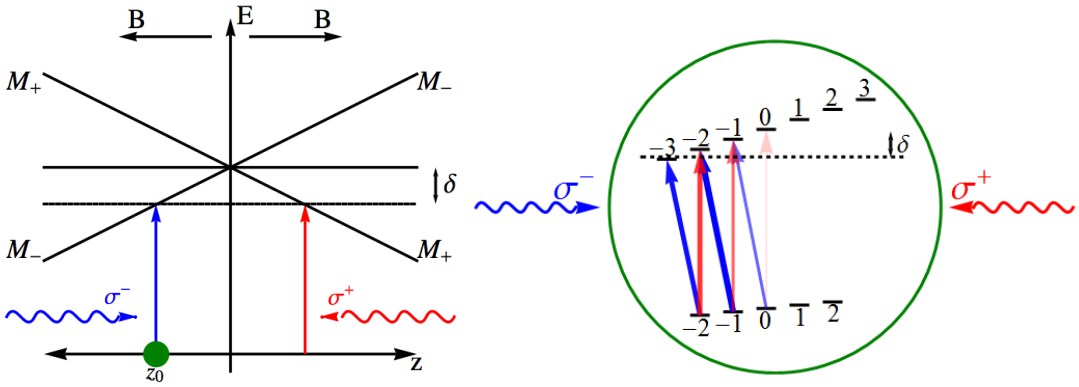

Figure 3.5: a) Zeeman effect in the MOT: The magnetic field gradient in Fig. 3.4 is linear close to the trap centre and in opposing directions either side of it. The levels of the atom are split into m_f states which are split to higher or lower energies depending on their sign. Here we consider and atom at position z_0, left of the zero field point. At this position the negative m_f states have been Zeeman shifted lower in energy while the positive states have been shifted higher in energy. By using laser beams circularly polarised in opposite directions and with a detuning from resonance we can create an imbalance in the force exerted by the beams in favour of the beam that pushes the atoms back towards the trap centre. b) The imbalance in force is created thanks to a combination of the detuning, circular polarization, Zeeman shift and selection rules. The σ^+ and σ^- light can only excite atoms to a +1 or -1 m_f state, compared to their starting state, respectively die to selection rules. Since both the detuning and the Zeeman shift for negative m_f states are negative here σ^- light interacts much stronger with the atom than σ^+ light.

$$g = g_{F'} m_{F'} - g_F m_F, \tag{3.14}$$

where g_F is the hyperfine Landé g-factor. e.g. for the trapping laser stretched state(($\mathbf{F} = 2$, $m_F = \pm 2$) $\rightarrow$ ($\mathbf{F'} = 3$, $m_F = \pm 3$)) g = 1.

The force of the combined σ^+ and σ^- light in one dimension is

$$\mathrm{F_{MOT}} = \mathrm{F_{scatt}}^{\sigma^+}(\omega - kv - (\omega_0 + \beta z_0)) - \mathrm{F_{scatt}}^{\sigma^-}(\omega + kv - (\omega_0 - \beta z_0)), \tag{3.15}$$

where $\omega - kv$ represents the atoms effective resonance frequency due to the doppler shift and $\omega_0 \pm \beta z$ is the resonant frequency for the $m_F = \pm 1$ shifted magnetic sublevels. This force can be approximately expressed as

$$\mathrm{F_{MOT}} = -2\frac{\partial \mathrm{F}}{\partial \omega} kv + 2\frac{\partial \mathrm{F}}{\partial \omega_0}\beta z_0, \tag{3.16}$$

where F is the force a counter-propagating light beam of a given intensity and absorption cross section will exert on an atom traveling towards it. With some simplification we can write this force as

$$\mathrm{F_{MOT}} = -\alpha v - \frac{\alpha\beta}{k} z_0, \tag{3.17}$$

where $\alpha = 2\frac{\partial \mathrm{F}}{\partial \omega}k$. This MOT force takes the form of an harmonic oscillator, with a spring constant $\alpha\beta/k$, and under typical MOT conditions will act as an over damped oscillator for most efficient MOT operation. The combination of magnetic and laser fields in the MOT allow atoms entering the trapping region to be slowed initially by the intersecting laser beams after which the position dependent absorption of σ^+ and σ^- light pushes the atoms towards the trap centre. As the MOT operation is entirely dependent on absorption of only σ^+ and σ^- light we can then approximate that all atoms are pumped into the highest angular momentum state available the majority of the time. This approximately means that only absorption to the largest m_F state contributes to the cooling cycle. The force exerted on the aotms can then be expressed as:

$$\begin{aligned} \mathrm{F\,(v)} =& \hbar k \frac{\Gamma}{2}\left[\frac{I/I_S}{4\left(\delta - kv + \Delta E\right)^2/\Gamma^2 + (1 + 2I/I_S)}\right] \\ & - \hbar k \frac{\Gamma}{2}\left[\frac{I/I_S}{4\left(\delta + kv + \Delta E\right)^2/\Gamma^2 + (1 + 2I/I_S)}\right]. \end{aligned} \tag{3.18}$$

A plot of Force vs velocity for our typical MOT parameters is shown in

Fig. 3.6.

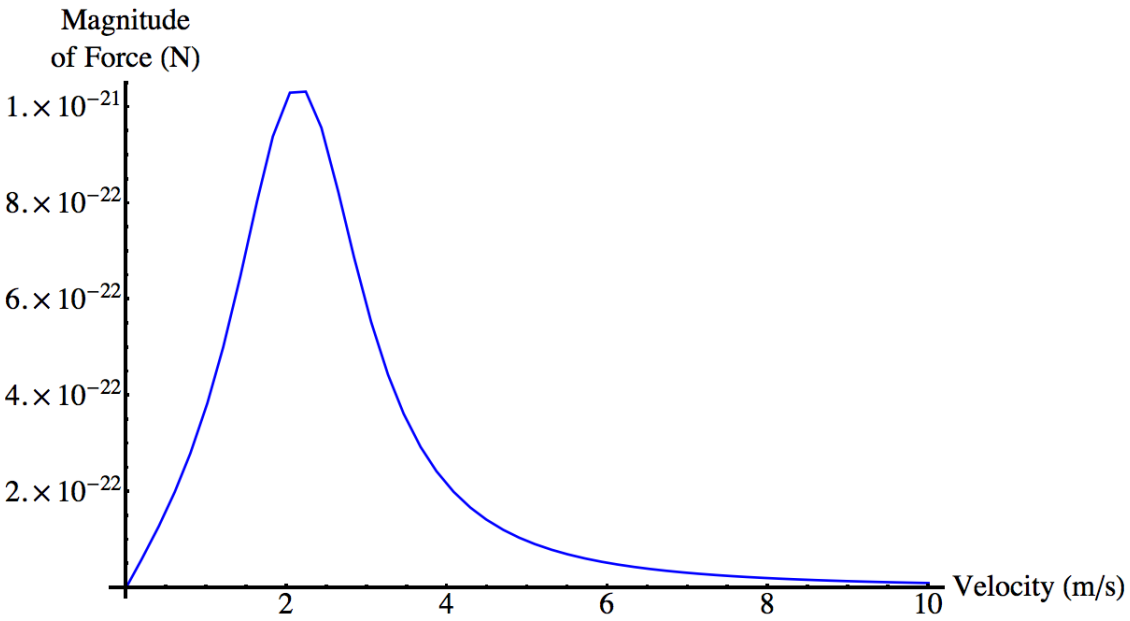

Figure 3.6: Force on an atom vs velocity for typical MOT parameters. For our parameters we observe a peak in force at 2 m/s.

Theoretically for a Trapping beam with a detuning of -17.2MHz and a magnetic field gradient of 10G/cm we obtain a capture velocity of $\approx 4.2\text{ms}^{-1}$. This capture velocity means only a fraction of the atoms from a room temperature vapour (where the average velocity is of the order 290m/s) can be trapped. It was experimentally shown in [26] that this fraction is substantial enough to ensure good loading rates into the MOT. This combination of effects allows the Magneto Optical Trap to easily trap atoms from a background low density vapour at room temperature down to temperatures of as low as 100μK (for ^{87}Rb).

The MOT scheme was predicted to be able to cool atoms down to the doppler temperature in 1989. [10] The doppler temperature can be shown to be as in equation 3.1. The minimum doppler temperature is obtained under the limit of $I_T/I_S < 1$ of $\frac{\hbar\Gamma}{2k_B}$ at a beam detuning of $\delta = -\Gamma/2$. The doppler

temperature for Rubidium is therefore 145μK.

The first MOT and optical molasses experiments revealed that the temperature achievable in these setups was almost an order of magnitude less than that predicted by the doppler temperature. The dressed-atom picture developed in 1989 by Dalibard and Cohen-Tannoudji as well as other descriptions resolve the discrepancy between theory and experiment. [19, 10, 20, 21].

3.2.8 MOT beams - Trapping and Repump

The standard MOT has two laser frequencies in addition to the quadrupole magnetic field called the Trapping and Repump beams. These transitions, for a MOT of ^{87}Rb, are shown in Fig.3.7. First the circularly polarized strong trapping laser, which is red detuned from the $5^2S_{1/2}(\mathbf{F}=2) \rightarrow 5^2P_{3/2}(\mathbf{F'}=3)$ transition is implemented in a 6 beam configuration. The beam in this configuration provides the trapping and cooling forces via absorption and re-scattering of photons at either side of the trap centre in 3 dimensions. While this is a closed transition as described above there is still the small probability for off resonant excitation to the $\mathbf{F'}=2$ hyperfine state at which point the atoms can spontaneously decay to the $\mathbf{F}=1$ lower ground state. In this state atoms are transparent to the trapping light and would be lost to the cooling cycle without additional Repumping.

Typical parameters in our MOT beams are a Trap laser of Intensity 5.2mWcm^{-2} in each beam with a $1/e^2$beam radius of approximately 1cm and a detuning of 17MHz, optimization of which is shown in Fig. 3.17. The Repump beam has an intensity of 2mWcm^{-2} with a beam radius of 0.6cm and zero detuning. For these typical MOT parameters in Rubidium approximately 1 in every 200 photons scattered by the Trapping laser will excite the $\mathbf{F}=2$ to $\mathbf{F'}=2$ transition. Assuming 50/50 split in the spontaneous scattering, 1 in every 400 scattering events will cause the system to lose an atom from the trapping cycle. To combat this effect a second circularly polarized laser, dubbed the Repump laser, is added. This beam in our standard

setup is resonant with the $5^2S_{1/2}(\mathbf{F}=1) \rightarrow 5^2P_{3/2}(\mathbf{F}'=2)$ transition. After absorption by this beam and spontaneous decay from the excited state atoms can return to the trapping cycle. The Repump laser in our setup is used in two directions in the xz plane, that perpendicular to gravity. A two direction setup is used as it is and optically simpler setup to overlap with the Trapping laser in this configuration. The optical setup for the MOT used in the area of the vacuum cell is shown in Fig. 3.8.

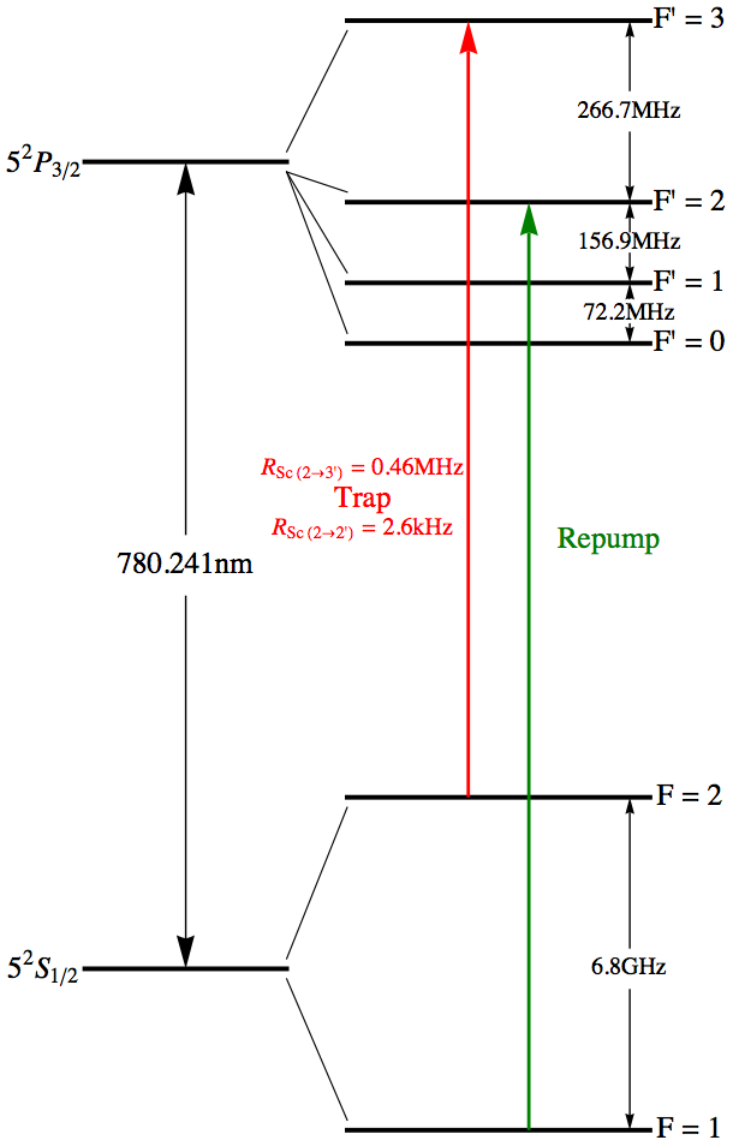

Figure 3.7: In the SPOT experiment we use the same trapping laser as in the regular MOT, (**F** = 2 to **F'** = 3) however we must now consider two possible Repump options. (**F** =1 to **F'** = 1 or 2) We must now consider a different Repump because of the complications arising from the addition of a third laser, called the Depump laser. The purpose of the Depump laser is to pump atoms from the **F** = 2 ground state to the **F'** = 2 excited state where they have a much greater probability of falling to the 'Dark' state. (**F** = 1)

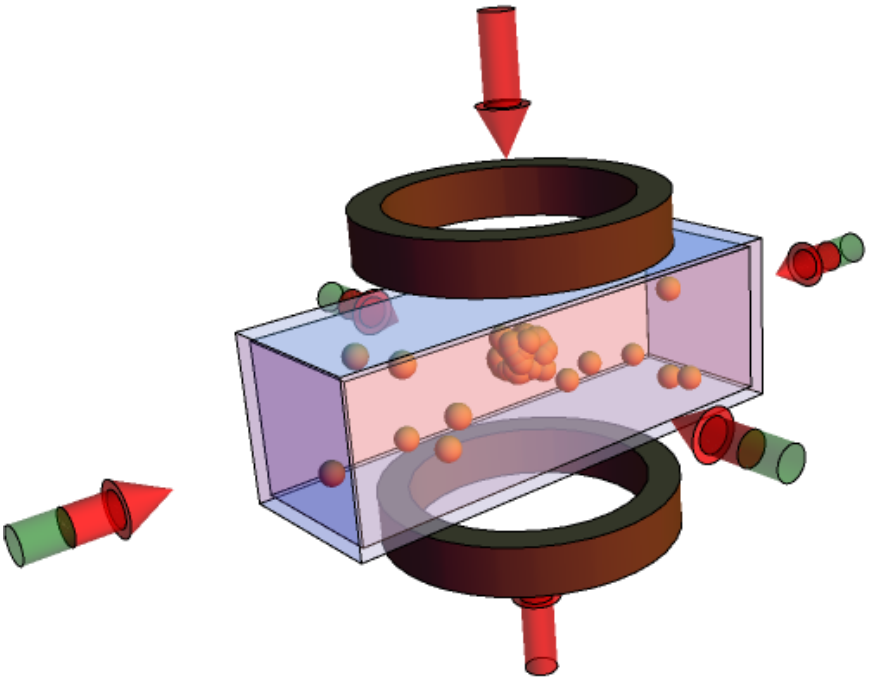

Figure 3.8: Six beam MOT. The Trapping beams shown in Red shine into and are retro-reflected into the trapping region at the zero of the quadrupole field created by the anti-helmholtz coils. The Repump beams overlap perfectly with the trap in the 4 beams in the horizontal plane of the MOT (relative to the coil orientation).

3.3 Fluorescence and Absorption measurements

Information about important MOT parameters such as loading rate, MOT size, atom number, density, temperature and fractional population of lower ground states can be found by two main methods. Fluorescence imaging is the simplest of these measurements that can be performed on the MOT. The fluorescence from the trapped atoms is collected by a lens 2 times the focal length of the lens from the MOT and focused onto either a photodiode or a CCD camera. Assuming a linear response in the detector, the number of

atoms is linearly proportional to the signal on the detector by the equation

$$\text{Signal}_{\text{PD}} = \alpha N \eta \frac{hc}{\lambda} \left(\frac{A}{2}\right)^2 \frac{\Gamma}{2} \frac{I_{tot}/I_S}{1 + I_{tot}/I_S + (2\Delta/\Gamma)^2}, \tag{3.19}$$

where α is the proportionality constant of the detectors response to light, η is the quantum efficiency of the detector, and A is the size of the numerical aperture of the lens.

Additionally the loading time of the MOT can be estimated by measuring the point of saturation in the MOT signal on the photodiode as the MOT is loaded. Depending on background pressure typical loading times in the MOT are of the order 0.5s to 10s.

Temperature measurements of the standard MOT are usually performed using Fluorescence imaging. To measure the temperature the atoms are collected in the MOT until the signal saturates. Some time after this the atoms are released by switching off the Trapping light. The trapping light is then pulsed on at varying delay times and if using a CCD camera the size of the cloud can be measured as a function of expansion time. The temperature of the MOT will then be of the form

$$T = \frac{m_{\text{Rb}} \sigma_t^2}{k_{\text{B}} t^2}, \tag{3.20}$$

where σ_t is the size of the cloud as a function of time, defined as the standard deviation of a gaussian fit of the cloud. The MOT temperature can also be measured using absorption imaging in a more involved process that will be discussed in chapter 3.

MOT density can also be estimated using fluorescence measurements by first measuring the atom number as described above and measuring the MOT size using a CCD camera at zero delay time. The MOT peak density will then be

$$\mathrm{n}_0 = \frac{N}{(2\pi)^{\frac{3}{2}}\,\sigma_x\sigma_y\sigma_z}, \tag{3.21}$$

where $\sigma_{x,y,z}$ are the sizes of the MOT in the x, y and z directions. In our case we assume $\sigma_z = \sigma_x$ as we only observe the MOT in two dimensions and these two dimensions are in the plane with the same magnetic field shape. Typical MOT density in our setup once optimized was of the order of 4×10^{10}atoms cm^{-3}. This value is of the order of the maximum possible density in a standard MOT.

Absorption imaging is a more involved but more versatile measurement technique. In absorption imaging a weak probe light field tuned on resonance to the Trapping transition passes, collimated, through the atomis cloud. Shortly after all light fields and the quadrupole field have been switched off the probe field is switched on along with a quantization magnetic field in the direction of propagation of the probe beam. When passing through the cloud the atoms will absorb an amount of the probe light proportional to the density of the atomic cloud in that area. The atoms will absorb and reemit an amount of light proportional to the density of atoms in the beam path forming a "shadow" in the beam as depicted in Fig. 3.9.

The CCD camera is triggered 3 times during one measurement, once with the probe beam and atoms, I_{OUT}, once with the probe beam but without atoms, I_{IN}, and finally a image is taken without the probe or atoms for background correction, I_B. The optical density, OD, of the could is then given by

$$\mathrm{OD} = ln\left(\frac{I_{\mathrm{IN}} - I_{\mathrm{B}}}{I_{\mathrm{OUT}} - I_{\mathrm{B}}}\right). \tag{3.22}$$

The two dimensional atomic density distribution is then

$$\mathrm{n}_{\mathrm{2D}} = \mathrm{OD}\frac{1}{\sigma_L}, \tag{3.23}$$

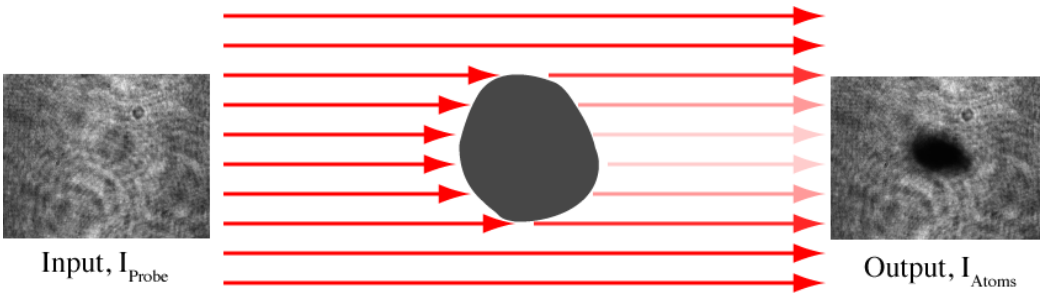

Figure 3.9: Absorption imaging of a MOT. A weak input Probe beam, magnified to be approximately flat to the atoms, is tuned to resonance with the trapping transition has an intensity well below saturation (1.67mWcm^{-2}). The probe beam is absorbed by the atomic cloud and a shadow is formed in the beam which is proportional to the 2 dimensional column density of atoms. Through this image we can calculate the number of atoms in the MOT and the size of the MOT cloud.

where σ_L is the optical cross section for light absorption which is equal to

$$\sigma_L = \frac{\sigma_{\text{Rb}}}{1 + I/I_S + (2\Delta/\Gamma)^2}, \tag{3.24}$$

where σ_{Rb} is a cross section for absorption constant in Rubidium which is $2.9 \times 10^{-13} m^{-2}$ [22]. The number of atoms in the trap is found by integrating over the entire 2D density distribution and accounting for the magnification of the imaging optics, M, and the pixel pitch, A, i.e.

$$\begin{aligned} \text{N} &= \text{M} \times \text{A} \times \sum_{x,y} \text{n}_{\text{2D}} \\ &= \text{M} \times \text{A} \times \text{OD} \frac{1 + I/I_S + 4\Delta^2/\Gamma^2}{\sigma_{\text{Rb}}}. \end{aligned} \tag{3.25}$$

In practice the density of the MOT is measured by calculating this atom number and dividing it by the volume of the trap characterized by the standard deviation, $\sigma_{x,y,z}$, of Gaussian fits in x and y ($\sigma_x = \sigma_z$) across the centre of mass of the 2D optical density distribution. The peak density of the MOT

is then equal to

$$n_{pk} = \frac{N}{2\pi^{\frac{3}{2}}\sigma_x\sigma_y\sigma_z}. \tag{3.26}$$

Typical densities in our MOT setup with approximately 3×10^8 atoms are approximately 4×10^{10} atoms cm^{-3}. This value is at the limit of densities possible in a MOT.

Just like the effect in the trapping beams, efficient absorption imaging requires the use of a closed transition to ensure absorption of multiple photons before an atom is lost to a state transparent to the Probe light. To create the closed loop transition a magnetic field in the direction of propagation of the probe beam is turned on 800μs before the Probe beam is switched on. This Quantization field gradient is of the order of 1G/cm, which is enough to sufficiently separate the various sublevels but not so strong as to significantly change the resonance frequency of the closed loop transition from the non-perturbed resonance frequency. The process of optimization of this field is detailed in the next section.

3.3.1 Compensation Field

A second set of helmholtz coils are added to combat the Earth magnetic field and other stray fields. Typically these field gradients are of the order $<$ 1G/cm. [27] For convenience in our experimental setup these coils were of a rectangular shape as shown in Fig. 3.10, and similar to the design of those found in [28]. These coils are used to cancel out the earth/stray fields and also to create the linear Quantisation field used during absorption imaging.

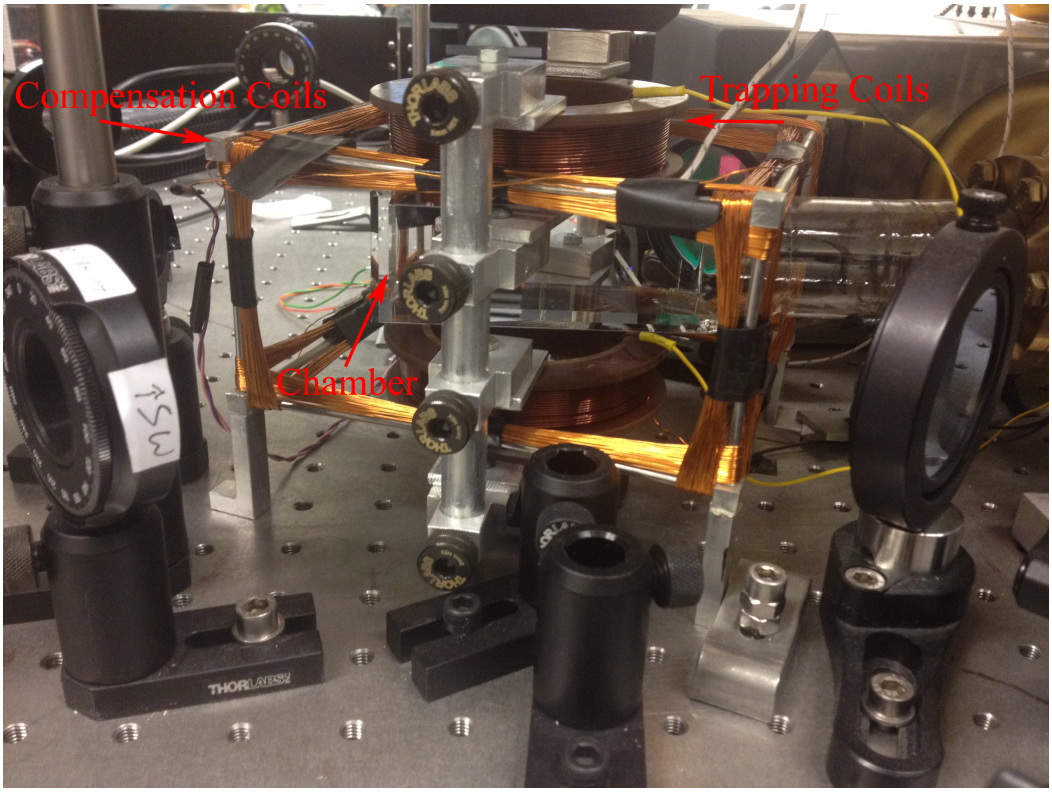

Figure 3.10: Photo of MOT Setup focussing on implementation of magnetic field coils.

To allow for the rise time of the Quantisation coils they are switched on 800μs before the probe field. A typical absorption imaging timing sequence is shown in Fig. 3.11.

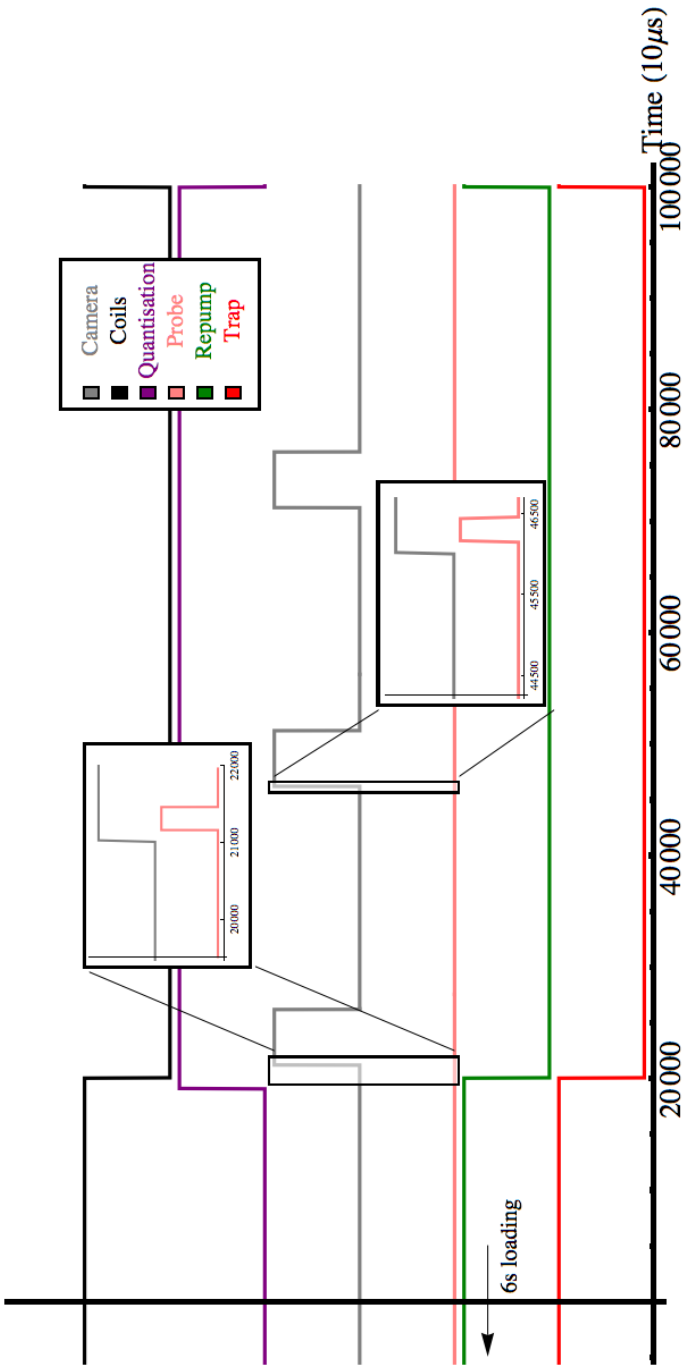

Figure 3.11: Timings of a typical absorption measurement performed on the MOT.

3.4 Experiment

3.4.1 Frequency Choice of Trap and Repump

Our absorption imaging beams are switched via AOMs in the same way as the trapping and repump beams. The AOMs are driven by a series of control electronics outlined in Fig. 3.12 and a TTL pulse emitted from a Data Aquisition (DAQ) card connected to the computer controlling the experiment. The specific frequency shift is controlled by either the voltage level on an analogue output form the DAQ card or by varying voltage driving electronics.

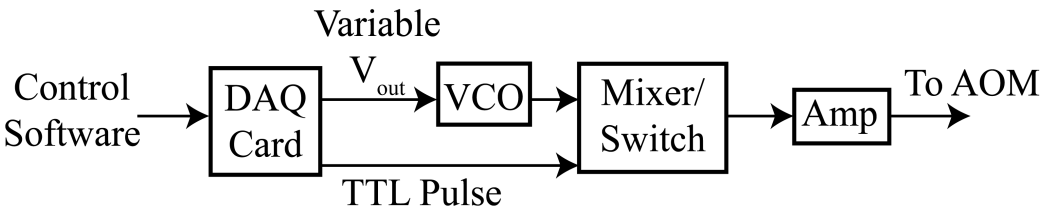

Figure 3.12: AOM electronic control setup.

Three fields are present during any absorption measurement, the Probe light field, the Compensation, and Quantization fields. Efficient absorption imaging requires the optimization of all 3 of these fields. In order to optimize these the compensation field was tuned approximately by viewing the MOT expansion with 2 CCD cameras viewing from orthogonal directions. If the compensation field is set correctly when the coils are switched off for an absorption measurement the MOT should expand uniformly in all directions. The compensation fields were set close to optimum by releasing and re-trapping the atoms in the MOT while the current to each direction, x, y, and z, of the coils was adjusted. When the MOT appeared to expand roughly uniformly the Quantization field was roughly set by adding a small current in the x, and y axes of the Compensation coils such that the MOT

visibly moved in the direction of the desired Quantization field gradient. i.e. in the direction of the Probe light propagation. The detuning of the Probe field was initially set to the resonance frequency for the unaltered **F** = 2 to **F'** = 3 transition.

After this absorption images were taken at a number of different Probe detunings for the conditions of no Compensation field, no Quantization field, and no magnetic fields during the absorption measurement. The results of this test are shown in Fig. 3.13, fits are lorentzian. In this figure we see that the Compensation field shifts the resonance by 1.35MHz and the Quantization field shifts the resonance by 3.26 MHz. We also see that with no additional fields the resonance is shifted by -2.10MHz. This shift is due to the doppler shift due to the lateral movement of the atoms when released by the trapping coils.

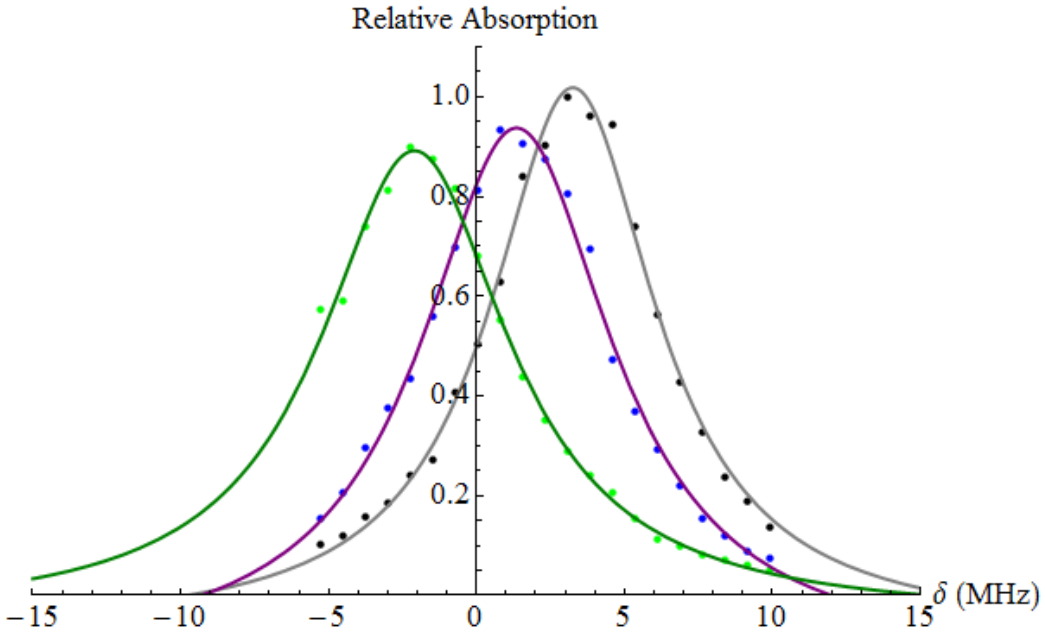

Figure 3.13: Relative absorption vs detuning for the conditions of no compensation field (black/grey), no quantization field (blue/purple), and no magnetic fields (green/dark green).

A shift of 3.26MHz due to the Quantization field was acceptable as the only requirement we have of this field is to create a large enough shift in the magnetic sublevels to facilitate the closed transition used for efficient absorption imaging as described above. The Compensation field should be of the order 1G/cm to compensate for the known Earth field. On a σ^- transition the shift of maximum absorption from resonance is -0.9MHz, i.e. the magnetic sublevel shift of the upper m_F states. The coils were optimized by changing the detuning of the probe beam during successive absorption measurements. The results of this test are shown in Fig. 3.15. The original compensation current settings are shown in blue, while the data from the adjusted current is shown in black, fits are Lorentzian.

The optimum compensation field was found by changing the current in the x and y axes of the MOT and monitoring the relative absorption of a probe beam. The relative absorption vs coil current is shown in Fig. 3.14.

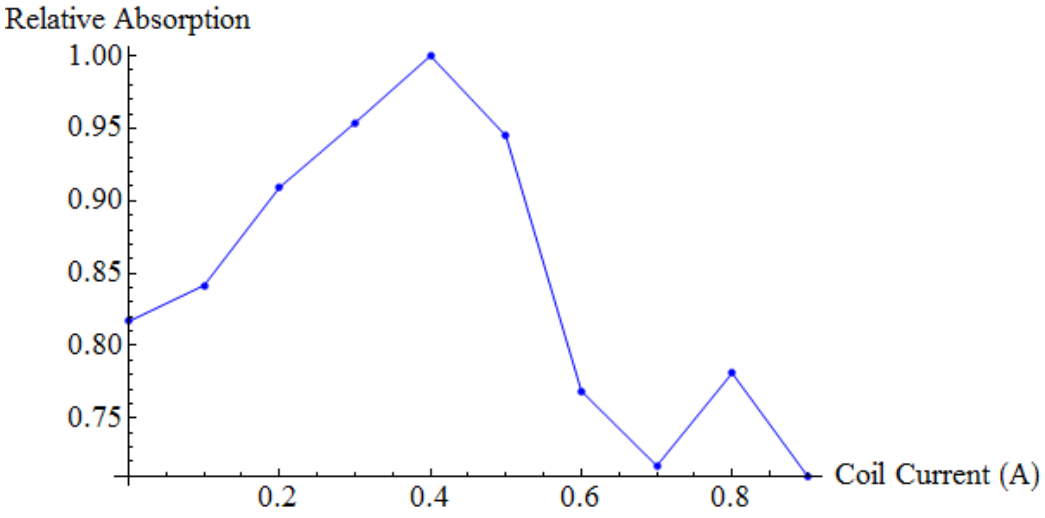

Figure 3.14: Relative absorption vs compensation current.

We observe a peak in absorption signal at 0.4A in the coils, the coils were then set to this value and small adjustments made until the MOT remained central when released by the trapping fields resulting in final currents of 0.38

and 0.44A in the long and short axes respectively. During this time the Quantization field was also adjusted slightly to keep the trap central relative to the position defined by the new Compensation field. The effect of this new compensation field on Probe resonance is shown in Fig. 3.15 with no quantization on and with Quantization on. We observe that with only the compensation field the peak is approximately -0.5MHz detuned from resonance. With the Quantization field added this resonance peak shifts to 2.0MHz detuned, indicating a total shift from the Quantization field of 2.5MHz. This represents a reduction of 0.76MHz in shift due to the Quantization field from the beginning of the optimization process, but this was still an acceptable level.

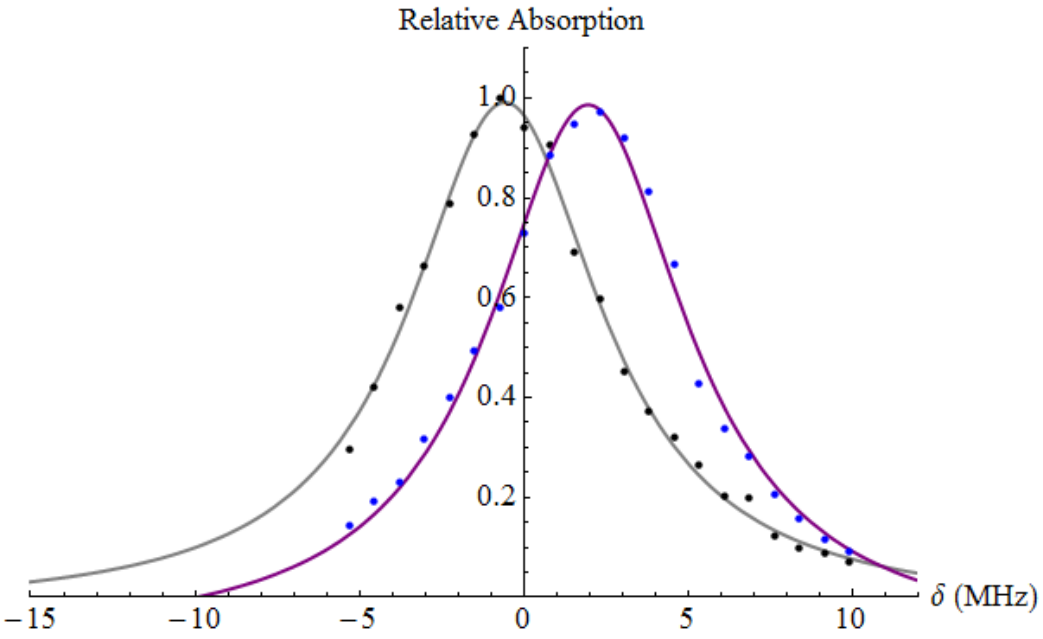

Figure 3.15: Relative absorption taken with the new compensation field in place for the conditions of no quantization field (black/grey) and with the quantization field (blue/purple).

The energy shift of the hyperfine state at a position z_0 from the MOT centre is

$$\Delta E = \mu_B g_F m_F B_{z_0}. \tag{3.27}$$

Our MOT coils produce a field of 10G/cm so this amounts to a shift of 7.0MHz per cm from the trap centre and m_F state for the ground states and 9.3MHz for the Trapping and Repump excited states for the parameters of our MOT.

The trap frequency was chosen experimentally by and observing at which frequency the MOT had the most atoms. The number of atoms was determined through on resonance absorption imaging as fluorescence imaging does not necessarily give a linear change in detector signal with trap beam detuning. The frequency of the trapping laser was altered using a double pass AOM as shown in Fig. 3.16 In the double pass setup an input beam is deflected and increased in frequency on one pass of an AOM then reflected and increased in frequency again such that it follows its input path, now counter-propagating. This allows us to change the frequency of the trap laser over a large range of frequencies without any adjustment to the trap alignment.

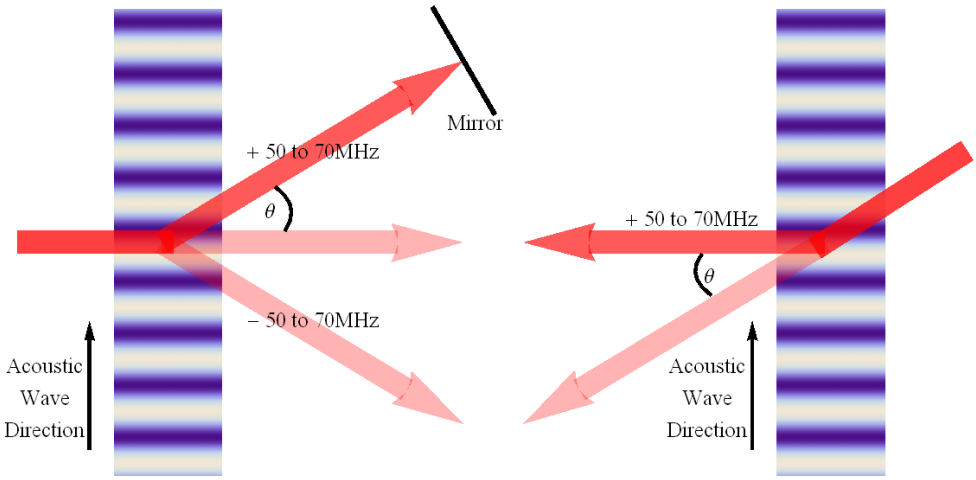

Figure 3.16: Illustration of how a double pass AOM works. a) On the first pass through the AOM works as normal creating different diffracted orders with frequencies of n, where n is the diffracted order, times the AOM frequency. In our case the AOM is operated in the 55 to 75MHz region giving 110 to 150MHz total shift possible (our trap laser is locked to a cross-over 133.2MHz away from the desired transition so this allows the optimum workable range of frequencies for testing). One of these orders is chosen for reflection back towards the AOM. b) The reflected order passes back into the AOM again and the order is again shifted upwards in frequency. This now doublly increased in frequency order follows the same path as the initial input beam. The two can then be separated by a polarising beamsplitter.

The trap frequency and coil currents were optimized by taking absorption images at successive trap beam detunings and trapping coil currents. The results of these tests are shown in Figs. 3.17 and 3.18 respectively, Fits are lorentzian. The trap beam Intensity in these tests was 9.6mW/cm^2. These results show a relatively flat peak at a detuning of 18.66MHz, while in coil current a flat peak at approximately 2.4A is observed. For normal MOT experiments the trap frequency and coil current were set at these values.

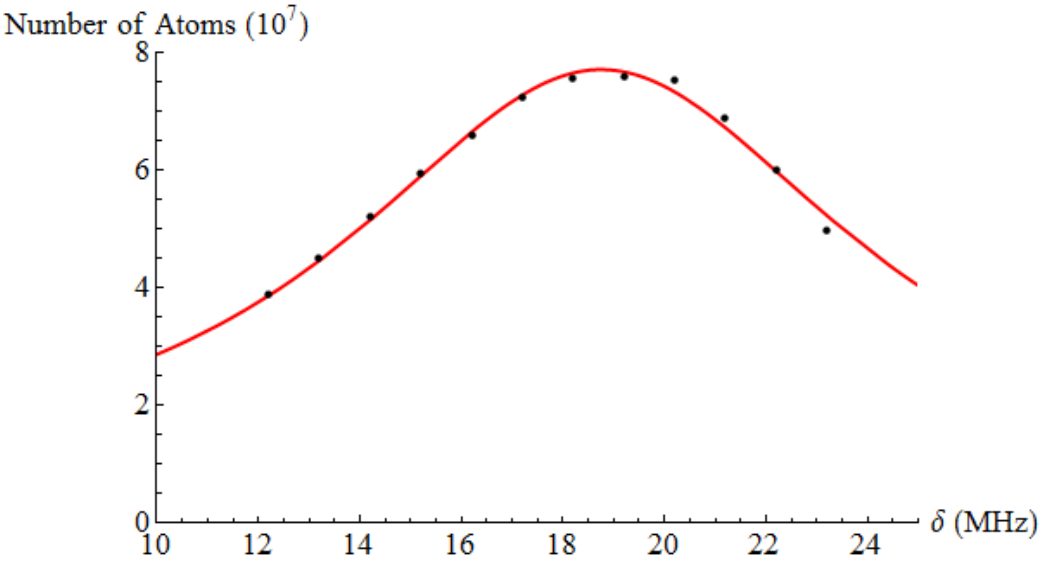

Figure 3.17: Number of atoms measured by absorption imaging vs trap detuning shows a peak at approximately 18.7MHz.

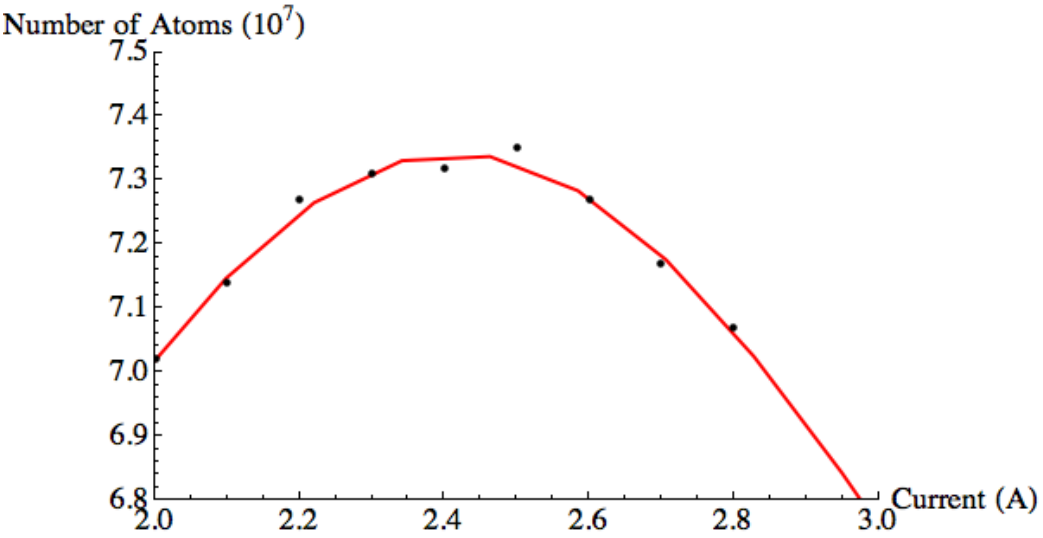

Figure 3.18: Number of atoms measured by absorption imaging vs quadrupole coil current shows a peak at approximately 2.4A.

3.4.2 MOT Temperature Measurements

MOT temperature measurements were taken using a variation on the fluorescence technique described above. Absorption images were taken of the MOT at different delay times after laser beams and main coils had been switched off. Using this method necessitated the need to re-load the MOT after each successive measurement however came with the advantages of better accuracy in the measurement of size of the trap. Absorption imaging is more accurate in this sense as we can adjust the intensity of the probe beam such that the shadow created by the expanding atoms reaches zero. This ensures a maximum resolution image of the expanding cloud. Additionally this method has greater symmetry with the results in the next chapter. Example results of the MOT temperature measurement are shown in Fig. 3.19

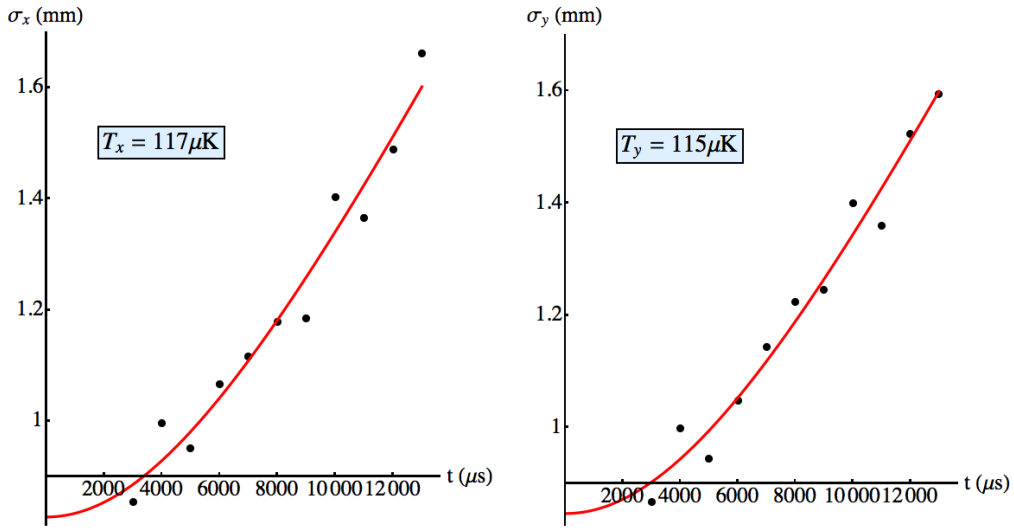

Figure 3.19: Size of trap in x and y directions vs time as atom cloud is allowed to expand in the absence of Trapping and Repump Light, and Trapping coil field. Results were taken using absorption imaging. Fits, in red, are of the form of equation 3.3.

In this figure we see that the size of the atom cloud expands as predicted by equation 3.3. If we fit this equation to the data we obtain temperatures in

the x and y directions of 117μK and 115μK respectively. Taking into account the z direction temperature which we do not observe but assume to behave in the same way as in x due to magnetic field symmetry, we obtain an average temperature for our MOT of 116μK for 2.5×10^8 atoms. This temperature is exactly in line with what we would expect from MOT trapping theory [9, 10].

3.5 Summary

The Magneto-Optical Trap previously designed and built at the University of Glasgow has been successfully optimized with a maximum 3×10^8 atoms at a cloud density and temperature of 4×10^8 atoms cm^{-3} and 116μK respectively. This MOT is a relatively compact system which as will be shown in the next chapter is suitable for use in MOT compression techniques. We have optimized and calibrated fluorescence and absorption imaging methods used to measure the various properties of the MOT above and with slight modification have been used to measure specific hyperfine state population densities. Currently absorption imaging and holographic beam shaping methods are being used to measure the temperature variation across the volume of the MOT in 1 dimension. Early results indicate a spatial variation previously assumed not to be the case.

In the near future this trap and its subsequent variations will be used in atomic interferometry experiments where the phases of the driving fields should effect the relative populations of an atom in a 4-level system [29]. The trap will also evolve to act as the first step in the loading of an optical dipole trap using a high power far red detuned beam.

References

[1] E. L. Raab, M. Prentiss, Alex Cable, Steven Chu, and D. E. Pritchard. Trapping of neutral sodium atoms with radiation pressure. *Phys. Rev. Lett.*, 59:2631–2634, Dec 1987.

[2] T. W. Hansch and A. L. Schawlow. Cooling of gases by laser radiation. *Optics Communications*, 13:68, January 1975.

[3] Alan L. Migdall, John V. Prodan, William D. Phillips, Thomas H. Bergeman, and Harold J. Metcalf. First observation of magnetically trapped neutral atoms. *Phys. Rev. Lett.*, 54:2596–2599, Jun 1985.

[4] Steven Chu, J. E. Bjorkholm, A. Ashkin, and A. Cable. Experimental observation of optically trapped atoms. *Phys. Rev. Lett.*, 57:314–317, Jul 1986.

[5] V. S. Bagnato, G. P. Lafyatis, A. G. Martin, E. L. Raab, R. N. Ahmad-Bitar, and D. E. Pritchard. Continuous stopping and trapping of neutral atoms. *Phys. Rev. Lett.*, 58:2194–2197, May 1987.

[6] M. H. Anderson, J. R. Ensher, M. R. Matthews, C. E. Wieman, and E. A. Cornell. Observation of bose-einstein condensation in a dilute atomic vapor. *Science*, 269(5221):198–201, 1995.

[7] M. A. Lombardi, T. P. Heavner, and S. R. Jefferts. Nist primary frequency standards and the realization of the si second. *The Journal of Measurement Science*, 2:74–89, 2007.

[8] M. Holland, K. Burnett, C. Gardiner, J. I. Cirac, and P. Zoller. Theory of an atom laser. *Phys. Rev. A*, 54:R1757–R1760, Sep 1996.

[9] C.S. Adams and E. Riis. Laser cooling and trapping of neutral atoms. *Progress in Quantum Electronics*, 21(1):1 – 79, 1997.

[10] P. D. Lett, W. D. Phillips, S. L. Rolston, C. E. Tanner, R. N. Watts, and C. I. Westbrook. Optical molasses. *J. Opt. Soc. Am. B*, 6(11):2084–2107, Nov 1989.

[11] G L Gattobigio, T Pohl, G Labeyrie, and R Kaiser. Scaling laws for large magneto-optical traps. *Physica Scripta*, 81(2):025301, 2010.

[12] R. Pugatch, M. Shuker, O. Firstenberg, A. Ron, and N. Davidson. Topological stability of stored optical vortices. *Phys. Rev. Lett.*, 98:203601, May 2007.

[13] C. Liu, Z. Dutton, C. H. Behroozi, and Hau L. V. Observation of coherent optical information storage in an atomic medium using halted light pulses. *Nature*, 409:490–493, January 2001.

[14] G. Labeyrie, C. Miniatura, and R. Kaiser. Large faraday rotation of resonant light in a cold atomic cloud. *Phys. Rev. A*, 64:033402, Aug 2001.

[15] Steven Chu, L. Hollberg, J. E. Bjorkholm, Alex Cable, and A. Ashkin. Three-dimensional viscous confinement and cooling of atoms by resonance radiation pressure. *Phys. Rev. Lett.*, 55:48–51, Jul 1985.

[16] C. Chesman, E. G. Lima, F. A. M. de Oliveira, S. S. Vianna, and J. W. R. Tabosa. Two- and four-beam magneto-optical trapping of neutral atoms. *Opt. Lett.*, 19(16):1237–1239, Aug 1994.

[17] Matthieu Vangeleyn, Paul F. Griffin, Erling Riis, and Aidan S. Arnold. Laser cooling with a single laser beam and a planar diffractor. *Opt. Lett.*, 35(20):3453–3455, Oct 2010.

[18] C. J. Foot. *Atomic Physics*. Oxford Master Series in Physics, 2004.

[19] J. Dalibard and C. Cohen-Tannoudji. Laser cooling below the doppler limit by polarization gradients: simple theoretical models. *J. Opt. Soc. Am. B*, 6(11):2023–2045, Nov 1989.

[20] Mariusz Gajda and Jan Mostowski. Three-dimensional theory of the magneto-optical trap: Doppler cooling in the low-intensity limit. *Phys. Rev. A*, 49:4864–4875, Jun 1994.

[21] Paul D. Lett, Richard N. Watts, Christoph I. Westbrook, William D. Phillips, Phillip L. Gould, and Harold J. Metcalf. Observation of atoms laser cooled below the doppler limit. *Phys. Rev. Lett.*, 61:169–172, Jul 1988.

[22] D. A. Steck. Rubidium 87 numbers. `http://steck.us/alkalidata/rubidium87numbers.pdf`, 2010. Retrieved Jan 2013.

[23] A. S. Arnold, J. S. Wilson, and M. G. Boshier. A simple extended-cavity diode laser. *Review of Scientific Instruments*, 69(3):1236–1239, 1998.

[24] David A. Smith and Ifan G. Hughes. The role of hyperfine pumping in multilevel systems exhibiting saturated absorption. *American Journal of Physics*, 72(5):631–637, 2004.

[25] M. Faraday. *On the Magnetization of Light and the Illumination of Magnetic Lines of Force.* Experimental researches in electricity / by Michael Faraday. The Royal Society, 1846.

[26] C. Monroe, W. Swann, H. Robinson, and C. Wieman. Very cold trapped atoms in a vapor cell. *Phys. Rev. Lett.*, 65:1571–1574, Sep 1990.

[27] K. Lindquist, M. Stephens, and C. Wieman. Experimental and theoretical study of the vapor-cell zeeman optical trap. *Phys. Rev. A*, 46:4082–4090, Oct 1992.

[28] A. S. Arnold. *Preparation and Manipulation of an 87 Rb Bose-Einstein Condensate*. PhD thesis, University of Sussex, 1999.

[29] Giovanna Morigi, Sonja Franke-Arnold, and Gian-Luca Oppo. Phase-dependent interaction in a four-level atomic configuration. *Phys. Rev. A*, 66:053409, Nov 2002.

4 | Dynamic Spontaneous Force Optical Trap

4.1 Introduction

High density and low temperature atoms within optical traps have been sought after since the advent of atom trapping in the last 2 decades. Since the first MOT was demonstrated using Sodium in 1987 [1] researchers have found methods to increase the density of this now ubiquitous tool. For many years these methods were looked at for the necessary second step to transfer atoms from MOT to Bose Einstein Condensates (BECs). High-density ultracold atomic vapours have since emerged as promising candidates for a number of applications including quantum memories, high precision metrology, and quantum simulations/computation [2, 3]. In standard MOTs the achievable densities are limited due to the interaction with the trapping light itself, mainly due to re-radiation forces. This chapter will report on our progress thus far in achieving a high density trap of Rubidium 87 with a temperature comparable to that of a MOT. This trap will take the form of a dark SPontaneous force Optical Trap (dark SPOT).

In the years since the first MOT many methods of density enhanced traps have emerged, including Compressed Magneto Optical Traps (CMOTs) in ^{85}Rb, [4], ^{87}Rb [5] and Cs [6] achieving densities of 5×10^{11} Atoms cm^{-3} for 2×10^7 atoms, 1.6×10^{11} atoms cm^{-3} for 10^9 atoms, and 1×10^{12} Atoms

cm^{-3} for 3×10^8 atoms respectively, at the expense of slight heating of the trapped atoms. The ^{87}Rb CMOT in [5] is performed in a semi dark way similar to our experiment. During the initial phase of compression, where the magnetic field density is ramped up a hole is created in the Repump beam which results in a higher collapsing force being applied to the atoms in the centre of the trap. Both of these traps have the requirement for an order of magnitude increase in magnetic field strength from the regular MOT state and the need for many linewidths detuning from resonance after the initial loading stage. In addition both traps require relatively high numbers of atoms in the initial MOT loading phase of $> 10^9$ atoms.

Another high density trap is the dark SPOT [7], in which a dark circle is imaged in the centre of the repump laser in order to shield the atoms in the centre of the trap from the repumping light. This dark centre in the Repump beam atoms in the centre region of the trap which have fallen to the ground state experience no radiation force from any beam and hence do not re-radiate scattered photons reducing the repulsive force which limits MOT densities. The first dark SPOT [7] was observed in 1992 using Sodium where densities of 10^{12}atoms cm^{-3} were achieved with 10^{10}atoms. The maximum density was observed when the fractional bright state population, ρ, was lower than 1%. Previously the dark SPOT technique has been utilized in both Cs [8], and ^{87}Rb [9] to reduce collisional losses and improve the lifetime of captured atoms from the MOT state. In Cesium a 5 times reduction in collisional losses was observed, while an order of magnitude increase in lifetime was achieved in ^{87}Rb. More recently the dark MOT technique, [10] which is essentially a temporal rather than spatial dark SPOT has been taken advantage of which is capable to trapping large numbers of atoms at high densities an order of magnitude greater than in the MOT. Most recently it has been shown that densities approaching the Ioffe-Regal regime [11], in which there is a phase transition to strong localisation, can be approached in a crossed dipole trap tuned to the blue of the resonance, in order to trap atoms in the dark core

of the dipole beam allowing compression by tuning the size of the hole. [12]

High density dark SPOTs of Rubidium have proven to be more elusive than in some other atomic species due to a weaker coupling between the excited states and the hyperfine ground state. There is a lower level of scattering from excited states pumped by off-resonant absorption of the Trapping light due to the relatively large detuning between the excited hyperfine states. This means that only 1 in every thousand photons pumped by the trapping light are scattered such that the atom falls to the lower ground state. This necessitates the use of a third beam in addition to the normal MOT setup to pump the atoms into the hyperfine ground state. This beam is known as the Depump beam, and was first suggested in the original SPOT paper [7]. The Depump beam used in our experiment is shown in Fig. 4.1 with the other MOT transitions. This is an additional challenge in Rubidium not present in previous high density SPOT experiments such as the original dark SPOT, which used Sodium atoms in their trap, as Sodium atoms have a much more favourable scattering into the ground state, there was no need for an additional Depumping beam in that experiment.

To avoid any non-desired EIT effects between the Repump light and the new Depump beam, the Repump transition has been moved to the $5^2S_{1/2}\mathbf{F} = 1$ to $5^2P_{3/2}\mathbf{F}' = 1$ transition.

In this section we present a technique which avoids some of the usual difficulties present in the other density enhancing experiments discussed above. These difficulties include heating during compression [12], the necessity for more than one cell/trap [13], the need to reduce pump laser intensities and increase detunings/magnetic field density mid way through the experiment [5, 6], and the need for high numbers of atoms in the initial MOT stage with low number retention. Here we report up to 75% retention of atoms from MOT to dark SPOT. We are aided in our development of the dark SPOT by use of a Spatial Light Modulator (SLM) to shape both of our Repump and Depump light with any desired phase or intensity distribution. SLMs have

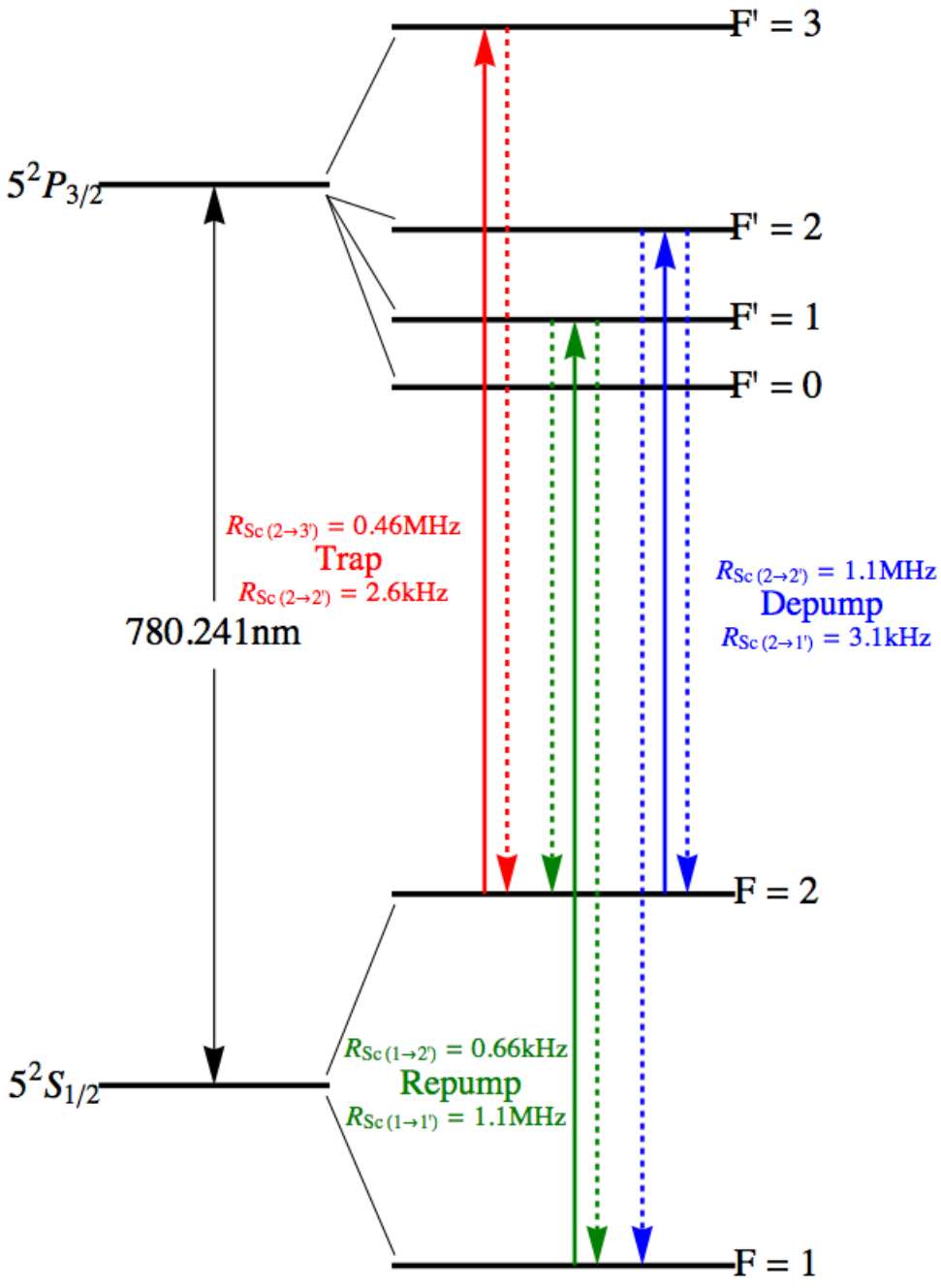

Figure 4.1: Ground and excited state hyperfine levels in ^{87}Rb and the transitions used/possible for Trapping, Repumping, and Depumping.

proven useful tools in atom optics experiments in a range of implementations including atom transport [14], atom guiding [15] , dipole trapping [16], optical lattices [17], and evaporative cooling [18].

The versatility of the SLM offers us a great advantage over previous experiments in this area, where dark circles were imaged into the beam, as we can dynamically shift between Repump geometries when transferring from MOT to dark SPOT loading phases. Here we use the SLM to our advantage by not only finding the perfect size of hole for optimum SPOT density but we also shape our Depump laser to the inverse of the Repump intensity field to create two distinct regions in the trap. One region where atoms are pumped to the F = 1 state and one where the atoms that escape from the Depump region can be re-trapped by the Trap and Repump fields. To our knowledge this is the first dark SPOT of ^{87}Rb made with a focus on large peak densities more than an order of magnitude greater than the standard MOT limit which is our trap is approximately 4×10^{10} atoms cm^{-3}.

This section will cover the development of the various holographic modes considered for and used in the SPOT experiment, ranging from Laguerre-Gaussian modes, newly developed Super Laguerre-Gaussian modes and simple circular intensity masked modes. The various mode types are investigated for their advantageous properties for the dark SPOT and their likelihood to be easily created by an SLM with limited resolution.

Next the various MOT parameters such as magnetic field density and trap detuning were reoptimized for SPOT operation. The SPOT peak density was then optimized for SPOT parameters such as Depump loading time and hole size in the Repump beam. Finally we record the peak density achieved in the SPOT along with the corresponding temperature at this peak density.

4.1.1 Theory of Density Limiting Regimes in the MOT

In the first SPOT experiment, using Sodium, high densities were achievable without the need for any beams other than the standard MOT beams as the excited state detuning in Sodium is small enough to allow enough off-resonant absorption from the Trapping beam to excited states which can scatter into the hyperfine ground state. The steady state scattering rate as a function of detuning is

$$R_{sc} = \left(\frac{\Gamma}{2}\right) \frac{(I/I_S)}{1 + 4\left(\Delta/\Gamma\right)^2 + (I/I_S)}, \tag{4.1}$$

where all symbols have their usual meanings. For $10^{-2}\mathrm{Wcm}^{-2}$ of trapping light 17MHz red detuned from the Trapping transition and hence 249MHz blue detuned from the $\mathbf{F} = 2$ to $\mathbf{F'} = 2$ transition we get a natural scattering rate of approximately 16kHz. For comparison the scattering rate of the 17MHz detuned trapping state is 2.89MHz. As a result, without any repump light, atoms are lost into the $\mathbf{F} = 1$ ground state only for every 400 or so trapping cycles. Previous dark SPOTs in other alkali atoms have taken advantage of the closer detuning of their hyperfine excited states causing much more favourable scattering into the hyperfine ground state. In order to speed up the transfer of atoms into the sheltered ground state we employ the Depump laser resonant withe the $\mathbf{F} = 2$ to $\mathbf{F'} = 2$ transition. Varying the intensity and detuning allows us the set the depump rate, and additionally we have control over its spatial shape, independently from the trapping transition.

Detailed in [7] and [19] a simple model suggests 3 density limiting factors in a MOT where the atomic species has 2 hyperfine ground states we will dub "dark" and "bright" for $\mathbf{F} = 1$ and $\mathbf{F} = 2$ respectively. Note that these are not quantum mechanical dark and bright superposition states, but the "dark" state is simply a hyperfine state that is not resonant with the driving laser. The 1st limit arises from the force exerted by the trapping beam which is

$$\mathrm{F_T} = -kpr\hat{\mathbf{r}}, \tag{4.2}$$

where k is the spring constant of the standard MOT and p is the probability that the atom is in the bright hyperfine state, i.e. a normal MOT would have $p \approx 1$. Scattering of the trapping light by atoms in the MOT leads to the repulsive force

$$\mathrm{F_R} = -k\,(\mathrm{n}/\mathrm{n_0})\,p^2 r\hat{\mathbf{r}}, \tag{4.3}$$

where n is the density and $\mathrm{n_0}$ is the density limit for the unaltered MOT. (in our case 4×10^{10} atoms cm^{-3}). For the case of a stable MOT we require that $\mathrm{F_T} > \mathrm{F_R}$ which leads to the first limit for density of

$$\mathrm{n} < \mathrm{n_0}/p. \tag{4.4}$$

The second limit relates to the fact that for a high number MOT the column density of atoms is limited by the fact that the atom cloud must be transparent for the trapping light i.e.

$$\mathrm{n}dp < b_0, \tag{4.5}$$

where $\mathrm{b_0}$ is the 2 dimensional density limit and d is the $1/e^2$ radius of the unaltered MOT. Using the fact that $\mathrm{n} = \mathrm{N}/d^3$ we arrive at the second limit

$$\mathrm{n} < (b_0/p)^{3/2}\,\mathrm{N}^{-1/2}. \tag{4.6}$$

Finally for large fractions of atoms in the ground state the volume of a low density gas at fixed temperature varies as $p^{-3/2}$ resulting in a 3rd limit

$$\mathrm{n} < \mathrm{N}p^{3/2}/d_0^3, \tag{4.7}$$

where d_0 is the cloud diameter for a standard MOT for low N.

As the SPOT becomes more and more effective we should approach the

limit defined by the column density of the atoms and their transparency to the trapping light. In Fig. 4.2 I have simulated this limit with varying fractional bright state population, p. Here we see that the density limit increases incredibly quickly for $p < 0.2$, for $p = 0.2$ the theoretical density limit is 4.5×10^{11} atoms cm^{-3} while $p = 0.1$ equates to a limit of 1.27×10^{13} atoms cm^{-3}. If a fractional bright state population of 1% could be reached the density limit increases to 4×10^{13} atoms cm^{-3} which is approaching densities commonly only achieved in optical dipole traps, a well established second step towards BEC. Clearly there are massive gains to be made in reducing the fractional bright state population.

We can see clearly that in the 2 regimes of a stable MOT and high atom numbers reducing the population of atoms in the dark state has great potential for increasing the trap density by orders of magnitude. Specifically the act of shielding the inner most atoms to both the trapping and Repump light we should be able to reduce the repulsive force dramatically. Applying the theory developed in [7] we would expect to see the greatest increase in optical density for $p < 0.1$, i.e. 90% of atoms in the dark state. However as there are many differences between the two experiments such as different atomic species and our SPOT creation technique is dynamic rather than steady state we cannot take this for granted.

We also note the studies done on the loss rates and hence density limiting factors of collisional losses in dark SPOTs studied in both sodium [20] and cesium [8]. The paper on Cesium suggests that at low light intensities collisional losses through hyperfine state switching will dominate in this type of trap while the one using Sodium suggests otherwise. Long SPOT loading time measurements have been undertaken in order to study the effects of losses on our dynamic dark SPOT.

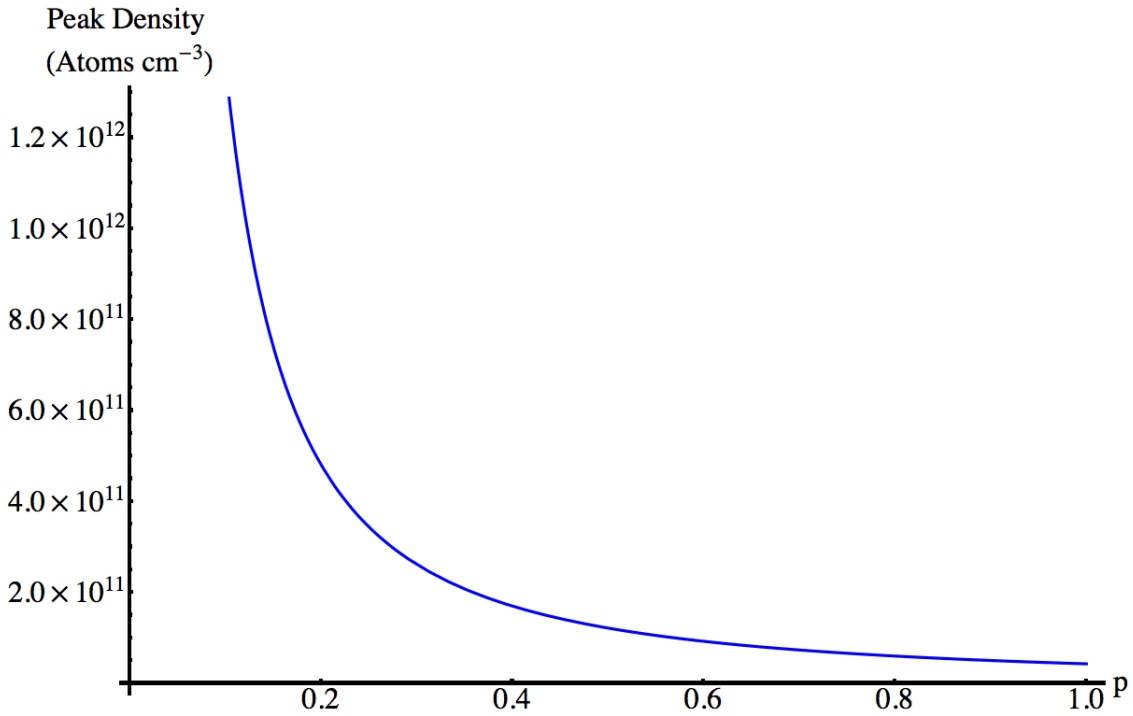

Figure 4.2: Simulation of the theoretical peak density from the limit described by equation 4.6 in the column density limited regime as a function of fractional bright state population p.

4.2 Holograms developed for use in a dark SPOT

In our experiment we have full control over the phase and intensity of our Repumping beam through use of the SLM. This allows us to investigate any and all possible beam profiles for use in the SPOT. Theoretically the ideal Repump beam for the SPOT experiment would consist of a perfectly flat outer halo around the beam, which would assure good overlap with the outer edge of the trapping light, with a perfect zero in the centre of the beam which could be altered in size at will. Experimentally, a finite remaining light intensity is unavoidable, mainly due to diffraction of the Repump beam, but also due to scattering of Repump light when it interacts with atoms

in the outer region of the trap. The latter is out of our control, but we have investigated differently shaped beam profiles and their effect on atom densities.

Laguerre-Gaussian beams, as detailed previously, have some of these desired properties, in particular they propagate without diffraction ensuring the profile of the light field should not alter within the trapping volume.The spiraling phase structure of LG modes ensures a perfect zero on the centre of beam propagation axis, however this perfect zero is limited to exactly at the centre of the beam propagation axis. By altering both the desired beam waist and l value generated on the SLM we can freely alter the peak to peak radius of the mode created in the Repump beam. LG modes with a large value of l will give a thin ring with a large hole in the centre with essentially zero intensity to the atoms, however the thin ring at large radius will reduce the effective recycling efficiency around the SPOT. Lower l modes with larger beam waists will create "fatter" rings but at the expense of smaller effective zero intensity in the centre of the beam. As shown in [21], the maximum intensity of an LG beam can be approximated to be

$$I_{max} = I_l / \left(4\sqrt{\mid l \mid}\right), \tag{4.8}$$

at a radius,

$$r_l \approx= \omega\sqrt{\mid l \mid /2}. \tag{4.9}$$

While different types of LG modes can meet both of the requirements of our ideal SPOT beam, no single LG mode can match both perfectly at the same time. To this end we sought after ways to combine Laguerre-Gaussian modes in such a way that we could create a beam with a flatter zero in the centre and flatter ring of intensity around the beam. One possible solution proposed was to use a superposition of multiple Laguerre-Gaussian modes with different beam waists and different p values dubbed Super-Laguerre

Gaussians which from now on we will refer to as SuperLG's. These modes are somewhat analogous to super-gaussians [22]. The profile of a SuperLG is of the form

$$\Psi(W,p) = \sum_{0}^{i_{max}} \sum_{0}^{p_{max}} \Phi_l^p(\omega_0 + iW), \tag{4.10}$$

where W is a constant typically less than the initial beam waist ω_0. The biggest obstacle to such a beam's use in this experiment is the unstable propagation dynamics caused by unmatched Gouy phases and differing Rayleigh ranges due to the changes in p and beam waist between each individual component of the beam respectively. Fig. 4.3 shows examples of various SuperLG modes after the collimation lens of the typical SLM setup, approximately 2.5m total propagation distance after the SLM face. In the figure, modes with W = $0.25\omega_0$ and i_{max} = 1, 2, 5, and 10 are shown. Larger values of i_{max} could not be tested at the time as the Labview program used to generate our hologram modes had memory management issues at higher values, however the modes captured show a disproportionate increase in size of the hole in the centre of the beam as more and more modes are superimposed into the overall beam. In addition the beam becomes slightly flatter at the peak and the gradient of intensity decrease at the edge of the beam becomes slightly flatter. Importantly however the beam appears to not have any significant distortion due to the additional beam waist modes after the collimating lens in our setup.

As these experimentally tested modes showed some promise we performed a full investigation into using superpositons of multiple ω and p modes to attempt to match a perfectly circular Intensity distribution. i.e. the perfect dark SPOT Repump beam.

Fig. 4.4 shows the progress of a simulation of a SuperLG mode in matching a perfect circular intensity mask for increasing i_{max}, with $p = 0$ and $W = \omega_0/50$. As i_{max} increases we observe a number of changes to the mode

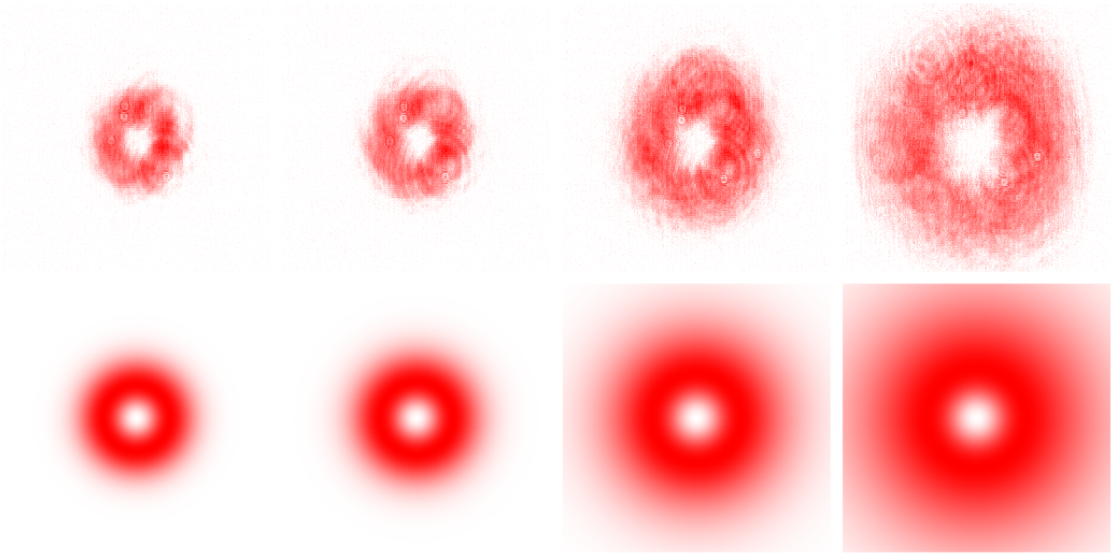

Figure 4.3: **Top Row:** Examples of SuperLG modes with multiple beam waists, W = $\frac{\omega_0}{4}$, and p = 0. From left to right: i_{max} = 1, 2, 5, and 10. **Bottom Row:** Theoretical simulations of the modes.

profile. From $i_{max} = 0$ to $i_{max} = 500$ the peak of the mode shifts in position from the beginning of the mask towards the centre, increasing the overlap with the mask. More importantly however we observe the peak of the beam becoming asymmetric as the intensity gradient on the outside edge of the beam becomes more shallow. In addition the size of the zero in the beam does not change size with increasing i_{max} meaning we maintain the ideal zero in the centre while improving the capture volume overlap at the edge.

Fig. 4.5 shows the progress of a simulation of a SuperLG mode in matching the desired mask for increasing numbers of p modes present in the beam. Initially additional p modes appear to reduce the overlap with the mask however relatively quickly the peak of the SuperLG begins to much more closely match the flatness of the mask by $p_{max} = 25$. Additionally a big improvement on the waist modes is the gradient of the edge of the SuperLG at both sides of the peak much more closely matches the ideal pattern. The cost of

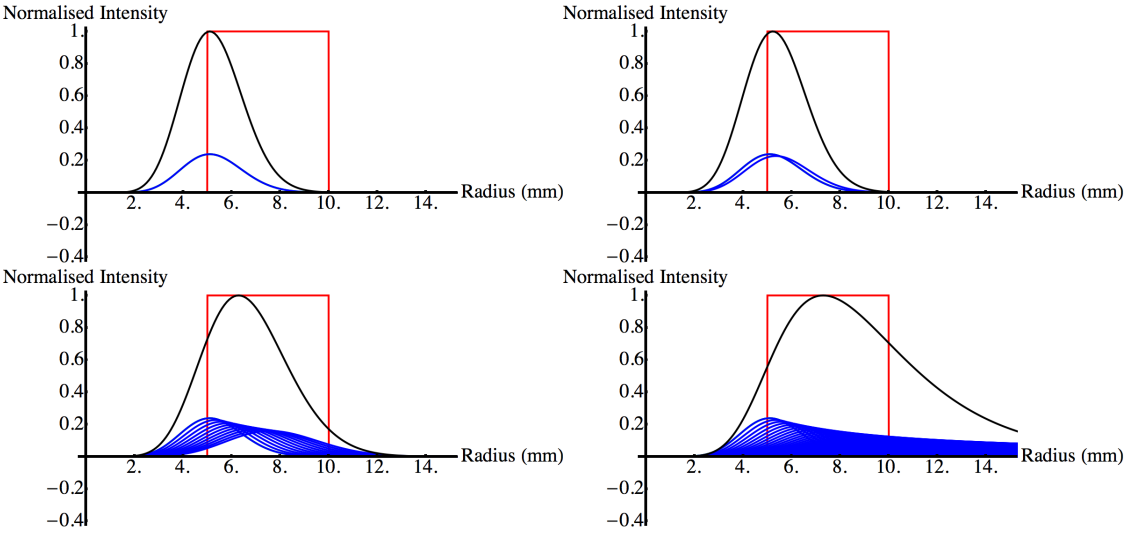

Figure 4.4: SuperLG modes with increasing beam waist components and $W = \omega_0/50$. In all images one half of the SuperLG modes are shown in one dimension. The "LG Top Hat" mask shown in red and the SuperLG beam in black. Individual components of each beam are be shown in blue. These are scaled so that the original modes is 0.2 of the final mode. Top Left: $i_{max} = 0$. Top Right: $i_{max} = 5$. Bottom Left: $i_{max} = 50$. Only 1 in every 10 modes is shown for clarity. Bottom Right: $i_{max} = 500$. Again only 1 in every 10 modes is shown for clarity.

this better shape at the peak however is small oscillatory behaviour towards the centre of the beam which would be detrimental to SPOT loading.

Fig. 4.6 shows the combination of a SuperLG mode with $i_{max} = 50$ and $p_{max} = 25$. $i_{max} = 50$ was chosen to save on computation memory. We do see some improvements in the beam profile, specifically the oscillation towards the edges of the beam is damped significantly.

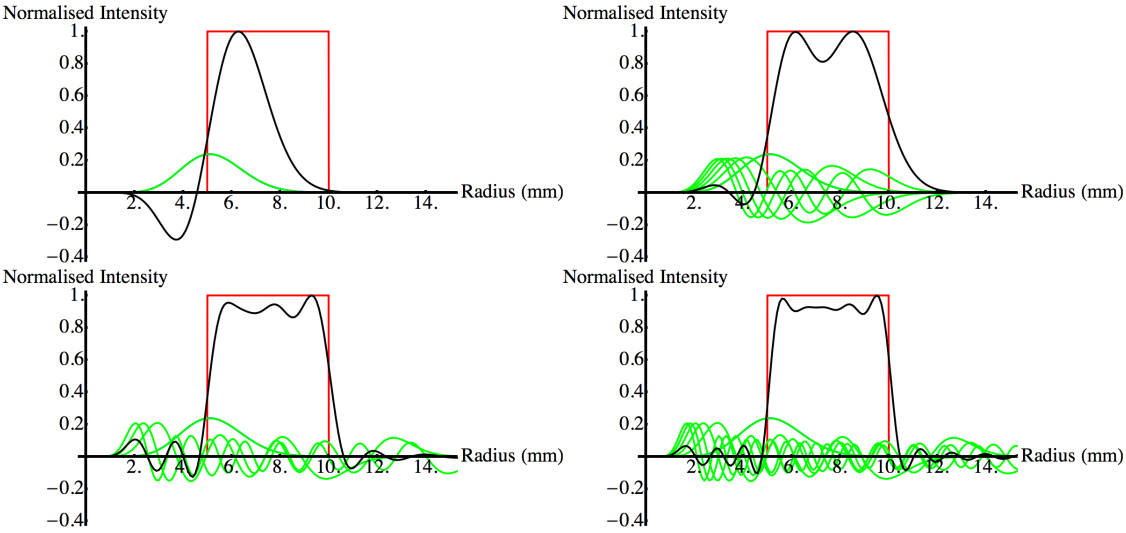

Figure 4.5: SuperLG modes with increasing numbers of p modes at constant ω_0. Again in all images one half of the SuperLG modes are shown in one dimension., and now constituent p modes are shown in green. Top Left: $p_{max} = 1$. Top Right: $p_{max} = 5$. Bottom Left: $p_{max} = 15$ Only 1 in every 5 modes is shown for clarity. Bottom Right: $p_{max} = 25$ Again only 1 in every 5 modes is shown for clarity.

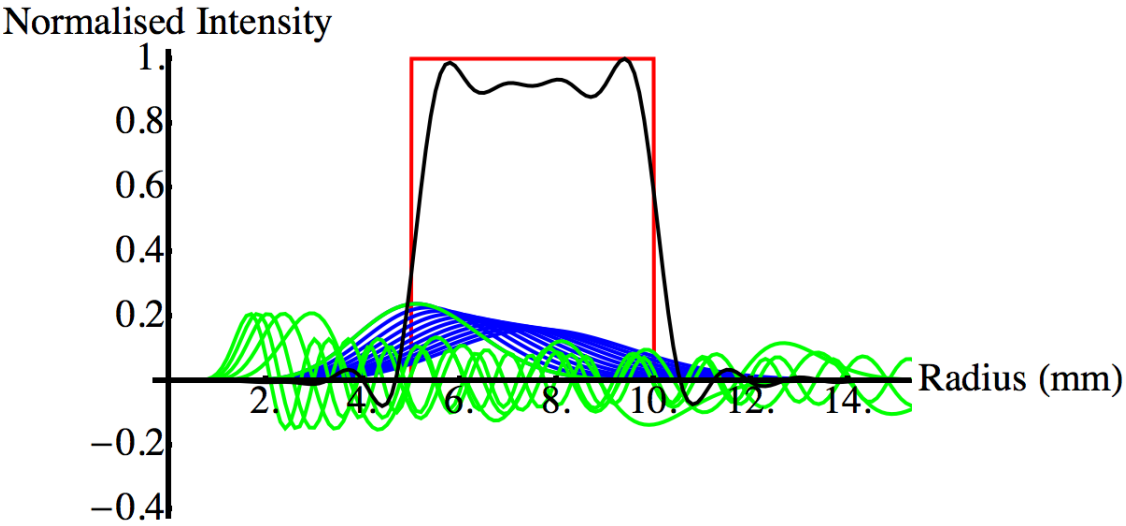

Figure 4.6: SuperLG mode and its constituent parts based on both waist and p mode variations. In this particular mode $i_{max} = 50$ and $p_{max} = 25$ were chosen.

While these combination SuperLG modes show promise in creating an appropriate intensity structure for the SPOT experiment they come with the added disadvantage of requiring large numbers of combined modes. Particularly in the case of multiple p modes this presents a problem when creating these beams using the SLM. Since the SLM has a limited number of pixels, 800×600 in our case, it can only be used to create so many modes at one time. Efficiency of the conversion will also drop as more and mode modes are added to the overall structure.

4.2.1 Circle Intensity Masks

Given the problems with creating SuperLG modes we sought after a solution using a much simpler hologram pattern. By intensity masking the standard ramped diffraction grating, used to create the LG fork hologram, with a circle of intensity 0 in the centre of the beam axis with 1 elsewhere we can approximate an intensity zero in the centre of the diffracted beam. An example of a circle mode hologram and the corresponding intensity pattern generated in the diffracted order are shown in Fig. 4.7. Only an LG mode or similar beam can create an exact intensity zero in the beam however we can achieve a very close approximation to an intensity zero in the circle modes by using a sufficiently large circle radius in the beam and while working close to perfect imaging conditions. This beam shares some of the advantages and disadvantages of high l LG modes, so both LG modes and Circle modes were chosen for use in the SPOT experiment.

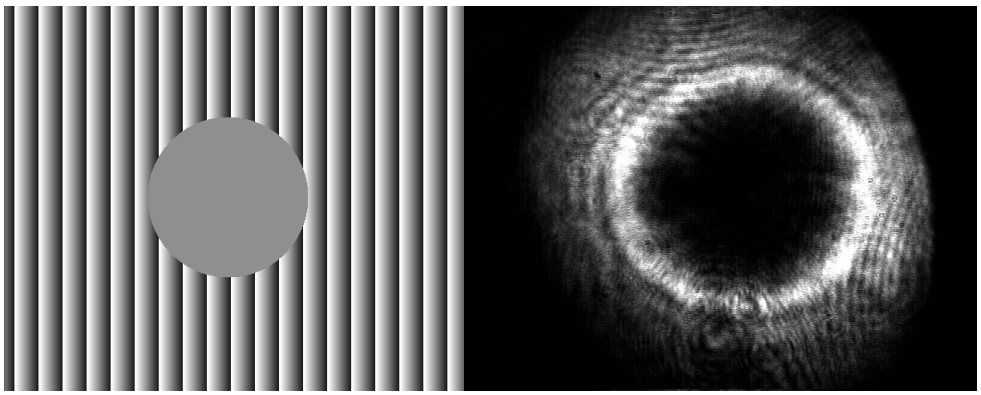

Figure 4.7: Left: Circle hologram consisting on the standard ramped grating previously discussed (with larger spacing for visualisation here) multiplied by an intensity mask with 0 in the centre and 1 outside. Right: corresponding beam shape in the m = 1 diffracted order after filtering and expansion/collimation.

4.3 Prediction of SPOT Shape

As discussed previously the Repump beams in the MOT are limited to the two horizontal arms of our trap. The shaped Repump beams in the SPOT experiment are also confined to these two axes only. In this scenario the effective confining potential for the SPOT becomes the overlap between two LG or Circle modes propagating perpendicularly with respect to one another. A simulation of this trapping potential is shown in Figs. 4.8 and 4.9. The first figure shows the SPOT shape from side on, i.e. through the propagation axis of either Repump beam, on the left. On the right a top down view is shown, i.e. through the centre of the Helmholtz coils. Fig. 4.9 shows this shape in a 3 dimensional view. The potential somewhat surprisingly more closely resembles a rounded off cube than a spherical shape as one might expect.

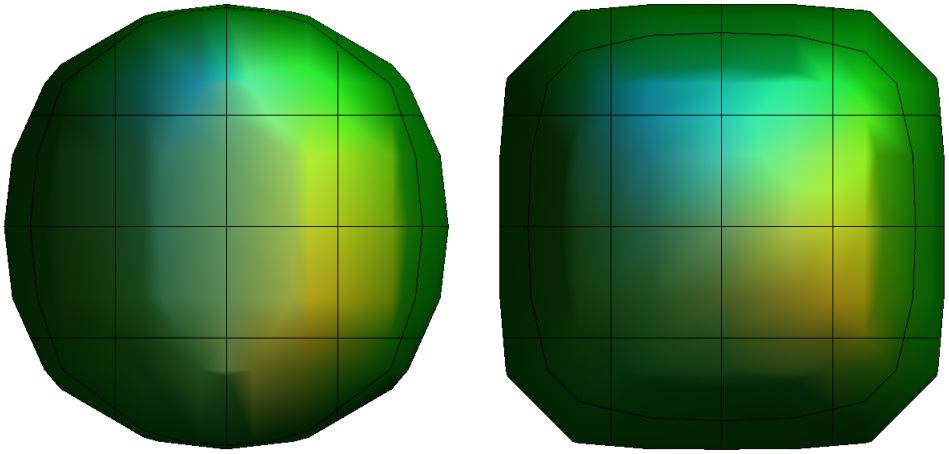

Figure 4.8: Left: SPOT confining potential viewed through the propagation axis of on of the Repump beams in the horizontal plane. Right: SPOT shape viewed from a top down point of view, i.e. through the Helmholtz coils of the MOT.

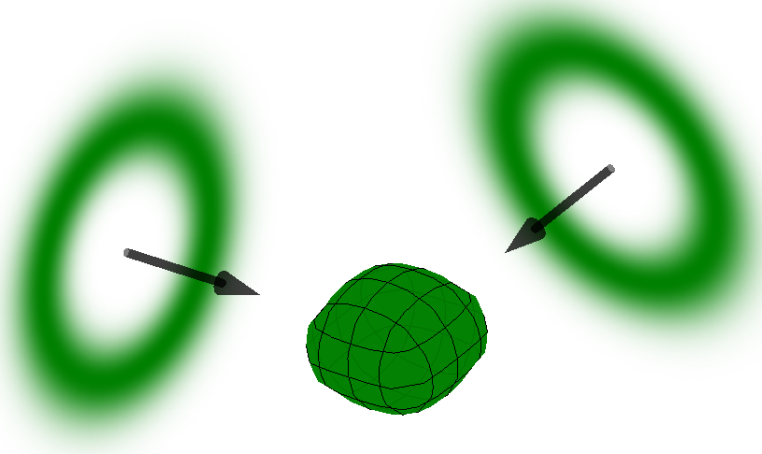

Figure 4.9: Three dimensional view of the theoretical SPOT shape. Two shaped Repumping beams, in case case LG modes with $l = 5$ propagate at exactly right angles to one another. The inverse of their intensity overlap is the shape of the SPOT confining potential shown in the centre.

4.3.1 Experimental Setup

The experimental setup for the SPOT experiment is shown in Fig. 4.10. The key differences of the SPOT experiment from the standard MOT setup are the addition of the depump laser and SLM. The Trapping laser is prepared as before 17MHz detuned from the $5^2S_{1/2}\mathbf{F} = 2$ to $5^2P_{3/2}\mathbf{F}' = 3$ transition. The Repump beam, still on resonance as in the MOT, is spatially filtered to improve mode quality before being shaped by diffraction off of the SLM and filtering of the desired order. Additionally a small portion of the Repump beam is now separated from the main beam and after frequency shifting to the $5^2S_{1/2}\mathbf{F} = 1$ to $5^2P_{3/2}\mathbf{F}' = 2$ transition which is used for two purposes. The beam is used to indirectly pump atoms to the $\mathbf{F} = 2$ ground state via the excited states for accurate number measurements of atoms in the ground state. This beam is also used for direct absorption imaging of the SPOT for size measurements used for SPOT density calculations.

Also added is the Depump laser, which is locked to the $5^2S_{1/2}\mathbf{F} = 2$ to $5^2P_{3/2}\mathbf{F}' = 1, 2$ crossover peak and frequency shifted 133.2MHz to the $5^2S_{1/2}\mathbf{F} = 2$ to $5^2P_{3/2}\mathbf{F}' = 2$ transition (not shown in the experimental diagram for simplicity). The beam is then polarized horizontally and shaped to the inverse of the Repump beam geometry by direct reflection from the SLM. The inverse intensity distribution is created in the direct reflection from the SLM, i.e. the 0th order, which is then combined with the first order of the Repump beam. This is done by reflecting both Repump and Depump off of a non-polarising beamsplitter where the Depump joins the Repump beam path at a small angle. This SLM setup is shown in further detail in Fig. 4.11. The combined Repump/Depump pair combine with the trap in the two horizontal arms of the MOT setup as before after 2× magnification.

The top of Fig. 4.11 shows an exaggerated zoom in of the Repump/Depump SLM setup. The two beams, Repump shown in Green, Depump in Blue are combined with a small angle difference at the surface of the SLM. The 1st diffracted order of the Repump beam is filtered off in the usual way with an

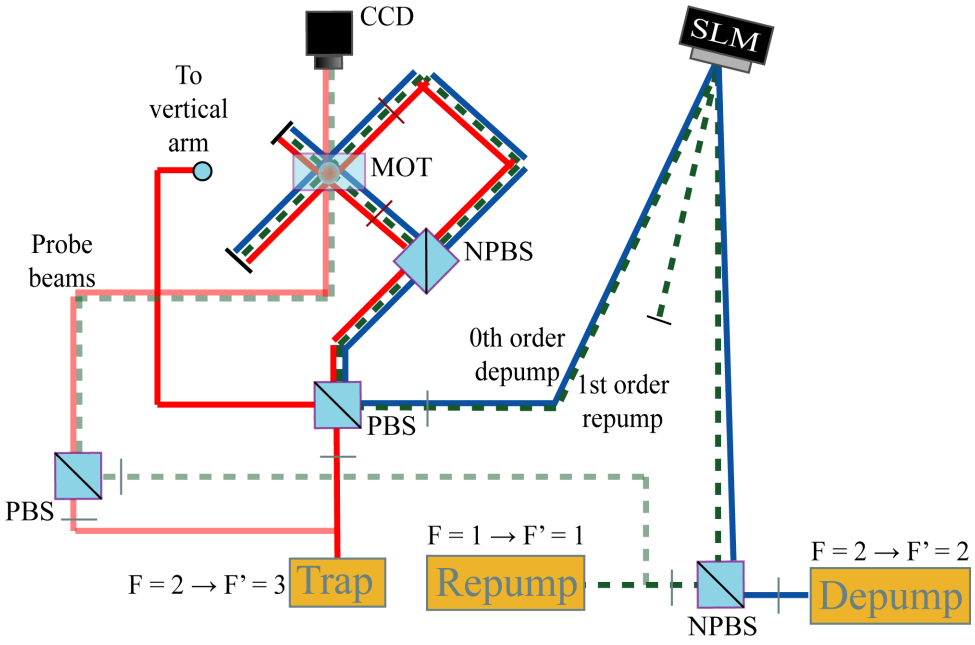

Figure 4.10: Experimental setup for the dark SPOT experiment.The key differences in the SPOT experiment from the standard MOT setup are the addition of the depump laser and SLM. The Trap laser is prepared as before. The SLM is used to shape the Repump beam 1st order and anti-shape the Depump beam 0th order in the setup more closely shown in Fig. 4.11 The combined Repump/Depump pair combine with the trap in the two horizontal arms of the MOT setup as before. Additionally a small portion of the Repump light is now taken for use as a pumping and probe beam on the same axis as the Probe beam from the standard MOT setup.

intensity profile chosen by the phase and intensity information on the SLM. The Depump beam input angle to the SLM is set such that the 0th order, the anti-shaped mode, is exactly overlapped with the 1st order of the repump. This alignment has the effect of the Depump filling the hole made in the Repump beam by the pattern on the SLM. The 0th order anti-shaping is shown alone in the Repump beam. The beam naturally has a halo of "extra" intensity from where the input Gaussian mode has not overlapped with the desired hologram. This outer halo of unshaped light can be removed by

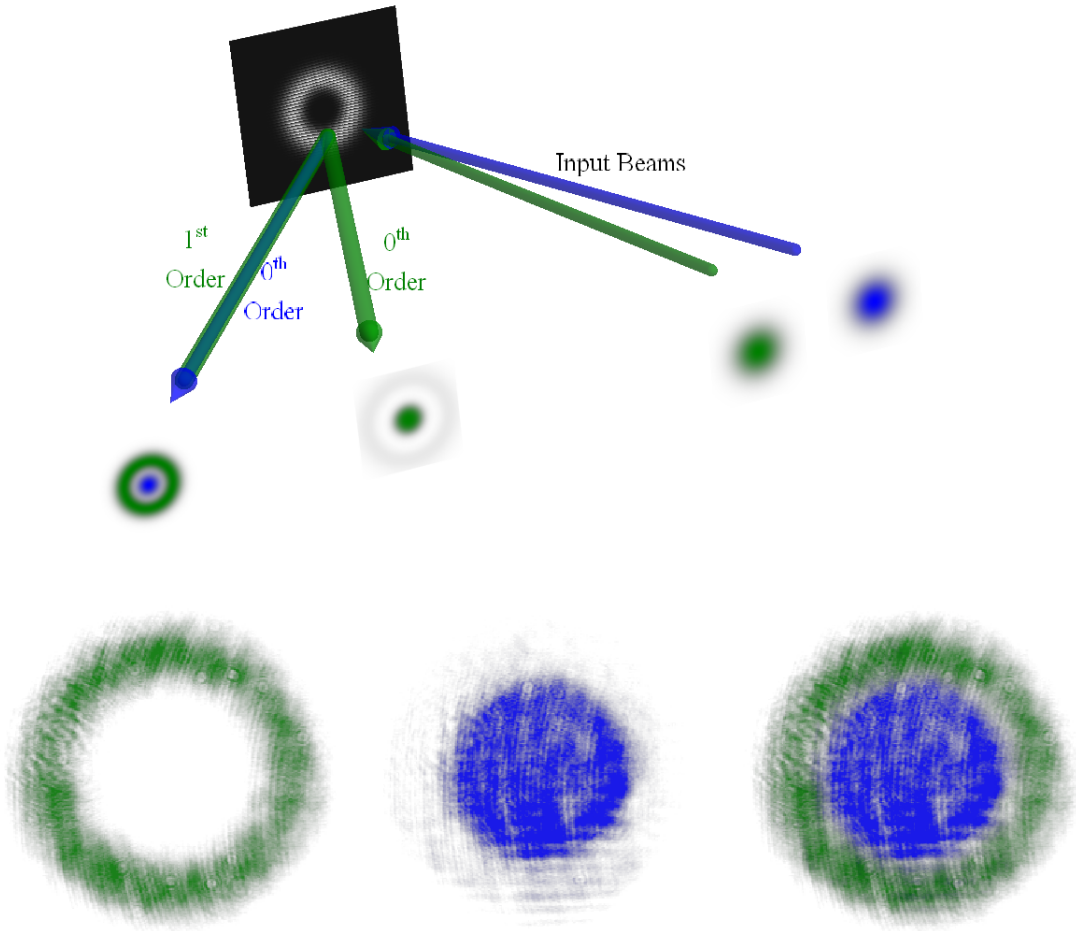

Figure 4.11: **Top:** Zoom in of the SLM setup in the SPOT experiment. The Repump beam is shown in green and the Depump in Blue. Angles are exaggerated and other orders are suppressed for clarity. **Bottom:** Example images of Repump/Depump pairing. From left to right: Repump beam 1st order shaped into and LG mode of $l = 5$ $p = 0$. Middle: Depump beam Anti-shaped from $l = 5$ hologram. Right: Combine Repump/Depump beam.

adding an extra grating with a different grating period or direction around the desired hologram if necessary. Experimentally generated images of the combined Repump/Depump beam and the individual Repump and Depump modes are shown in the bottom of Fig. 4.11.

4.4 Measurement Technique

Measurements in the SPOT experiment consist of 3 separate loading processes all performed in exactly the same way followed by 3 different measurements. After each loading phase a different set pumping and absorption beams are triggered in order to measure 3 things: the number of atoms in the bright state, the number of atoms in both bright and dark states together, and the size of the SPOT. Each of these measurements consists of a timing sequence similar to that in Fig. 4.12, which in particular details the timings for measuring the number of atoms in both the bright and dark states.

The general SPOT loading sequence and measurement is as follows. First the MOT is loaded as per normal to collect atoms in the trap, next the loading parameters are switched such that atoms are loaded into the dark SPOT. Various direct absorption measurements are then performed to determine the number of bright state and dark state atoms as well as the size of the dark state trap in order to calculate SPOT peak density.

In detail the loading and measurement process is as follows. In each of the 3 sequences there is a 6s loading process in the standard MOT state with a Gaussian Repump beam, i.e. a grating only on the SLM. During this time $3{\times}10^8$ atoms are loaded into the MOT. At the end of this loading phase the SLM is switched from a grating to the desired beam with a hole on the beam axis to be used in the SPOT. This switch of the SLM uses a secondary grating to the side of the main pattern to diffract the extra light from the 0th order of the AOM onto a photodiode which triggers the rest of the experiment. After this trigger the Depump beam is switched on via an AOM for a pre-determined amount of time during which the SPOT is loaded with up to 1.5×10^8 atoms. After this Depump loading time has alloted, the Trap, Repump, Depump, and Anti-Helmholtz coils are switched off. To account for its rise time 800μs prior to this the quantisation field is switched on for the first and second measurements.

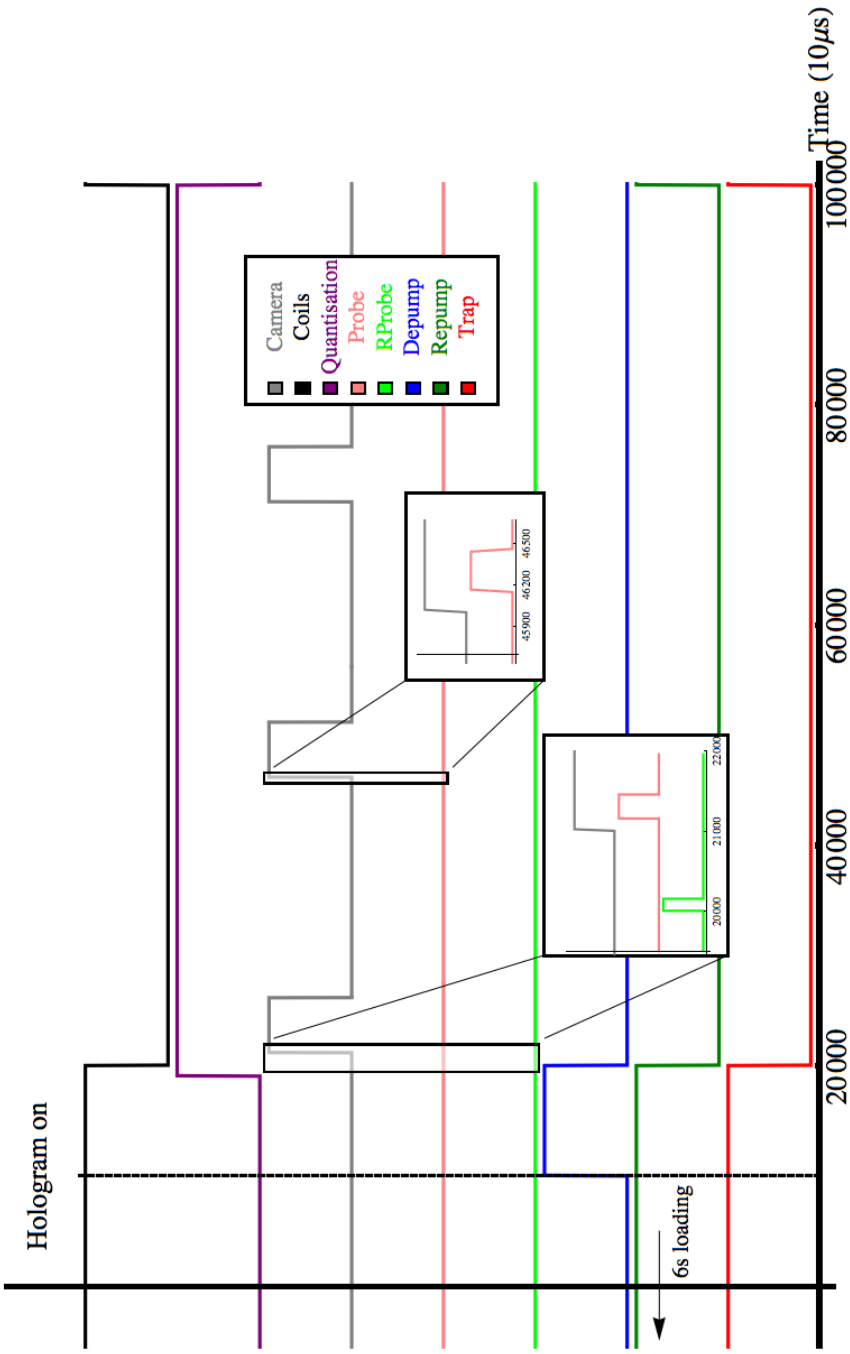

Figure 4.12: Example timing of all variables in the SPOT experiment. Specifically this graph details the timings for measuring the total number of atoms in both bright and dark states.

After the above SPOT loading phase in the first experiment the Probe beam is switched on for 3000μs after a 5000μs delay to allow the cloud to expand and the standard absorption imaging is performed as described in the MOT chapter. This measures the number of atoms in the bright state, N_B.

In the second measurement stage before the Probe beam is switched on, the RProbe beam is switched on for 1500μs in order to pump atoms collected in the Dark state into the **F** = 2 ground state via the excited states. The cloud is then allowed to ballistically expand for 10000μs (longer this time to account for the increase in atom number) after which standard absorption imaging on the **F** = 2 ground state is performed again. This measures the total number of atoms present in both hyperfine ground states, N_T. At this point we can determine the number of atoms in the ground state, i.e. in the SPOT, which is $N_D = N_T - N_B$.

In the third stage standard absorption imaging is performed again, however this time using the RProbe beam only, for 1000μs pulse time. As there is no stretched state from **F** = 1 to the excited states, as there is in **F** = 2, $m_F = 2$ to **F'** = 3, $m_{F'} = 3$ transition, this measurement is extremely weak and we cannot accurately determine the number of atoms in the ground state from the absorption image. This measurement however does detect some of the atoms (approximately 10%) which provides us with the size of the dark state cloud as the size should be independent of absorption signal strength, assuming a Gaussian distribution. Fig. 4.13 shows the relative shape of both the SPOT and MOT generated experimentally, from absorption and fluorescence imaging respectively.

The peak density of atoms in the dark state can be calculated from the equation below, if we assume a gaussian distribution,

$$n_0 = \frac{N_D}{(2\pi)^{\frac{3}{2}}\,\sigma_x\sigma_y\sigma_z}. \tag{4.11}$$

In this case we take $\sigma_z = \sigma_x$ as these widths are both in the horizontal plane

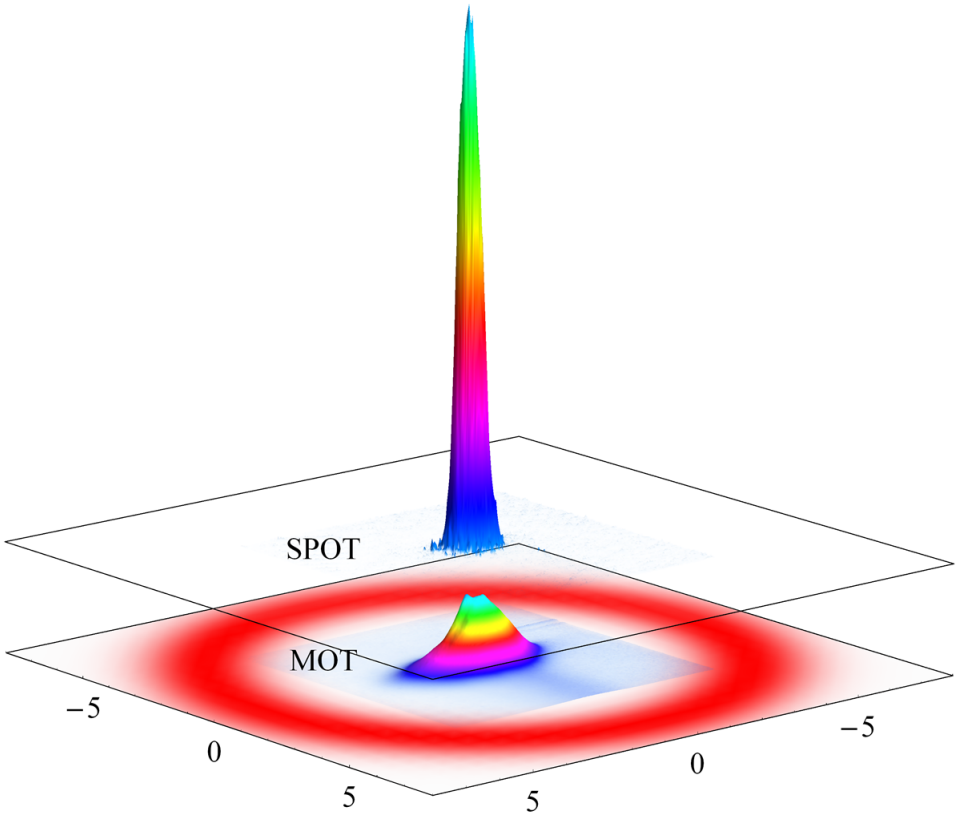

Figure 4.13: Experimental images of SPOT and MOT both plotted such that their 3D volume represents the number and density of atoms in the respective traps. A theoretical 2D image of the LG beam used to generate this SPOT trap is shown below the images for comparison.

of the setup and should therefore experience the same magnetic field shape from the horizontal helmholtz coils.

4.5 SPOT Optimization

4.5.1 Magnetic Field

The first parameter optimized in the SPOT experiment was magnetic field strength. The standard MOT requires a magnetic field strong enough to separate the m_F sub-levels within the atoms enough to create a closed loop transition is created for the trapping beam frequency. The field needs to be weak enough however such that the trapping volume of the MOT is not adversely affected as stronger fields result in a smaller trapping volume for one fixed trap beam detuning.

In the SPOT however we theorize that increased magnetic field strength may reduce the probability of atoms in the centre of the trap being recycled by stray Repump photons. The effects of increasing magnetic field strength (coil current) from the standard MOT value of 10G/cm (2A) on dark state density and atom number in the bright and dark states are shown in Fig. 4.14. In this figure we see as one might expect, a general decrease in atom number as the field strength is increased and the optimal MOT conditions previously calibrated are lost. However at 3A, approximately 13G/cm, we see a distinct peak in the number of atoms in the dark state. As of writing this is not fully understood but we theorize it is due to a near perfect balance being achieved between the strength of the Depump field in the centre of the trap, such that pumping to the dark state is ideal but the Depump is not so strong as to push atoms out of the dark state region altogether. As at this current the density appears to have reached the maximum value before essentially leveling off, the coil current was maintained at this value for all SPOT measurements. There is some suggestion that higher densities may be achievable at higher currents however our equipment could only be safely operated at 3A without overheating. All figures in these optimization experiments were taken using a Circle beam with a radius of 150px on the

SLM corresponding to approximately 6mm at the trap.

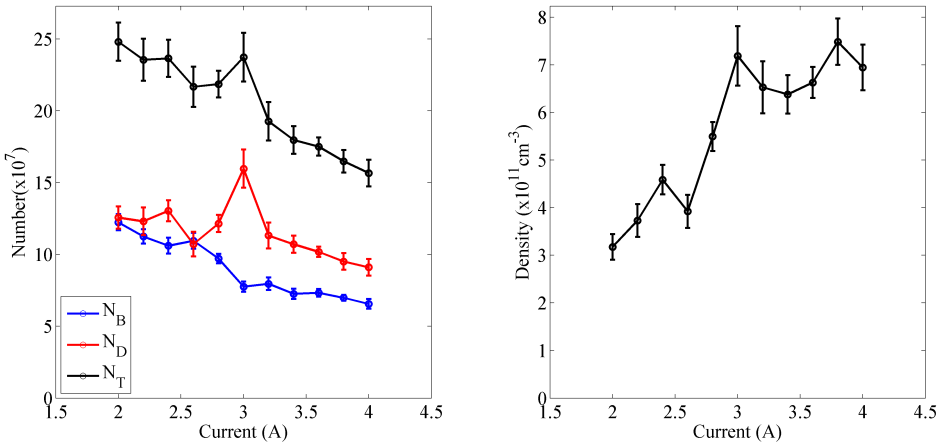

Figure 4.14: Left: Number of atoms in the bright, (blue) dark, (red) and both (black) states vs coil current. Right: Density of atoms in the dark state vs coil current.

4.5.2 Depump Power

In a very similar set of experiments the ideal Depump power was determined. The ideal Depump power however was found to 0.5mW over a 6mm radius beam.

4.5.3 Trap Frequency

With the new coil field density set we then investigated varying the trap frequency detuning ±5MHz from the ideal MOT detuning previously measured to be 17MHz, the results of this test are shown in Fig. 4.15. We observe a peak in density of atoms in the dark state at 17MHz detuning, the same as before for the MOT. Interestingly above 17MHz we see a quick fall in density while below 17MHz the fall is more gradual. At this point in time we have no viable explanation for this effect. In the number measurements

we see a corresponding slight change in gradient of the decrease in number of atoms. The number of atoms shows an overall gentle decrease over time from 12MHz as the experiment is run, however we attribute this to slow decline in background pressure in the cell while these measurements were taken. After this result the Trap frequency remained at 17MHz detuning for the rest of the experiments.

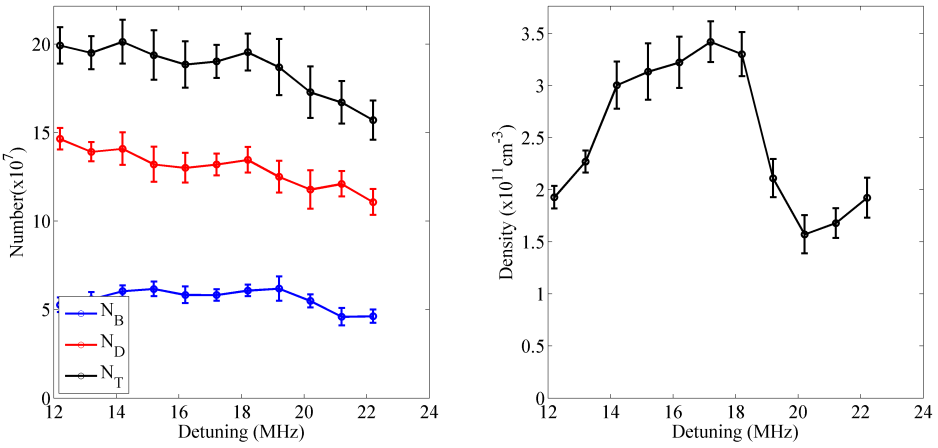

Figure 4.15: Left: Number of atoms in the bright, (blue) dark, (red) and both (black) states vs Trap detuning. Right: Density of atoms in the dark state vs coil current.

4.5.4 MOT Load Time

Currently the best state-of-the-art atom optics experiments utilize MOTs with atom numbers greater than 10^9 atoms, while our MOT is currently limited to around 3×10^8 atoms cm^{-3} at maximum capacity. This is also interesting because other high density schemes require high starting numbers while ours doesn't and still works for even lower initial numbers. To gain some understanding on the likely behaviour of the SPOT in higher number MOT setups we invesitgated the performance of the SPOT as more and more atoms were added to the MOT it is loaded from. This was done by performing the

experiment between 0.5 and 10s MOT loading time. Fig. 4.16 shows the results from increasing MOT load time, i.e. increasing atom number in the MOT vs number and this atom number vs density in the SPOT. We observe that the density in the SPOT appears to increase linearly with atom number as expected from equation 4.11. This shows great promise for introducing this type of setup in a higher atom MOT experiment.

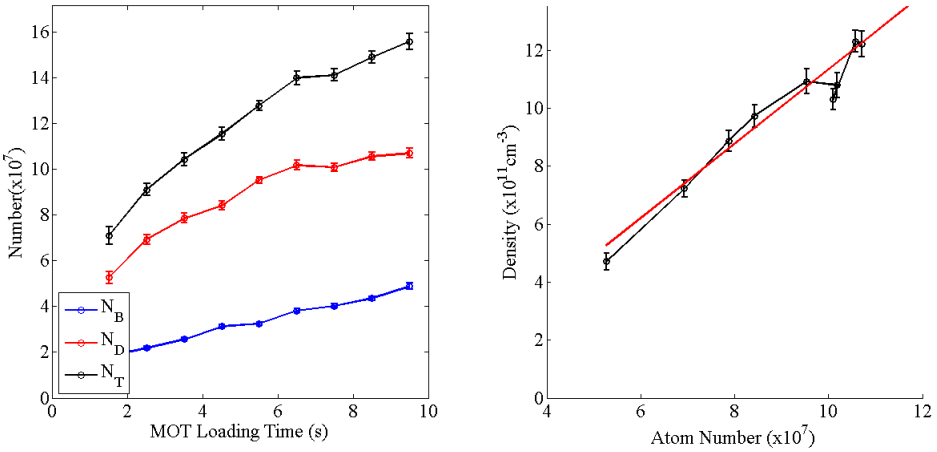

Figure 4.16: Left: Number of atoms in the bright, (blue) dark, (red) and both (black) states vs MOT loading time. Right: Density of atoms in the dark state vs atom number in the dark state with linear fit shown in red.

4.5.5 SPOT Load Time

The next optimisation was performed as a function of the SPOT loading time which we define as the length of time the depump beam is switched on after the SLM pattern, and therefore Repump Intensity field, has been changed to a circle mode. Results of this test are shown in Fig. 4.17. Two distinct regimes can be observed in the loading time variation. In the first regime we observe a very steep rise in SPOT number/density between 0 and 75ms. During this time we theorise that the characteristics of the trap more closely resemble that of a temporal dark SPOT than that of the spatial dark

SPOT we aim to create. In the temporal dark SPOT the dynamics of the trap are dominated by the addition of Depump intensity in time rather than the spatially varying intensity profile in the Repump. We note interestingly that during this period densities of an order of magnitude greater than the MOT can still be observed. We theorize that this effect may be due to the pumping effect of the depump laser dominating the behaviour of the trap pumping atoms into the F = 1 state which rush towards the trap centre. The long term behaviour of the trap is then dominated by the shaped Repump geometry where the F = 1 atoms are no longer resonant with any light in the trapping volume.

After 100ms we see the characteristic behaviour of the spatial dark SPOT over short timescales of an approximately linear increase in density with a slowly decreasing dark state atom number as atoms are lost to collisions and other loss processes.

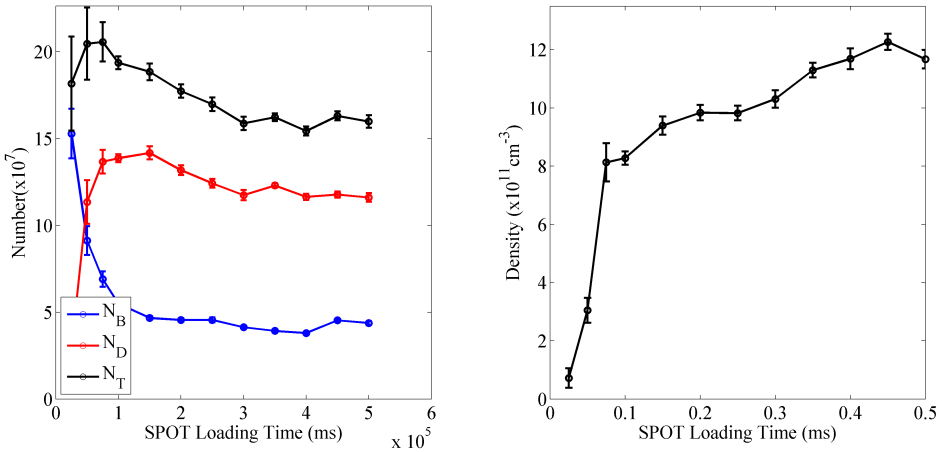

Figure 4.17: **Left:** Number of atoms in the bright, (blue) dark, (red) and both (black) states vs SPOT loading time up to 0.5s. **Right:** Density of atoms in the dark state vs SPOT loading time up to 0.5s.

The long time dependence of the SPOT over 4s was tested seperately and is shown in Fig. 4.18. In the long time dependence we observe a relatively

steady decay in both the density and atom number in both states. Again however ever after long time scales of 4s we still observe an order of magnitude increase over MOT density. We attribute this loss to the usual losses present in the MOT such as collisional and absorption of re-emitted light.

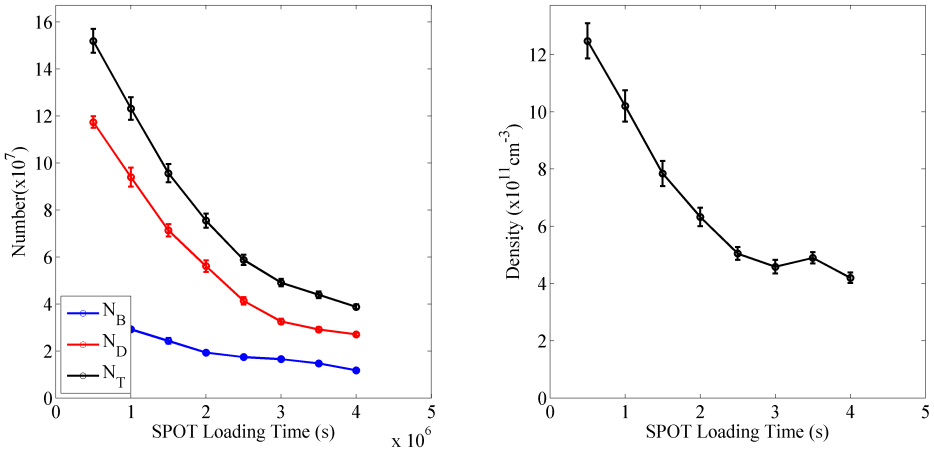

Figure 4.18: Left: Number of atoms in the bright, (blue) dark, (red) and both (black) states vs Long SPOT loading time up to 4s. Right: Density of atoms in the dark state vs atom number in the dark state up to 4s.

4.5.6 Circle Radius and l Number

Measurements from this point onward are taken with varying Repump geometries during the SPOT loading phase. The dependency tested which we believed to be most fundamental to the advantage of our method over previous efforts was the effect of increasing the size of the hole in the repump beam vs SPOT peak density. The first Repump intensity field tested was a Circle mode hologram with varying circle radius, the results of which are shown in Fig. 4.19. In circle radius variation we see a peak in density of atoms in the dark state of 1.7×10^{12} atoms cm^{-3} at a Circle radius of 6mm. This radius counter-intuitively is much larger than the SPOT size itself which is of the order 200μm. The ring size much more closely matches the capture

volume of the MOT which we estimate from our trapping beam size to be of the order 1cm in radius. In this case it appears that good overlap with the trapping beams is a much more dominant process than having a hole size which matches the SPOT size. Additionally the Circle radius mode can only create a perfect zero in the centre of the beam with a sufficiently large radius hole in the hologram which will also add to the necessity for a larger hole size Repump beam. Either side of the density peak we see an almost linear decrease in density with a smooth decrease in atom number. Interestingly the slope of the decrease with larger Circle radius is less than that with smaller circle radius. We attribute this difference in slope to the difficulty in creating a perfect zero in the beam profile due to diffraction when smaller holes are used.

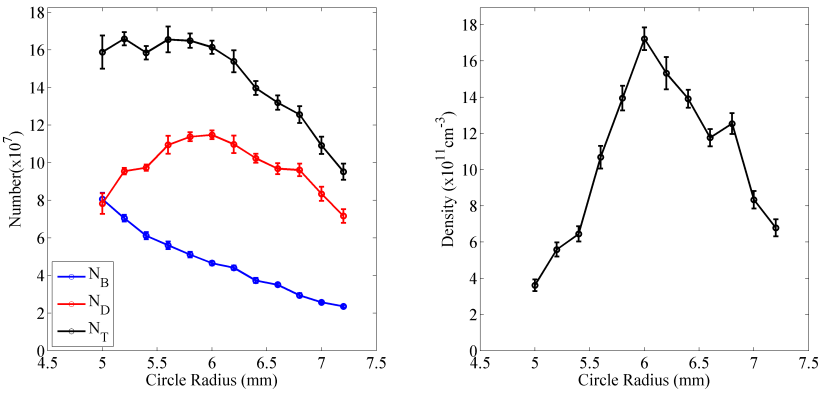

Figure 4.19: Left: Number of atoms in the bright, (blue) dark, (red) and both (black) states vs SPOT loading time up to 4s. Right: Density of atoms in the dark state vs atom number in the dark state. Sizes are quoted at the position of the MOT.

The second set of Repump field shapes tested were that of Laguerre-Gaussian modes at multiple beam waists. Three beam waists were tested, $\omega = 1.88$, 2.81, and 3.75mm respectively (at the position of the MOT) and the results of which are shown in Figs. 4.20, 4.21 and 4.22. In these l mode tests we see several similarities to the behaviour of Circle modes. For $\omega =$

1.88 we see a peak in density at $l = 19$ of 1.5×10^{12} atoms cm^{-3} for 1.2×10^{8} atoms. This corresponds to a peak-to-peak diameter of approximately 12.2mm, almost exactly the same as for the Circle modes. Additionally we also observe similar behaviour either side of the peak in density and atom number, namely a sharp decline for smaller l modes in density and a slower decline for larger l modes. The number of atoms in the dark state curve is smoother than in density as before but this time moving slightly towards a sharper decline for lower peak-to-peak radius and vice versa. For $\omega = 2.81$mm and 3.75mm this evolution in behviour continues. We see in number a much steeper reduction in atom number for smaller l modes than for higher again. More interestingly however we begin to see a reduction in the position of the peak density as a function of peak-to-peak radius in the LG mode. A possible reason for this is that larger beam waist modes naturally keep a good overlap with the MOT trapping volume for low l modes while still managing to create a large enough perfect zero to allow for SPOT operation. Throughout these experiments the largest peak density was achieved using circle modes and was approximately 1.7×10^{12}atoms cm^{-3}, at least one order of magnitude greater than previous efforts in Rubidium compression and almost 2 orders of magnitude greater than the density of a standard MOT.

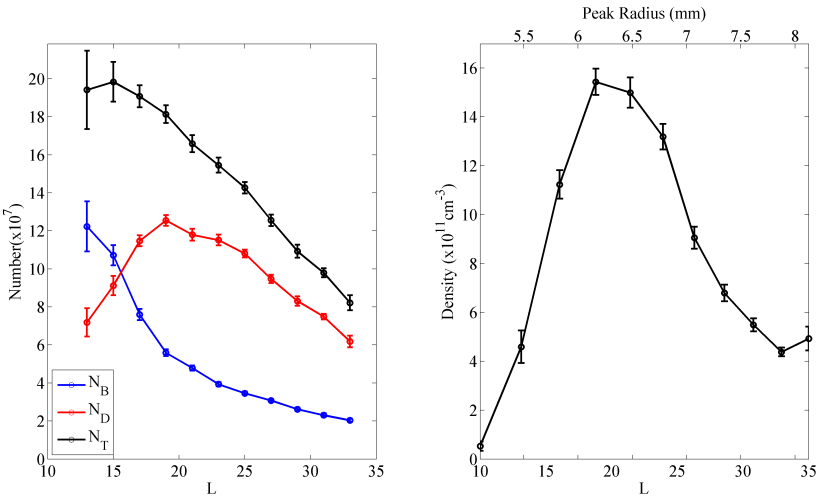

Figure 4.20: Left: Number of atoms in the bright, (blue) dark, (red) and both (black) states vs l value (written as L on the axis label) at a beam waist of $\omega = 1.88$mm. Right: Density of atoms in the dark state vs l value at a beam waist of $\omega = 1.88$mm. Sizes are quoted at the position of the MOT.

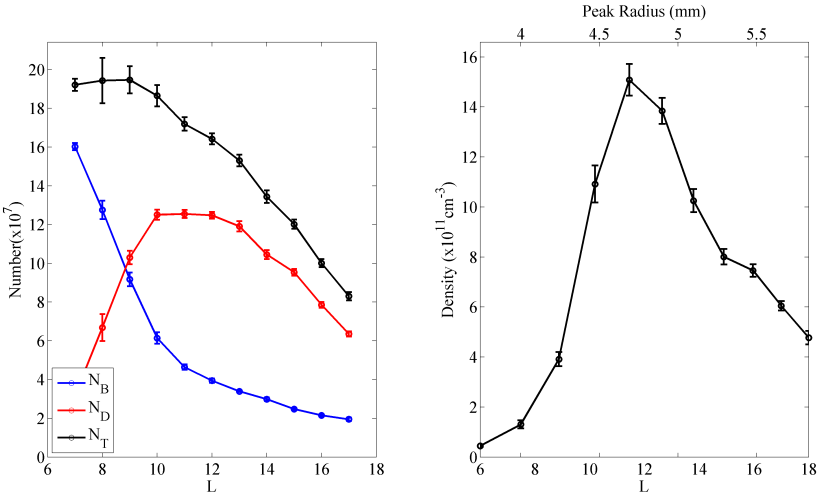

Figure 4.21: Left: Number of atoms in the bright, (blue) dark, (red) and both (black) states vs l value (written as L on the axis label) at a beam waist of $\omega = 2.81$mm. Right: Density of atoms in the dark state vs l value at a beam waist of $\omega = 2.81$mm. Sizes are quoted at the position of the MOT.

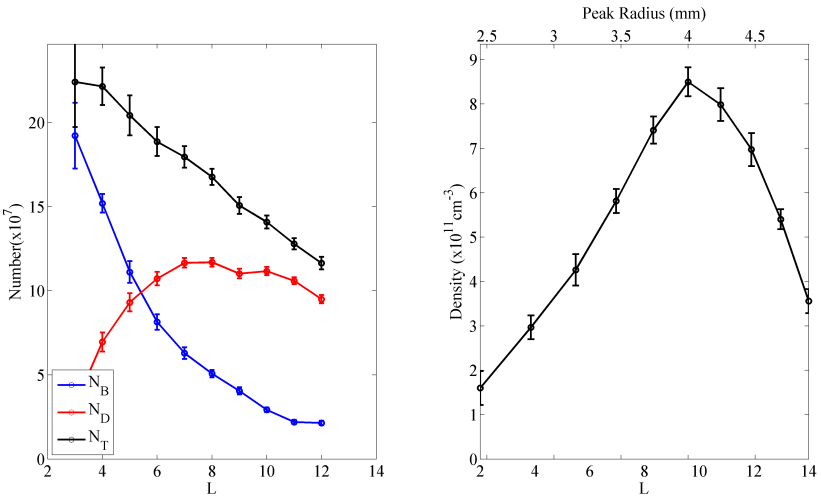

Figure 4.22: Left: Number of atoms in the bright, (blue) dark, (red) and both (black) states vs l value (written as L on the axis label) at a beam waist of $\omega = 3.75$mm. Right: Density of atoms in the dark state vs l value at a beam waist of $\omega = 3.75$mm. Sizes are quoted at the position of the MOT.

4.6 SPOT Temperature

In previous MOT compression experiments a side effect of increasing the density inside the trap was heating of the atomic cloud. To understand the effect of the SPOT loading process on the temperature of the ground state atoms we performed temperature measurements based on successive ground state absorption measurements. Usually temperature measurements are performed by taking successive fluorescence measurements of the bright state atoms in the MOT at different expansion times. We apply a corresponding technique to atoms in the dark SPOT. By measuring the FWHM of the SPOT at different expansion times we gain information on the kinetic energy and therefore temperature of the atoms within. As the SPOT atoms are trapped in the ground state we cannot easily perform a fluorescence measurement on these atoms. Instead our system uses a series of direct absorption

measurements of the $\mathbf{F} = 1$ atoms in exactly the same process as step 3 of the measurements described previously. Taking into account the pulse time of the absorption beam and using the same fitting equation used for MOT temperature measurements, Eqn. 3.3, the temperature should be of the form

$$T = \frac{m_{\mathrm{Rb}}\sigma_t^2}{k_{\mathrm{B}}\left(t + t_{abs}\right)^2}, \tag{4.12}$$

where σ_t is the standard deviation of a gaussian fit to the cloud shape at time t and t_{abs} is the pulse time of the probe beam. For each absorption image we fit the size, σ of the SPOT in both x and y directions effectively giving us two temperatures. There will be some small differences in the temperature in x and y due to external perturbations such as residual Earth magnetic field and gravity. The fits of SPOT size vs expansion time and the associated temperature from these fits are shown in Fig. 4.23. Both temperature fits appear to fit the data very closely and result in similar temperatures of $T_x = T_z = 78.9\mu K$ and $T_Y = 85.3\mu K$ for the ground state atoms. The temperature in the y-direction is slightly higher than that in the horizontal plane most likely due to residual influence of gravity. This data suggests that not only does the SPOT result in 2 orders of magnitude increase in density from the MOT but that there is no adverse heating involved in the increase in density. In fact the data seems to suggest that the temperature decreases slightly from the measured MOT value of 116μK, however this is not a significant decrease.

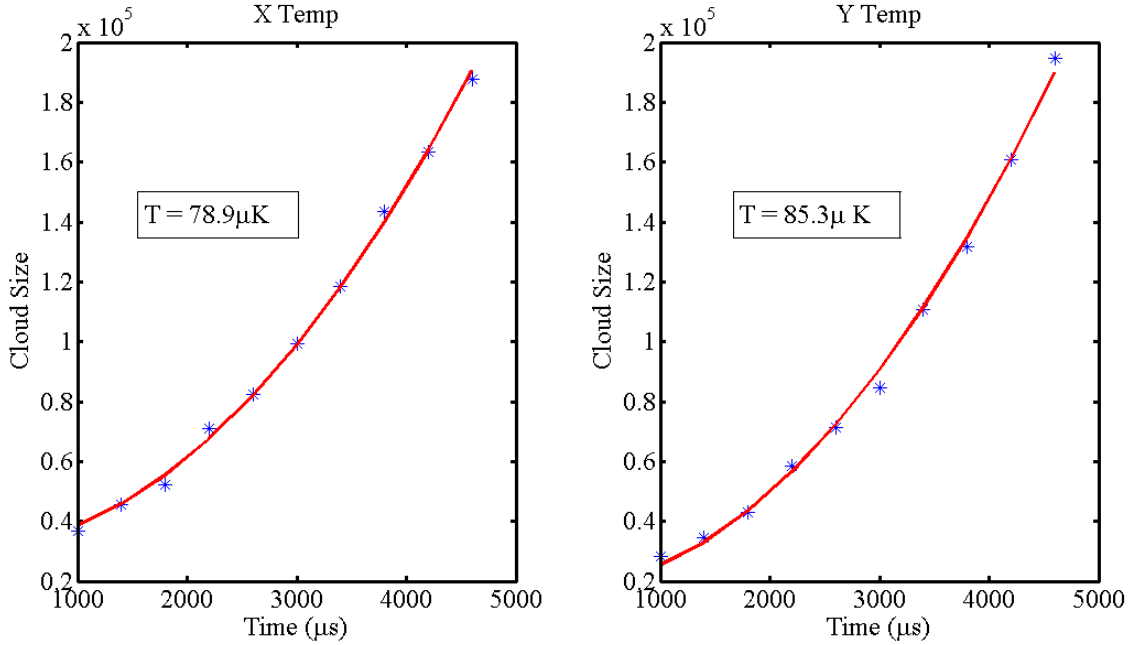

Figure 4.23: Left: SPOT size vs expansion time with temperature fit in x direction. Right: SPOT size vs expansion time with temperature fit in y direction. Combined both fits result in an average temperature in the SPOT of 82.1μK.

In addition to giving us the temperature we can use the fitted graphs to extrapolate back to the density of the SPOT at time $t = 0$. After this correction we come to a peak density in the SPOT of approximately 2.5×10^{12} atoms cm^{-3} for 1.2×10^8 atoms.

4.7 Actual fractional population in the dark state

The peak density in this experiment is found to occur when 70% of the total atoms in the MOT system have transfered into the SPOT. Analysis of the images in Fig. 4.13 allow us to determine the fractional population, p, in the

bright state by analysing the relative population in the MOT and SPOT of atoms constricted to the SPOT dominated volume only. From this we find a fractional population $p = 0.04$. Plugging this and our other MOT parameters gives a theoretical maximum density in the SPOT of 6.5×10^{12} atoms cm^{-3}. While there may be other effects in place that will limit our density further we believe this shows great promise for implementing our dark SPOT trap in higher atom number systems.

4.8 Summary and Further Work

In summary we have developed a dynamic dark SPontaneous force Optical Trap (dark SPOT) using a Repump beam shaped in various intensity fields with an anti-shaped depump beam via a novel Spatial Light Modulator setup. In this setup the size of the hole in the Repump could be optimized precisely for ours or any other MOT parameters. This hole in the Repump and Depump beam combine to pump atoms into the $\mathbf{F} = 1$ hyperfine ground state in a ^{87}Rb MOT where they are sheltered from all laser fields present in the experiment at that time. This technique is exploited primarily to increase the densities of these atoms by almost 2 orders of magnitude from the standard MOT limit and by 1 order of magnitude greater than in previous MOT compression techniques utilized in Rubidium. The peak density reached was approximately 2.5×10^{12} atoms cm^{-3} for 1.2×10^{8} atoms confined in the SPOT. We have shown that these large densities are achievable using both Laguerre-Gaussian modes and simple intensity masked beams. Both shaping options give density increases in the SPOT experiment with hole sizes several times larger than the SPOT itself. We attribute this behaviour to the difficulty in fully eliminating all Repumping light from the centre of the trap either from the beam itself or from reemission of Repumping light by atoms inside the capture volume. This behaviour has not been observed in other SPOT experiments to our knowledge as other non-dynamic methods

require an ever present hole in the Repump beam. This necessitates smaller hole size in order to preserve MOT atom number whereas our method does not require this. We have shown that this method could have promise in higher atom number traps to the goal of creating even higher peak densities as we observe a linear increase in SPOT density with increasing atom number. This could prove to be very useful in such traps as a more efficient route to BEC where a higher percentage of initial atoms in the MOT are retained. Our trap achieves peak density while maintaining approximately 70% of the atoms initially in the MOT. We have also observed the relatively long stability of the SPOT by testing loading times up to 4s. At these long time scales we still observe a increase of atom density of over two orders of magnitude, persistent over 500ms which would allow significant time for experiments on initially denser atomic clouds.

In addition to these increases in peak density we have also observed that the temperature of the dark state atoms does not increase during compression. In fact we observe a slight decrease in the temperature of the atoms when loaded into the SPOT. This drop in temperature is attributed to the decrease in absorption and reemission processes in the centre of the trap which usually dominate atom behaviour in the centre of the MOT.

Over the next year further work will be completed on this experimental setup using several aspects of the SPOT experiment and using the ground state trap itself. At the time of writing a study is being performed into the temperature profile of the atoms in the standard MOT using most of the techniques learned in the development of the SPOT experiment.

In the future our dark state trap may be used in the development of an experiment in controlling the populations in a four level system using the phases of four separate light beams. Being able to pump the majority of the atoms from a MOT to the ground state could be extremely useful in this type of experiment as this could be used as a known building block for transferring atoms to the other 3 levels using the phase interference of the

four beams.

The likely next evolution of this experimental setup will include a far detuned laser for producing an optical dipole trap. An Optical Dipole Trap uses a tightly focused laser detuned, often by hundreds of nm, from optical resonance. If detuned in the Red direction atoms are attracted to intensity maximums, if blue detuned they are attracted to intensity minimums. Usually as a result of the tight focusing and relatively high temperature atoms in a MOT a large percentage of atoms are lost during transfer to the dipole trap. Our slightly colder and much denser trap could possibly allow for a much higher transfer of number of atoms to the dipole trap.

References

[1] E. L. Raab, M. Prentiss, Alex Cable, Steven Chu, and D. E. Pritchard. Trapping of neutral sodium atoms with radiation pressure. *Phys. Rev. Lett.*, 59:2631–2634, Dec 1987.

[2] I. M. Sokolov, D. V. Kupriyanov, R. G. Olave, and M. D. Havey. Light trapping in high-density ultracold atomic gases for quantum memory applications. *J. Mod. Opt.*, 57(19, SI):1833–1840, 2010.

[3] Alexander I. Lvovsky, Barry C. Sanders, and W. Tittel. Optical quantum memory. *Nature Phot.*, 3(12):706–714, DEC 2009.

[4] Wolfgang Petrich, Michael H. Anderson, Jason R. Ensher, and Eric A. Cornell. Behavior of atoms in a compressed magneto-optical trap. *J. Opt. Soc. Am. B*, 11(8):1332–1335, Aug 1994.

[5] L.-S. Yang, B.-T. Han, D.-S. Hong, T. A. Mohamed, and D. J. Han. Loading and Compression of a Large Number of Rubidium Atoms Using a Semi-Dark Type Magneto-Optical Trap. *Chinese Journal of Physics*, 45:606, December 2007.

[6] Marshall T DePue, S Lukman Winoto, D.J Han, and David S Weiss. Transient compression of a mot and high intensity fluorescent imaging of optically thick clouds of atoms. *Optics Communications*, 180(1-3):73 – 79, 2000.

[7] Wolfgang Ketterle, Kendall B. Davis, Michael A. Joffe, Alex Martin, and David E. Pritchard. High densities of cold atoms in a *dark* spontaneous-force optical trap. *Phys. Rev. Lett.*, 70:2253–2256, Apr 1993.

[8] D. Sesko, T. Walker, C. Monroe, A. Gallagher, and C. Wieman. Collisional losses from a light-force atom trap. *Physical Review Letters*, 63:961–964, August 1989.

[9] M. H. Anderson, W. Petrich, J. R. Ensher, and E. A. Cornell. Reduction of light-assisted collisional loss rate from a low-pressure vapor-cell trap. *Phys. Rev. A*, 50:R3597–R3600, Nov 1994.

[10] P.L. Chapovsky. Spectral characteristics of cold rubidium atoms in a dark magneto-optical trap. *Journal of Experimental and Theoretical Physics*, 103(5):711–719, 2006.

[11] M. Gurvitch. Ioffe-regel criterion and resistivity of metals. *Phys. Rev. B*, 24:7404–7407, Dec 1981.

[12] Tom Bienaimé, Giovanni Barontini, Laure Mercier de Lépinay, Louis Bellando, Julien Chabé, and Robin Kaiser. Fast compression of a cold atomic cloud using a blue-detuned crossed dipole trap. *Phys. Rev. A*, 86:053412, Nov 2012.

[13] S. Friebel, R. Scheunemann, J. Walz, T.W. Hänsch, and M. Weitz. Laser cooling in a co2-laser optical lattice. *Applied Physics B*, 67(6):699–704, 1998.

[14] T. L. Gustavson, A. P. Chikkatur, A. E. Leanhardt, A. Görlitz, S. Gupta, D. E. Pritchard, and W. Ketterle. Transport of bose-einstein condensates with optical tweezers. *Phys. Rev. Lett.*, 88:020401, Dec 2001.

[15] Olivier Houde, Demascoth Kadio, and Laurence Pruvost. Cold atom beam splitter realized with two crossing dipole guides. *Phys. Rev. Lett.*, 85:5543–5546, Dec 2000.

[16] Tim Freegarde and Kishan Dholakia. Cavity-enhanced optical bottle beam as a mechanical amplifier. *Phys. Rev. A*, 66:013413, Jul 2002.

[17] N. V. Morrow, S. K. Dutta, and G. Raithel. Feedback control of atomic motion in an optical lattice. *Phys. Rev. Lett.*, 88:093003, Feb 2002.

[18] M. D. Barrett, J. A. Sauer, and M. S. Chapman. All-optical formation of an atomic bose-einstein condensate. *Phys. Rev. Lett.*, 87:010404, Jun 2001.

[19] Thad Walker, David Sesko, and Carl Wieman. Collective behavior of optically trapped neutral atoms. *Phys. Rev. Lett.*, 64:408–411, Jan 1990.

[20] Volume Number July-August, Eite Tiesinga, Carl J. Williams, Paul S. Julienne, Kevin M. Jones, Paul D. Lett, and William D. A spectroscopic determination of scattering lengths for sodium atom collisions, Jul 1996.

[21] M.J. Padgett and L. Allen. The poynting vector in laguerre-gaussian laser modes. *Optics Communications*, 121(1-3):36 – 40, 1995.

[22] Wai-Hon Lee. Method for converting a gaussian laser beam into a uniform beam. *Optics Communications*, 36(6):469 – 471, 1981.

5 | The Blue Light Experiment

5.1 Introduction

Coherent blue light generation from nonlinear atomic and non-atomic media has been studied in many different configurations for a number of years now. In non-atomic media coherent blue light generation has been shown in Lithium Niobate waveguides [1, 2] and frequency doubling [3, 4, 5]. In atomic vapours coherent blue generation has been shown in hot Cesium vapour [6] and in Rubidium, [7, 8, 9, 10] producing of the order of μW of blue light in both cases. Recently an experiment in Strathclyde University conducted by, then PhD student, Dr. Aline Vernier reported the production of up to 1.1mW of 420nm blue light from a heated ^{85}Rb vapour [11]. This experiment and further unpublished initial experimentation by Dr. Vernier act as the building blocks for the work presented in this chapter.

The interaction between light and matter can take on a nonlinear nature under one of two conditions: Either the intensity of the light is sufficient to induce nonlinear effects or there is a natural resonance between the light and the properties of the material. In atomic vapours nonlinear effects can become apparent even at low light intensities allowing the investigation of phenomena like efficient frequency up-conversion [11], four-wave mixing [12], slow light [13] and image storage [14] using home built or inexpensive comercial diode lasers. In the blue light experiment we take advantage of four wave mixing (FWM) to produce light at 420nm from NIR pump light at 780nm

and 776nm with an additional beam generated at 5230nm. FWM like many nonlinear processes such as frequency doubling, sum and difference frequency generation and parametric down conversion, are said to be phase matched [15, 16, 17, 18]. Phase matching is governed by equation 1.11 Only when there is no phase mismatch, $\Delta k = 0$, do the four beams fully constructively interfere. The effect is analogous to the classical Mach-Zehdner Interferometer illustrated in Fig. 5.1. High effciency can be achieved in colinear and non-colinear phase matching depending on the structure of the nonlinear medium [19]. In this experiment we use colinear pumping with the same handedness polarisation, which was found to be most efficient setup in [11].

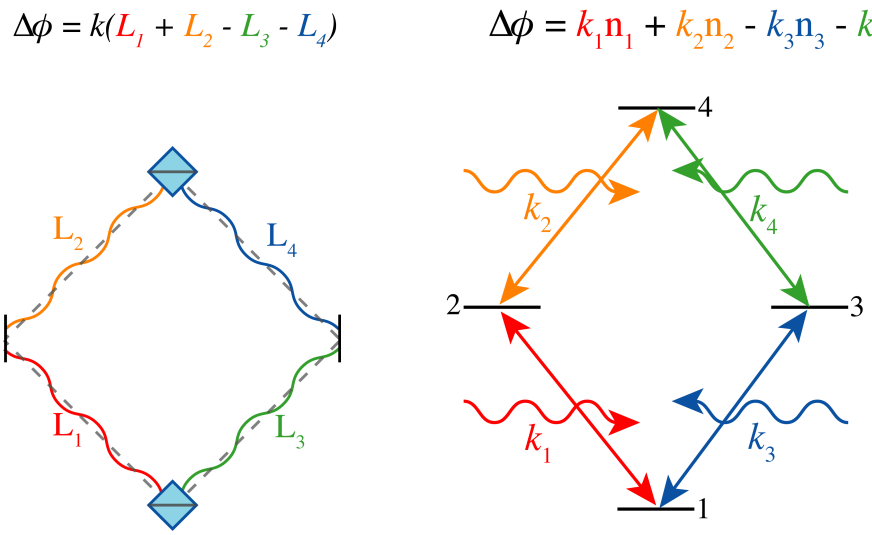

Figure 5.1: Comparison between Mach-Zehdner and an atom interferometer.

The phase matching equation, Eqn. 1.11, is also dependent on the relative refractive index of the material for each of the four waves. The refractive index of the atomic vapour will vary as a result of the the Optical Kerr effect. The Kerr effect is a nonlinear optical process usually only occuring at high intensity but possible at low intensities in atoms due to their lower saturation intensities [20, 21]. The refractive index of a nonlinear material is modified by the Kerr effect such that

$$n = n_0 + n_2 I \quad \text{where } n_2 = \frac{3}{4}\frac{Re(\chi^{(3)})}{n_0^2 \epsilon_0^2 c}. \tag{5.1}$$

In atoms this can be a dramatic effect close to resonance, [22], producing strong negative or positive lensing depending on the sign of the detuning. Kerr lensing can have a dramatic effect on phase matching and therefore four wave mixing efficiency, if one or more of the waves has a much greater non-linear susceptibility, than the others. Lensing on a subset of the beams will reduce the overlap of that beam with the other three modes, increasing k vector mismatch. It is these strong nonlinear effects at low light power (10s mW) that make atoms, such as Rubidium in our case, ideal for study of nonlinear effects.

The blue light experiment level diagram along with the pump and output wavelengths is shown in Fig. 5.2.

My contribution to this work is split up into 3 main areas made distinct from one another by increasing OAM content and complexity in the pump mode profiles. First a short study was conducted using gaussian pump fields in order to measure precisely chracteristics of the blue light such as confirming the optimum detuning from resonance and Kerr Lensing effects. Secondly we repeated some earlier measurements of coherent blue light production against the frequencies of the two pump modes using a combination of beat note and two-photon spectroscopy. Finally measurements of the effect of Kerr Lensing on the three observable frequencies around the frequency range of blue light production with particular attention on the 780nm beam and the effects seen at negative Kerr lensing.

Secondly the use of Laguerre-Gaussian modes as pump light was investigated specifically looking at their conversion through FWM to the 420nm mode. Kerr lensing results were repeated but for the most part the focus was on analysing the translation of the OAM to the blue beam. The OAM content transfered from the pump beams was shown to always appear in the output entirely in the blue beam. An analysis of the 3 dimensional overlap

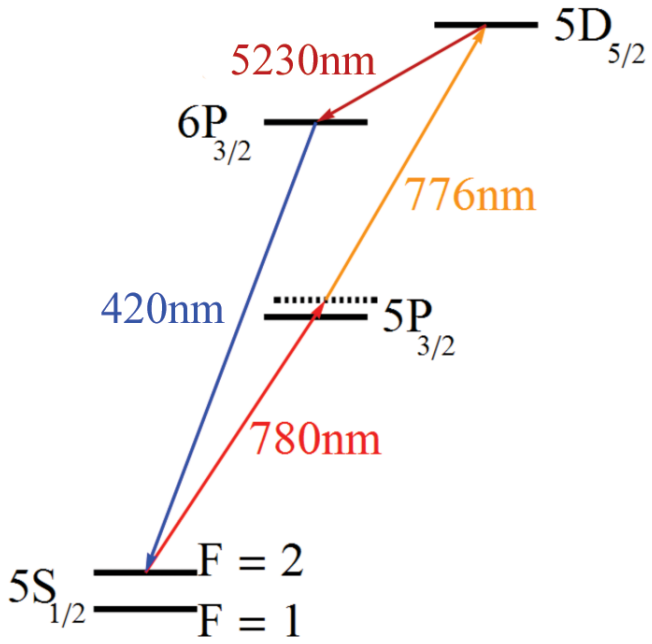

Figure 5.2: Blue light experiment level diagram: Two lasers at 780nm and 776nm are used as a two-photon pump beam to produce an unobserved 5.2μm beam and a 420nm output.

integral of the four modes was done and compared between the FWM here and typical very well known behaviour in similar Spontaneous Parametric Down-Conversion (SPDC) experiments to help explain the distribution of OAM in the output channels.

The third part of the experiment was focussed on the observation of the blue beam when simple superpositions of LG modes were used as pump light. Analysis of the distribution of OAM content in the blue beam sheds light on the effect of Gouy-phase matching in determining which modes are most efficiently converted to the blue. This behaviour best illustrates the quantum nature of the blue light experiment.

5.2 Theory - Two-Photon Spectroscopy

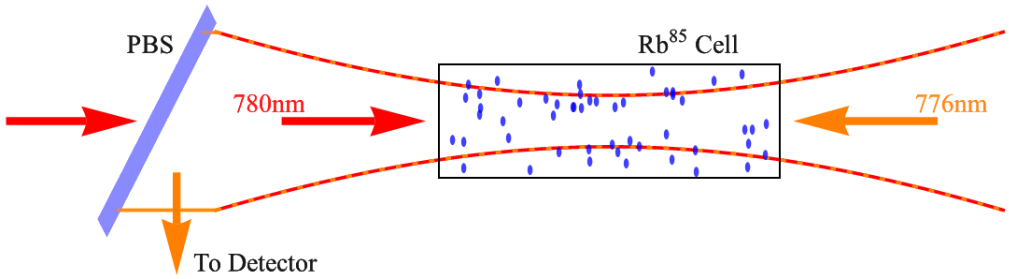

Figure 5.3: Two-Photon Spectroscopy in the blue light experiment: Two counter-propagating beams at 780nm and 776nm are circularly polarised with the same handedness and focussed into a heated cell of Rb^{85}. Inside the cell the beams are absorbed on a two-photon transition producing 5230nm, which is left unobserved, and 420nm light. The 776nm laser is then collimated after the cell and linearly polarised(not shown) before being seperated from the red beam by a polarising beamsplitter. The 776nm beam is then observed on a photodiode where the essentially doppler free absorption profile can be observed next to the saturated absorption spectrum of the 780nm beam generated elsewhere.

Two-photon spectroscopy utilises a similar setup to saturated absorption spectroscopy to create an absorption spectrum with significantly reduced doppler broadening. Fig. 5.3 shows two counter-propagating laser beams, in this case 780nm and 776nm, which are focussed, non-colinear, into a heated cell of Rb atoms. Inside the cell the beams are absorbed on a two-photon transition, facillitated by large detuning from intermediate atomic resonance. The two photons are absorbed simultaneously while not populating the intermediate, $5P_{3/2}$, state. This two-photon process has an entirely different behaviour than the absorption of two single photons of 780 and 776nm, which would populate the intermediate state. The rate of transfer of population via the intermediate state is determined by the rates of the individual steps while the two-photon transition has a virtual intermediate level.

Absorbing a photon from each of the two counter-propagating beams creates an absorption profile where the doppler shifts from each beam effectively cancel. Ideally two-photon spectroscopy is performed using one beam retro reflected through the sample to provide a perfectly doppler free signal but the frequencies of the 780nm and 776nm beams are close enough that only a small residual doppler shift remains. (approx 60MHz) The frequency absorbed by the atoms on the two-photon transition is then of the form

$$\omega_{780}\left(1-\frac{v_{780}}{c}\right)+\omega_{776}\left(1+\frac{v_{776}}{c}\right)\approx\left(\omega_{780}+\omega_{776}\right), \tag{5.2}$$

where v_{780} and v_{776} are the velocity class of atoms resonant with the 780nm and 776nm beams respectively. The velocity class is dependent on the detuning of the individual beams which under normal operational parameters are approximately equal.

5.3 Experiment - Gaussian Pump Beams

The first iteration of the experimental setup is illustrated in Fig. 5.4. The setup consists of two pump beams, a 780nm homebuilt ECDL, similar to the designs in [23], tuned to scan between the $5S_{1/2,F=1}\rightarrow 5P_{3/2}$ and $5S_{1/2,F=2}\rightarrow 5P_{3/2}$ transitions and a 776nm Toptica DL-100 oppositely detuned to the $5P_{3/2}\rightarrow 5D_{5/2}$ transition. A second 780nm laser used for accurate frequency measurements of both pump beams in separate frequency measurement setups. This beam was used in scanning mode across the entire Rubidium spectrum for two-photon spectroscopy measurements of the 776nm frequency and locked to the $5S_{1/2,F=2}\rightarrow 5P_{3/2,F=3\rightarrow 4}$ crossover peak for beat note measurements of the 780_{pump} frequency.

In order to achieve blue light production the two pump lasers are overlapped at a non-polarising beamsplitter after which they are circularly polarised with the same handedness and co-propagate towards a heated cell 3cm in length of Rubidium atoms at approximately 130°C (estimated using

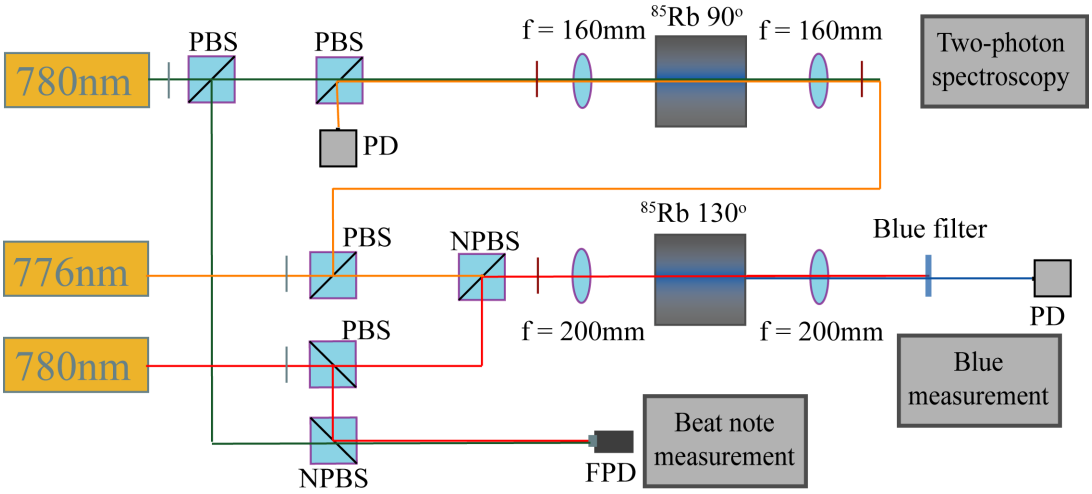

Figure 5.4: First blue light experimental setup with Gaussian pump fields. A homemade 780nm ECDL and a Toptica DL-100 776nm laser are used to generate 420nm light in a Rubidium cell heated to 130 degrees. After the cell the pump beams are then filtered out and the blue is measured on a photodiode which can be triggered at the same rate as the 780nm or 776nm lasers are scanned. A third laser at 780nm is used for accurate measurements of the two pump frequencies. The 780_{pump} frequency is measured by overlapping with the measurement 780nm beam onto a fast photodiode connected to an RF spectrometer from which the beat note of the two can be read. The 776nm frequency is measured using two-photon spectroscopy in a second heated Rb cell. The two-photon spectroscopy is performed by overlapping the 780_{meas} beam, this time scanning over the Rubidium 85 and 87 saturated absorption spectrum, counterpropagating with a small portion of the 776nm beam. The 776nm beam is then focussed onto a photodiode which is triggered at the same rate as the 780_{meas} beam scan. The position of the absorption in the 776nm beam relative to the 780nm peaks gives the detuning of the 776nm beam plus a large stark shift due to the necessity in focussing the beams into and heating in the two-photon cell. Half waveplates are shown in grey. Quarter waveplates are shown in dark red.

the Beer-Lambert law) which can be converted to an approximate vapour pressure (using simple energy equivilance) of 9 $\times 10^{-4}$mbar. This temperature and pressure combination was previously determined to give optimum

output of coherent blue beam power. The combined beam is weakly focussed by a 200mm lens into the cell producing a focus inside the cell of 8.3μm. When all factors were optimized a maximum blue power of 1.2mW was observed, broadly similar to the results in [11]. In the cell the pump beams are absorbed on a direct two-photon process with a virtual intermediate state. 5.23μm light is produced, which is absorbed by the cell walls and therefore not observed. The last link in the FWM process produces both 420nm fluorescence and a coherent beam. The blue beam is separated from the NIR pump beams by either a blue filter or a Dichroic mirror depending on the measurement being performed.

For the first experiment the pump beams are filtered from the blue which is then observed on a photodiode triggered at the same rate as both pump beams are scanned. An example of this measurement is shown in Fig. 5.5. This figure shows the blue output (in blue) on the photodiode when the 780_{pump} laser is set to scan between the doppler broadened sections in the saturated absorption spectrum shown in red.

The frequency of the 776nm laser was measured using two-photon spectroscopy as described above. To do this 5 mW of the 776nm light was separated from the main beam at a polarising beamsplitter, done before this light was joined with the 780_{pump}. The separated light was then circularly polarised and focussed into a heated cell, 7cm in length, of Rubdium at 90°C with a 160mm lens creating a focus size of 52μm. At the same time the 780_{meas} beam was set to scan over the entire Rubidium saturated absorption spectrum and focussed into the cell using another 160mm lens, counter-propagating with the 776nm beam. This lens also acted as a collimator for the 776nm light after exiting the cell. The 776nm beam is linearly polarised after the cell and seperated from the 780_{meas} beam by a polarising beam splitter after which the absorption is monitored on a photodiode which was triggered at the same rate as the 780_{meas} scan. FWM in the cell produces an essentially doppler free absorption peak in the observed 776nm trace, an

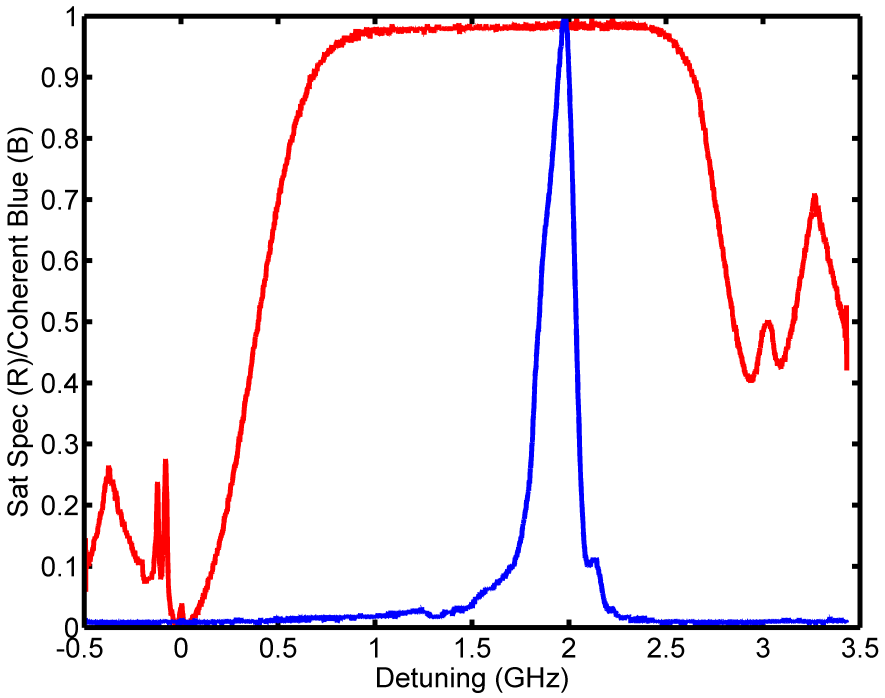

Figure 5.5: In Blue: Normalized 420nm light spectrum as measured on a photodiode when 780*pump* is set to scan over the normalized saturated absorption peaks shown in Red.

example of which is shown in Fig.5.6. It is necessary to use high intensities of measurement light to achieve an appreciable absorption signal in the 776nm beam therefore all of the 776nm measurements were subject to a large Stark shift.

The AC stark shift is the effect where a radiation field perturbs not only the populations but the energy of the levels in an atom. The AC stark light shift on a two-level atom in a time-dependent electric field is

$$\Delta\omega = \pm\frac{\Omega^2}{4\delta}, \tag{5.3}$$

where Ω is the Rabi Frequency and δ is the energy level seperation of the un-

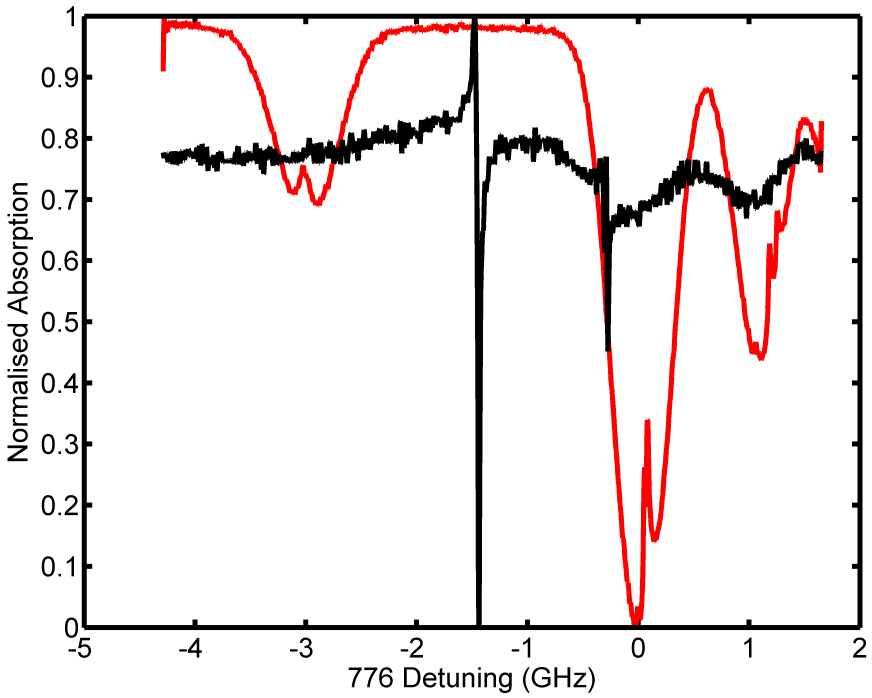

Figure 5.6: In Black: Essentially Doppler free absorption spectrum of the 776nm beam measured on a photodiode. Red: 780 saturated absorption spectroscopy.

perturbed states. For the values stated above for the two beams a stark shift of 0.5GHz was calculated. This value was added on to all 776nm frequency results.

5.3.1 3D map of coherent blue output

The graphs in Fig. 5.7 were created by recording 420nm scans similar to the one in Fig. 5.5 at multiple different 776nm detunings. These scans formed the data for the z-axis (height of blue peak) and the y-axis, 780nm detuning, which is measured directly from the distance between the peaks in the saturated absorption spectrum. Each of these scans were recorded

along with a corresponding 776nm trace similar to the one shown in Fig. 5.6. The position of the main 776nm absorption dip, relative to the 780_{meas} saturated absorption spectrum, provided the x-axis position for each of the 420nm scans.

This data shows a peak in blue output power at approximately 1.6GHz detuning for both pump beams. (negative detuning for the 776nm beam) This agrees with previous data taken in [11]. By confirming the detuning behaviour of the experiment and comparing it to previous data we were able to ensure that the experiment was working as it had been previously allowing us to directly compare later results on blue OAM conservation to preliminary results taken by Dr. Aline Vernier.

Fig. 5.8 also confirms that the position of the coherent blue peak closely follows the theoretical two-photon absorption line i.e.

$$\delta_{780} = -\delta_{776}. \tag{5.4}$$

5.3.2 Gaussian Pump Beams - Kerr Lensing

The Optical Kerr Effect is an instantaneous nonlinear effect whereby the effective refractive index of a nonlinear material changes when intense light propogates through it. While the intensities used in this experiment would not normally be considered very intense light, the high non-linearity of the dense Rb vapour allows for non-linear effects to be observed even at relatively low beam power. As a gaussian beam is more intense in the centre than on the outer edges the Kerr effect causes a greater phase change in the centre of the beam than further out creating a lensing effect. Fig. 5.9 illustrates the Kerr lensing effect.

The setup for this part of the experiment in shown in Fig. 5.10. In this experiment the pump beams are seperated from the blue through use of a Dichroic mirror. The pump beams themselves are seperated from one

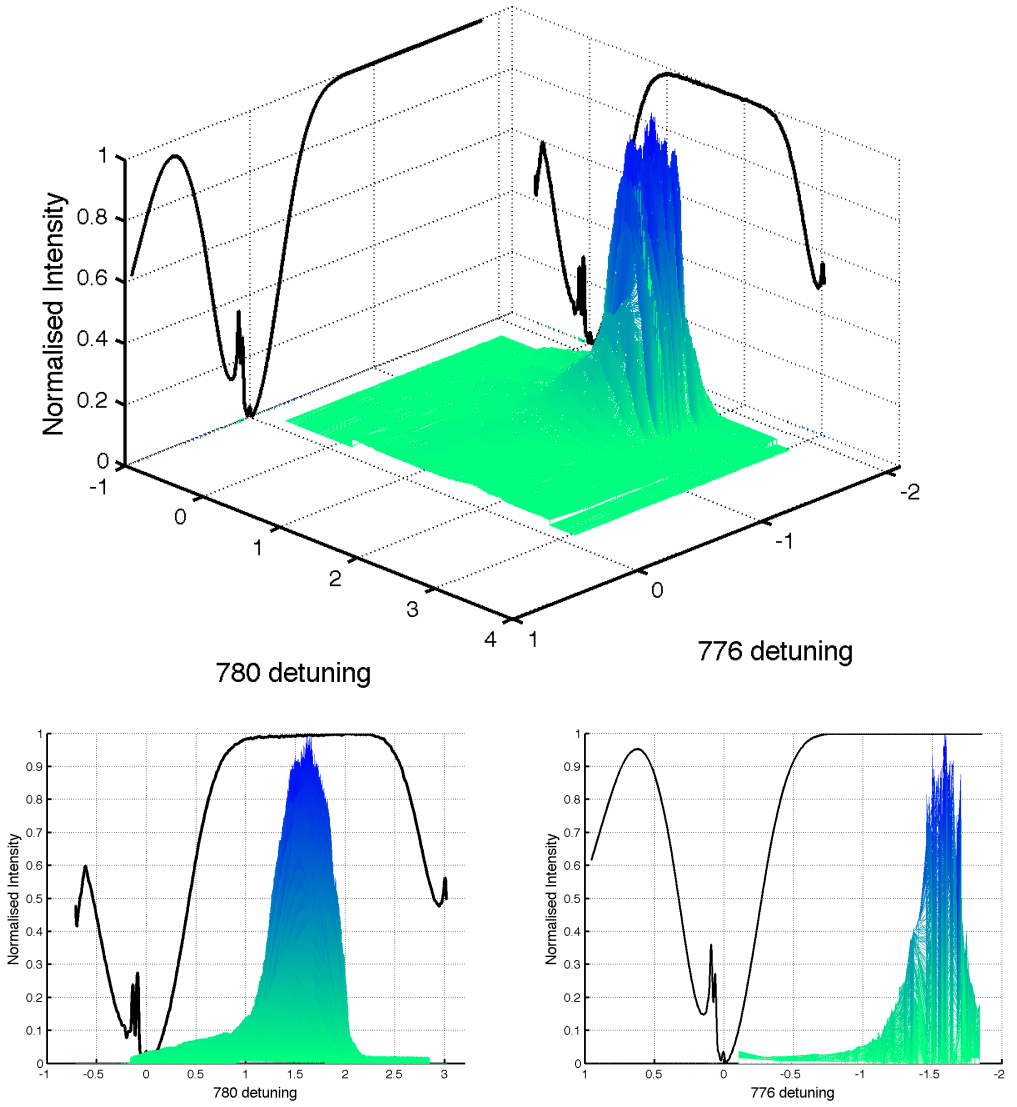

Figure 5.7: 3D map of coherent 420nm output as a function of 780nm and 776nm detuning. The graph is produced by combing 50 of the blue scans shown in Fig 5.5, providing the z-axis data and the 780nm detuning. The scans were taken at a number of different 776nm detunings, each one determined by analysis of a 776nm absorption trace similar to the one shown in Fig. 5.6. This data clearly agrees with previous results showing a peak in beam power at a detuning of approximately 1.6GHz in both beams. (-1.6GHz for the 776nm beam)

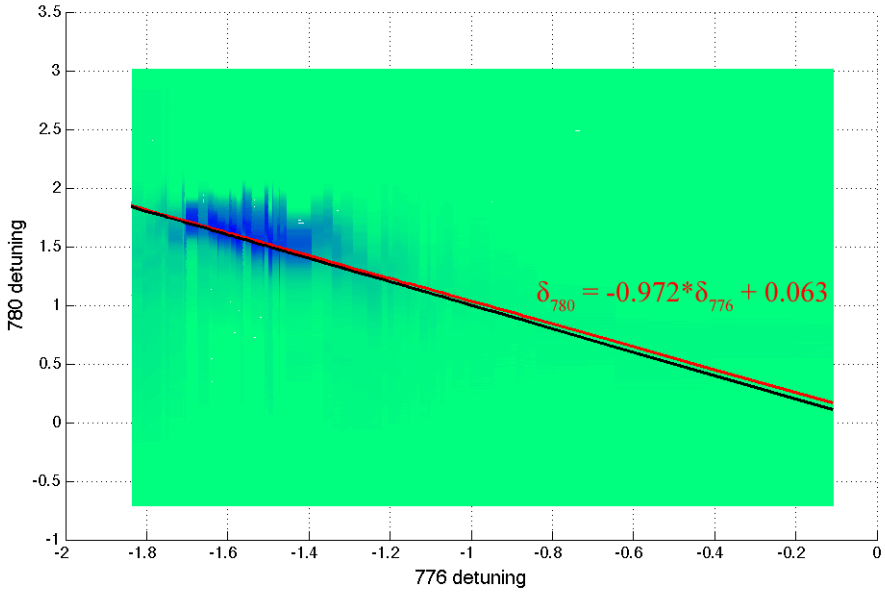

Figure 5.8: Top down view of coherent blue light output as a function of pump detunings. The linear trend of the position of the peak of each scan (shown in red) closely agrees with theoretical two-photon absorption line. (shown in black)

another by reflection from an 1800 lines cm^{-1} grating and a propogation distance of greater than 1 metre afterwards, the 780_{pump} is then observed on a CCD camera. Initial tests showed that Kerr lensing effects in the 776nm and 420nm beams were minimal and so they were not observed during this test. All Kerr measurements listed here were done on the 780nm beam.

Normalised beam waist values on the positive side of two-photon resonance and the first two on the negative side are shown in Fig. 5.11. The beam waist of the 780_{pump} laser appears to lens dramatically over a relatively small range of frequencies. As the 776nm beam is left essentially not effected by Kerr Lensing this change in beam size and propagation characteristics in the 780nm beam causes the overlap between the two beams to significantly reduce very quickly. In blue in Fig. 5.11 we can see the corresponding drop

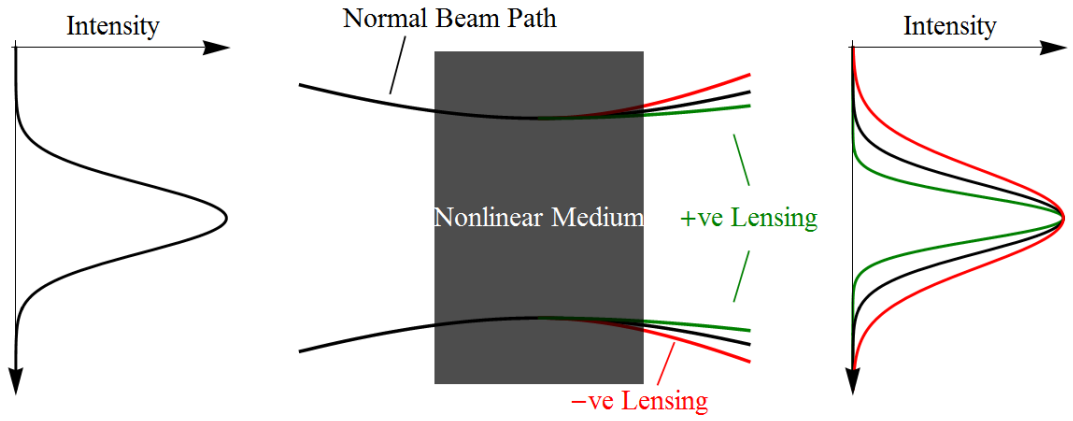

Figure 5.9: Kerr Lensing in a nonlinear medium: A non-uniform high intensity optical field propogating in a nonlinear medium will cause differing phase shifts in the light phase depending on the intensity at any point in the beam profile. The beam can experience positive or negative Kerr lensing dependning on the properties of its interaction with the medium. In our heated Rubidium cell positive and negative Kerr lensing appear for positive and negative detunings from two photon resonance. ($\Delta\omega = \pm 1.6$GHz from single photon resonance)

in blue output power and therefore FWM efficiency from this reduction in overlap.

5.3.3 Negative Kerr Lensing

On the negative detuning side of Kerr lensing we observe a dramatic distortion of the beam profile of the 780_{pump} mode again within a few 10s of MHz detuning. The beam begins to exhibit a ring like structure reminiscent of both excited p and l modes within 100 MHz of detuning. These modes were modeled as a superposition of a gaussian mode and an excited $p = 1$ mode with different focussing characteristics. (i.e. a different amount of Kerr Lensing due to the change in position of intensity maxima) The best fit modes are shown in the middle row of Fig. 5.12. The model has a degree

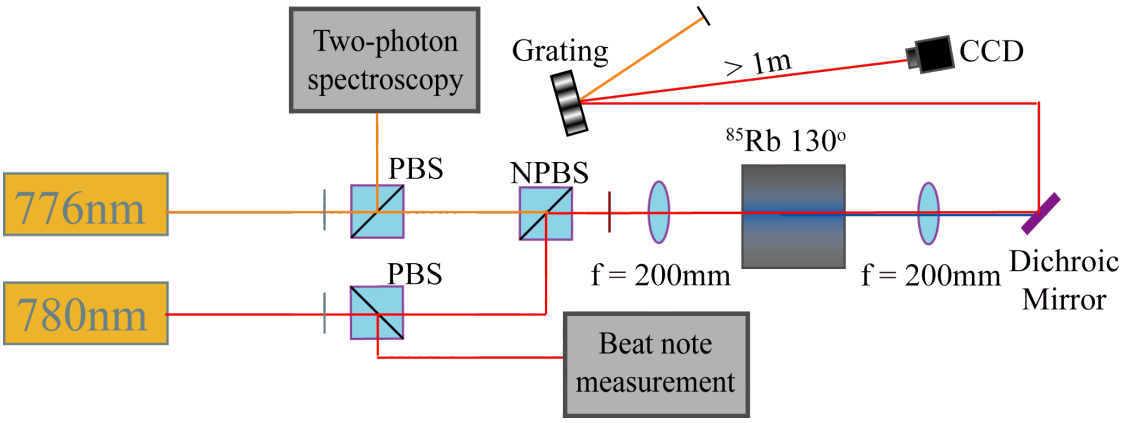

Figure 5.10: Blue Light setup for Kerr Lensing measurements. Changes from the first setup in Fig. 5.4 are the addition of a Dichroic mirror which reflects the pump beams while transmitting the blue which is left unobserved in this experiment. The two red beams are then seperated from one another via a grating and a propogation distance of > 1m. The beam profile of the 780_{pump} is then monitored on a CCD camera after a number of ND filters not shown above.

of success for most of the profiles indicating that the negative Kerr effect is somehow causing the excitation of p modes in some portion of the beam. i.e. the output modes are of the form

$$a_1 LG_{0,0}(K1) + a_2 LG_{0,1}(K2), \tag{5.5}$$

where a_1 and a_2 are the complex amplitude coefficients of each beam and K1 and K2 are some coefficients related to the Kerr effect. As of writing the differing Kerr effect in each beam is simply treated as a change to the output beam waist of the mode exiting the cell. A full analysis of the Kerr effect may be completed in the future.

The coefficients of the $p = 0$ and $p = 1$ modes are shown against the absolute value of detuning in Fig. 5.13 with $p = 0$ in black and $p = 1$ in blue. Initially close to two-photon resonance the mode is entirely in a "pure" Gaussian, $LG_{0,0}$ state. As the detuning increases the amount of pure

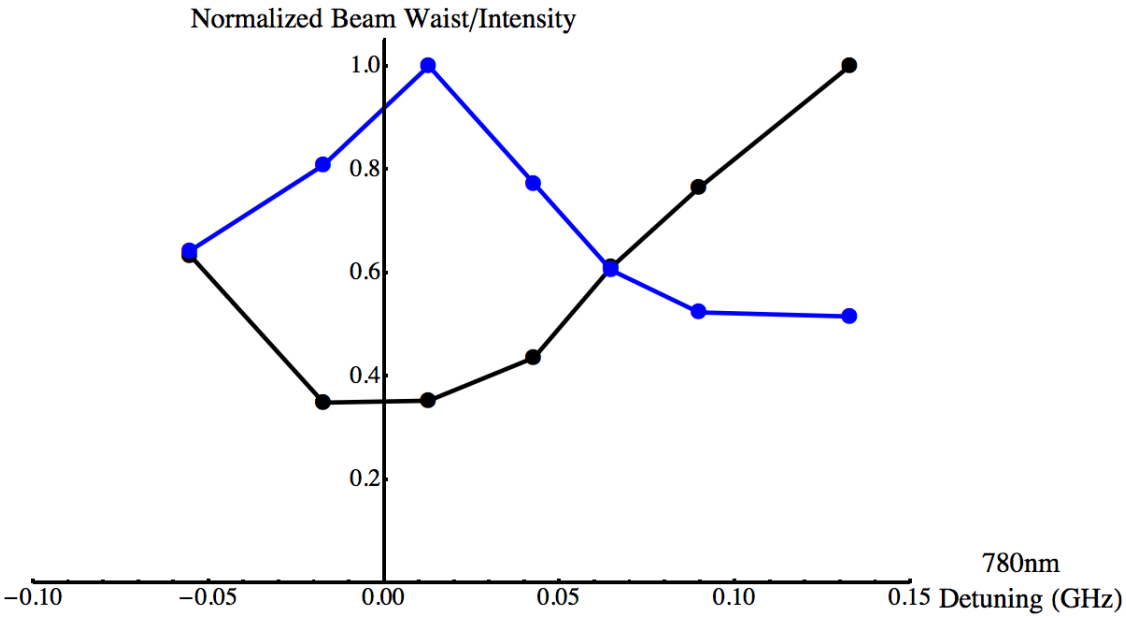

Figure 5.11: Normalized 780nm beam waist and normalized 420nm beam intensity as a function of 780nm detuning. In Black: Normalised beam waist of the 780_{pump} laser as a function of detuning from two-photon resonance. In Blue: Normalised Intensity of the coherent 420nm output as a function of 780_{pump} detuning from two-photon resonance. The beam waist of the mode changes dramatically even at relatively low detunings of 10s of MHz. This change in beam properties reduces the overlap between the two pump lasers which causes a corresponding reduction in FWM efficiency.

Gaussian decreases rapidly while a small proportion of $LG_{0,1}$ mode appears. Around 100MHz detuning there is a phase shift in the $LG_{0,0}$ mode while $LG_{0,1}$ reaches a maximum. The two modes appear to mirror one another in accordance with the phase change of each mode.

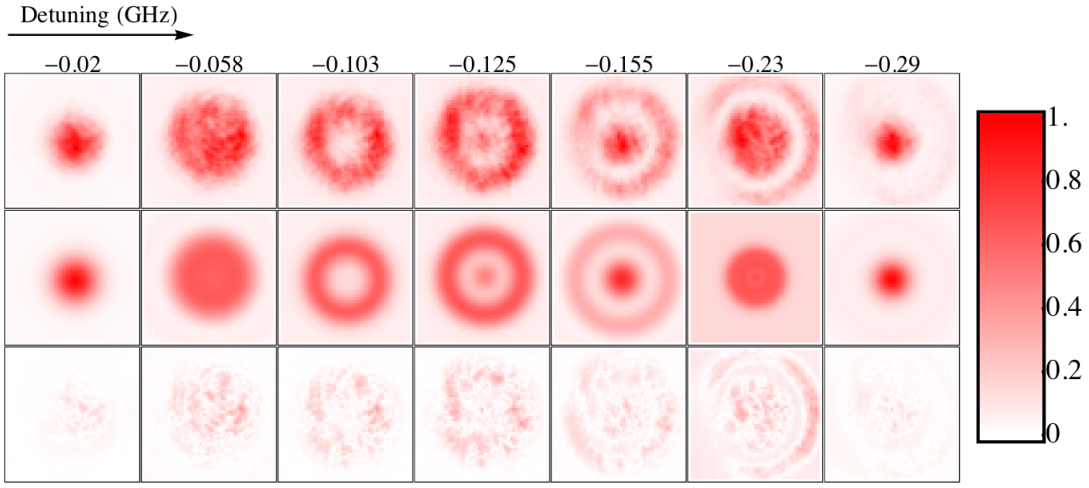

Figure 5.12: Top Row: Beam profiles of 780_{pump} beam at increasingly negative detuning from two-photon resonance. Middle Row: Best fit simulation beams made from a superposition of an $LG_{0,0}$ with a $LG_{0,1}$ where both beams have different lensing parameters due to the Kerr effect. Bottom Row: Residuals of the fit.

5.4 Laguerre-Gaussian Beams in the Blue Light

As FWM is a phase-matched process this makes the blue light experiment ideal for investigation of phase dependent light-atom interaction. The spatially varying phase of Laguerre-Gauss (LG) modes is particularly appealing when investigating phase-dependent effects, as these eigenmodes of propagation are characterised by an axial vortex line which can easily be visualised on a CCD camera in real time. Additionally the efficiency of conversion in this experiment allows us to evaluate higher order LG modes which exhibit a much lower conversion efficiency to the blue at higher l states. As discussed previously LG modes have an azimuthal phase structure, $e^{il\phi}$, associated with an orbital angular momentum (OAM) of $l\hbar$ per photon [24]. Conervation and storage of OAM has been observed in a number of similar processes to this experiment including the entanglement of OAM modes

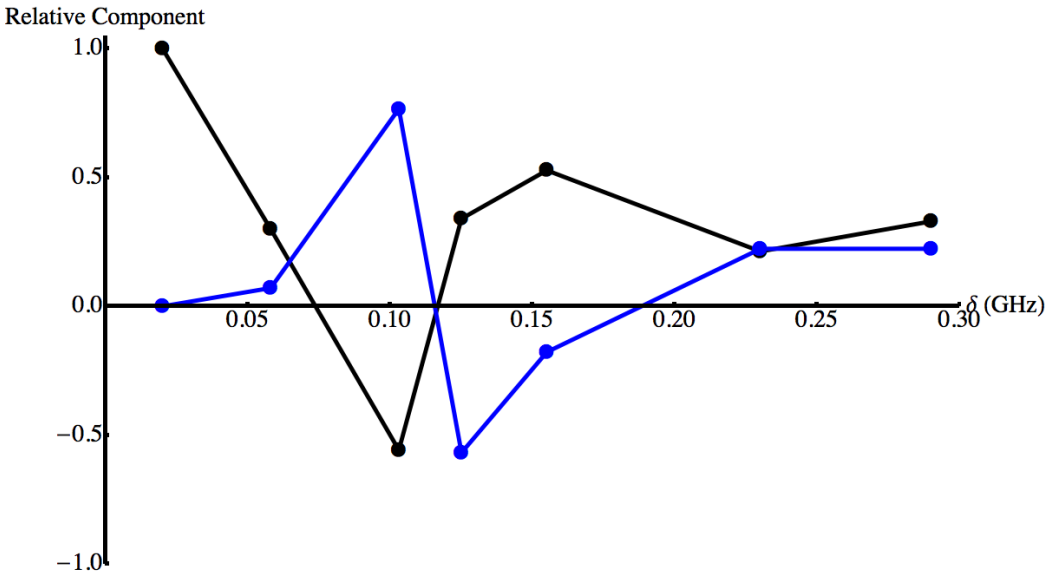

Figure 5.13: Relative component of each mode (p = 0 in black, p = 1 in blue) as a function of detuning from two photon resonance. Negative component indicates a phase change of π.

in Spontaneous Parametric Down-Conversion (SPDC) [25, 26], Second Harmonic Generation (SHG) [27], FWM in semiconductors [28], and in multi order Raman sideband generation [29]. In the SPDC case it has been shown that phase-matching applied to waves with a transverse phase-structure is responsible for the conservation of OAM [30] as long as all modes are observed [31]. More generally, parametric amplification of complex images has been realised using non-linear crystals. [32]

In atom optics, unlike in solid state processes, non-linear effects are highly efficient and can only require low light intensities such as in this experiment and others similar to it [6, 7, 11, 12]. FWM and other closed loop processes have enabled the transfer of phase information to room temperature atomic vapours [33, 34], and optical OAM has been used to manipulate the quantum state of Bose-Einstein Condensates via Raman transitions [35, 36]. In these processes, the OAM of light was transferred to the atomic media. In a

recent experiment, correlated OAM beams, were generated in a FWM process utilising Raman transitions between different hyperfine states of the same optical transition [37].

The phase-matching condition we assume to be present in the blue light experiment would suggest that $l_{780} + l_{776} = l_{5230} + l_{420}$. Our initial investigation with LG pump beams was centered around determining the distribution of the OAM states in the output modes. As the 5230nm beam could not be observed we had no direct information about its OAM state but it could be inferred through analysis of the 420nm OAM state and the fact that momentum must be conserved.

The experimental setup in this experiment is shown in Fig. 5.14. The main difference in this experiment is the addition of a spatial light modulator which is used to shape the phase and intensity profile of the pump modes into Laguerre-Gaussian modes of order $l = 0$ to 5 and $p = 0$. As the l number is increased the intensity of the pump modes will be reduced by the diffraction efficiency of the SLM. In order to combat this and other losses due to diffraction off of the SLM, a Tapered Amplifier (TA) from Toptica was added to the setup. A tapered amplifier is a solid state device that acts as an optical amplifier rather than a laser which in our setup was used to turn 21mW (13mW 776nm and 8mW 780nm) of pump power into up to 500mW out of the TA. After the TA the beam is expanded to 5mm beam waist and reflected off of the SLM encoded with the phase and intensity information of the desired mode. The desired mode is then focussed into the Rb cell, as in the first experiment, followed by the separation of the IR and blue beams are separated. A small portion of the blue and the two pump beams are sent straight to the CCD camera via a series of beamsplitters, with several ND filters in the IR beams. The rest of the blue is then sent into a Mach-Zehnder interferometer with a dove prism in one of the arms. The light ray direction inside the dove prism flips the image of the input mode in one axis turning l to $-l$. The resulting interference pattern of the l and $-l$ modes exhibits $2l$

lobes. This lobe structure allows direct measurement of the OAM content in the original blue beam. An example image is shown in Fig. 5.15.

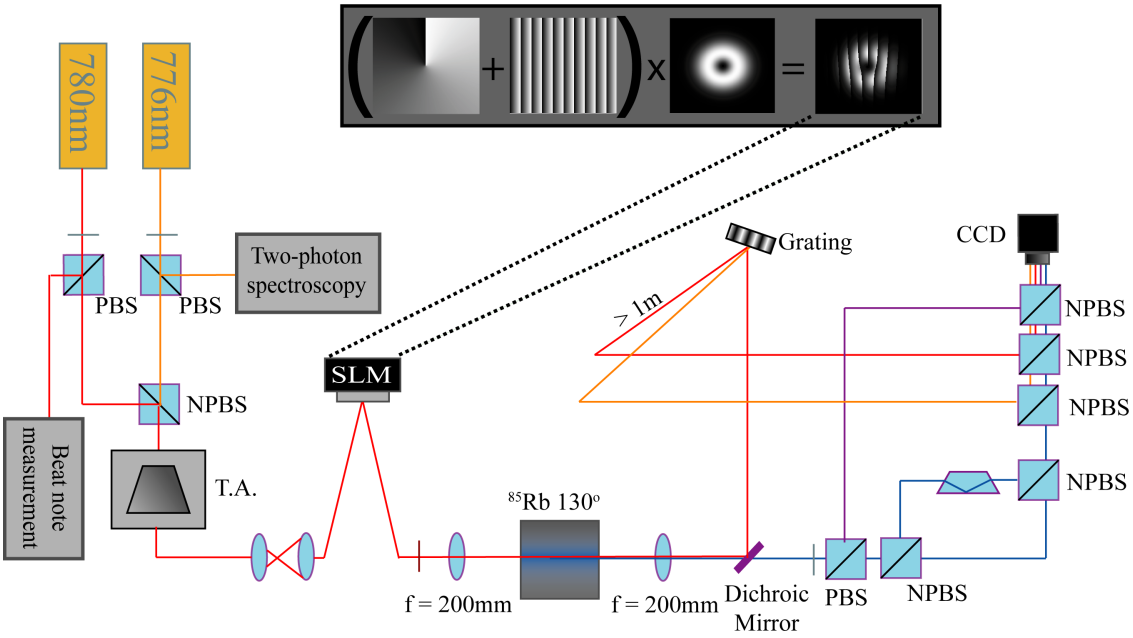

Figure 5.14: Experimental setup for the OAM conservation experiments: For this set of experiments a tapered amplifier (TA) was added to boost about 21mW(13mW 776nm and 8mW 780nm) to up to 500mW of combined pump beam power. This extra power is necessary to combat diffraction losses at the SLM and decreased conversion efficiency from LG pump beams. After the TA the beam is expanded to 5mm beam waist and diffracted off of the SLM encoded with the phase and intensity information of the desired mode between $l = 0$ and 5. The resulting mode is focused into the Rb cell as before after which 1/3 of the 420nm beam is sent directly to the CCD and the rest is sent into a Mach-Zehnder interferometer with a dove prism in one of the arms. The dove prism reverses the ray direction of the input mode effectively turning l to $-l$. The interferogram produced allows direct measurement of the OAM content of the blue beam. Finally all four beams (780_{pump},776nm, direct 420nm, and interfered 420nm) are observed on the CCD camera by way of a series of non-polarising beamsplitters.

With the four images on the CCD camera simultaneously we can now

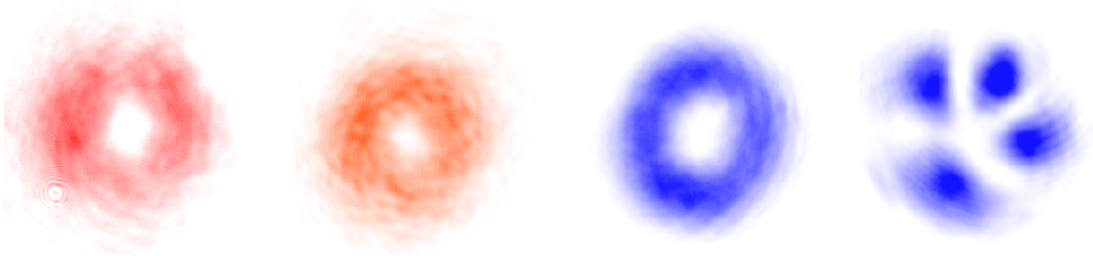

Figure 5.15: Example (colourised) data captured on CCD camera. From left to right: 780nm $l = 1$ mode in red, 776nm $l = 1$ mode in orange, 420nm unknown l mode, and 420nm interference pattern with 4 lobes indicating $l = 2$ in the blue.

directly measure the OAM content of the 420nm beam by counting the lobes in the interferogram. Also we can find the detuning that relates to minimum Kerr Lensing, i.e. most efficient FWM, by looking at the profile of the 780nm beam. The 420nm LG profiles and their corresponding interference patterns for pump modes from $l = 0$ to 5 are shown in Fig. 5.16 The number of lobes and inferred OAM content are shown in Table. 5.1. As Kerr Lensing can negatively effect amplitude overlap of the four fields all data has been taken at the position of two-photon resonance and therefore minimum Kerr lensing.

Input $l_{780} = l_{776}$	No. of Lobes	l_{420}
0	0	0
1	4	2
2	8	4
3	12	6
4	16	8
5	20	10

Table 5.1: Input pump beam OAM from $l = 0$ to 5, resulting number of lobes in the blue interferogram, and deduced OAM content in the blue.

The data from Fig. 5.16 and Table 5.1 shows a complete conversion of all of the input pump beam OAM to the 420nm mode at the output of FWM, i.e. $l l_{420} = 2 l_{780,776}$, with no visible contribution in other OAM states or

Figure 5.16: Resulting images of the blue beam and the interference pattern from the interferometer for input OAM from $l_{780,776} = 1$ to 5. The interference pattern consistently shows a number of lobes equal to four times the input OAM in the 780 and 776 beams, therefore the OAM in the blue is consistently equal to $2l_{780,776}$

nonzero p states. This indicates that the 5230nm mode must be generated in a $l = 0$ state under our assumption that momentum must be conserved through FWM. However as the 5230nm mode is unobserved we have no direct information about the p state of this mode. To evaluate the likely state of the 5230nm mode we can consider the 3 dimensional overlap integral

$$C_{p_B,p_{IR}}^{l_B,l_{IR}} = \int_{-L/2}^{L/2}\int_0^R\int_0^{2\pi} \rho\Phi_{p_{780}}^{l_{780}*}\Phi_{p_{776}}^{l_{776}*}\Phi_{p_B}^{l_B}\Phi_{p_{IR}}^{l_{IR}}\mathrm{d}\varphi\mathrm{d}\rho\mathrm{d}z. \tag{5.6}$$

where L is the length of the cell and R is the radius of the numerical aperture of the system. The probability that the blue and NIR photons are in their respective modes is then $|C_{p_B,p_{IR}}^{l_B,l_{IR}}|^2$.

First we consider the integration over azimuthal angle, which leads to

$$\int_0^{2\pi} e^{l_{780}+l_{776}-l_B-l_{IR}\varphi}\mathrm{d}\varphi = 2\pi\delta_{l_{780}+l_{776}-l_B-l_{IR}}, \tag{5.7}$$

where δ is the Kronecker delta. This restricts the output states to those for which OAM is conserved i.e.

$$l_{780} + l_{776} = l_B + l_{IR}. \tag{5.8}$$

This conservation is confirmed by our results above.

Next we consider the z direction integral. For this overlap integral we assume the condition for the output modes that requires matched Gouy phases. For Gaussian beams the well known Boyd Criterion [38], from Spontaneous Parametric Down Conversion (SPDC) experiments, states that the maximum conversion efficiency in frequency translation process occurs when the Rayleigh ranges, z_R, of pump and output modes are equal. In usual SPDC set-ups the Rayleigh range far exceeds the crystal length removing the need for Gouy phase matching, whereas the length of our vapour cell in this setup is many times the Rayleigh range which is defined as

$$z_R = \frac{\pi\omega_0^2}{\lambda}. \tag{5.9}$$

As we presume we also require Rayleigh range matching this sets a condition of the beam waist of the output modes as a function of the waists of the input modes which we define by choice of focussing lens. The condition on the output beam waists is then

$$\omega_{420,5230} = \sqrt{\frac{\lambda_{420,5230}}{\lambda_{780}}}\omega_{780}. \tag{5.10}$$

The Gouy phase for LG and excited p modes also depends on the mode number and is given by

$$(2p+ \mid l \mid +1)\arctan(z/z_R). \tag{5.11}$$

We already have an efficiency condition on the z_R portion of the Gouy phase from the Boyd criterion above. We now theorize that maximum efficiency is achieved for matched Gouy phases which is achieved when equation 5.10 is true and therefore when

$$| l_{780} | + | l_{776} | = | l_B | + | l_{IR} | + 2p_B + 2p_{IR}, \tag{5.12}$$

assuming $p = 0$ for both pump modes at minimum Kerr Lensing. Assuming this case of maximum efficiency we would expect the 5230nm mode to be in a purely gaussian state. i.e. $l = p = 0$.

Now we consider the 2 dimensional spatial overlap integral of the 4 modes at the focus of the input beams which is

$$\int_0^R \Phi_0^{l_{780}*}(\omega_{780})\Phi_0^{l_{776}*}(\omega_{776})\Phi_0^{2l_{780,776}}(\omega_{420})\Phi_{p_{5230}}^0(\omega_{5230})\,\mathrm{d}r. \tag{5.13}$$

In this case the maximum conversion efficiency should occur when the 4 modes have the greatest amplitude overlap with one another. Fig. 5.17 shows the results of the numerical integration of the this integral for $\mathrm{p}_{5230} =$ 0 to 10.

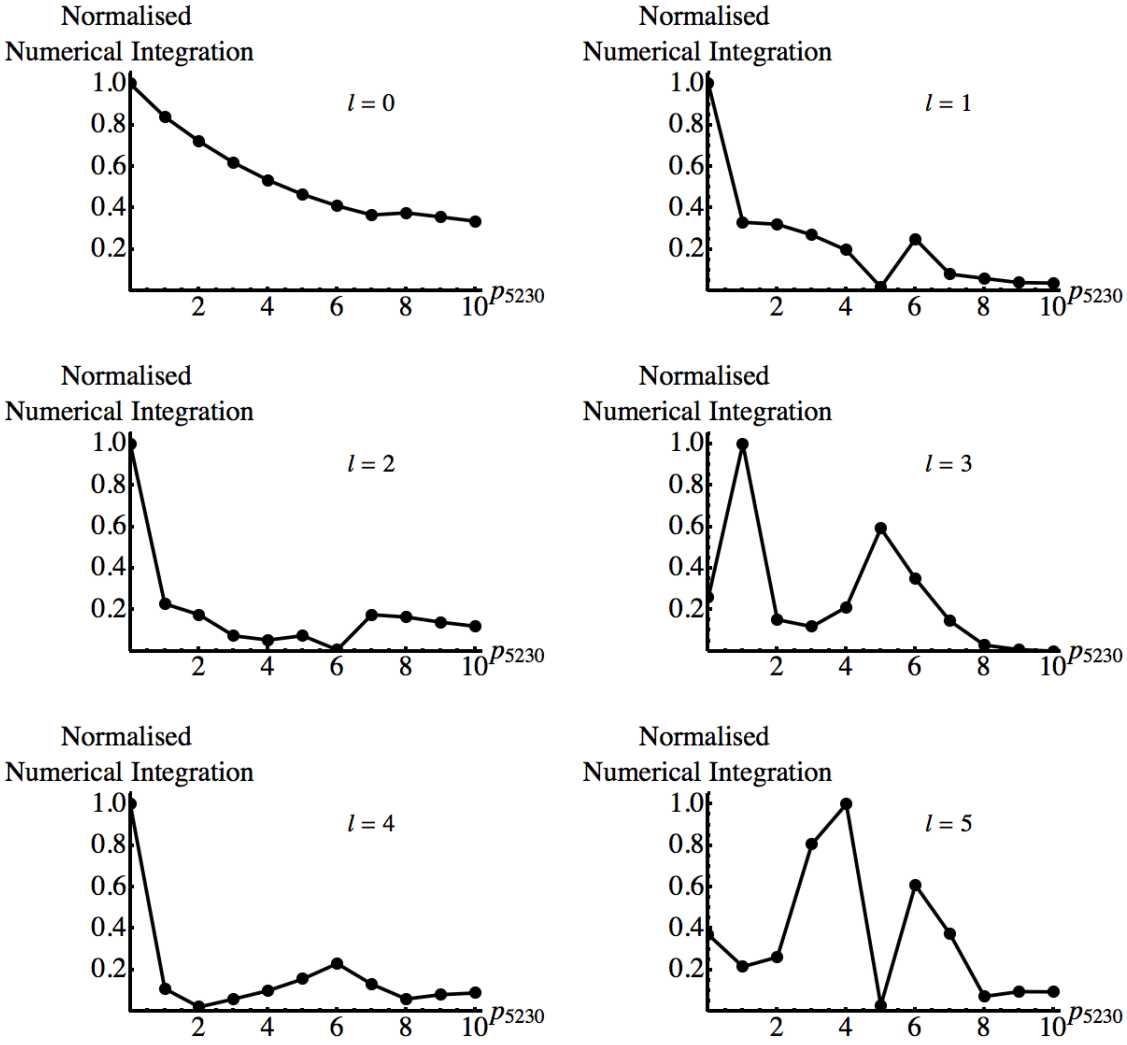

Figure 5.17: Normalised numerical integration of the four beam amplitudes for p_{5230} = 0 to 10 for pump modes with l = 0 to 5. Most of these graphs show as expected a peak at p = 0 followed by a decline in overlap with small peaks for p rings with increased overlap with the pump or blue modes. The graphs for l = 3 and l = 5 however show peaks at p = 1 and 4 respectively indicating maximum conversion efficiency for these modes in contradiction to the previous Gouy phase matching maximum efficiency prediction.

The normalized numerical integration indicates the relative likelihood of

a particular mode being produced in the four wave mixing process. In our experimental analysis we observe no p component in the blue beam but all OAM content converted to the blue. For reasons of Gouy phase matching we expect to see a large peak in the numerical integration at $p = 0$. The first 3 modes and $l = 4$ show as expected a large peak at $p = 0$ and diminishing overlap for greater p modes. All 4 of these also show a small peak at greater p values as the peak of a one of the rings in that mode has increased overlap with the OAM ring of the pump and/or blue modes. The integrals for $l = 3$ and $l = 5$ however show peaks at $p = 1$ and 4 respectively. This indicates that these modes should be most efficiently produced which is in direct contradiction to the Gouy phase matching prediction from the z direction integral. As a result of this we also looked at the amplitude overlap of $l = 0$ to 10 in the 5230 beam (with p set to zero) which is shown in Fig. 5.18 in order to compare this overlap integral technique with OAM conservation which we know to be true.

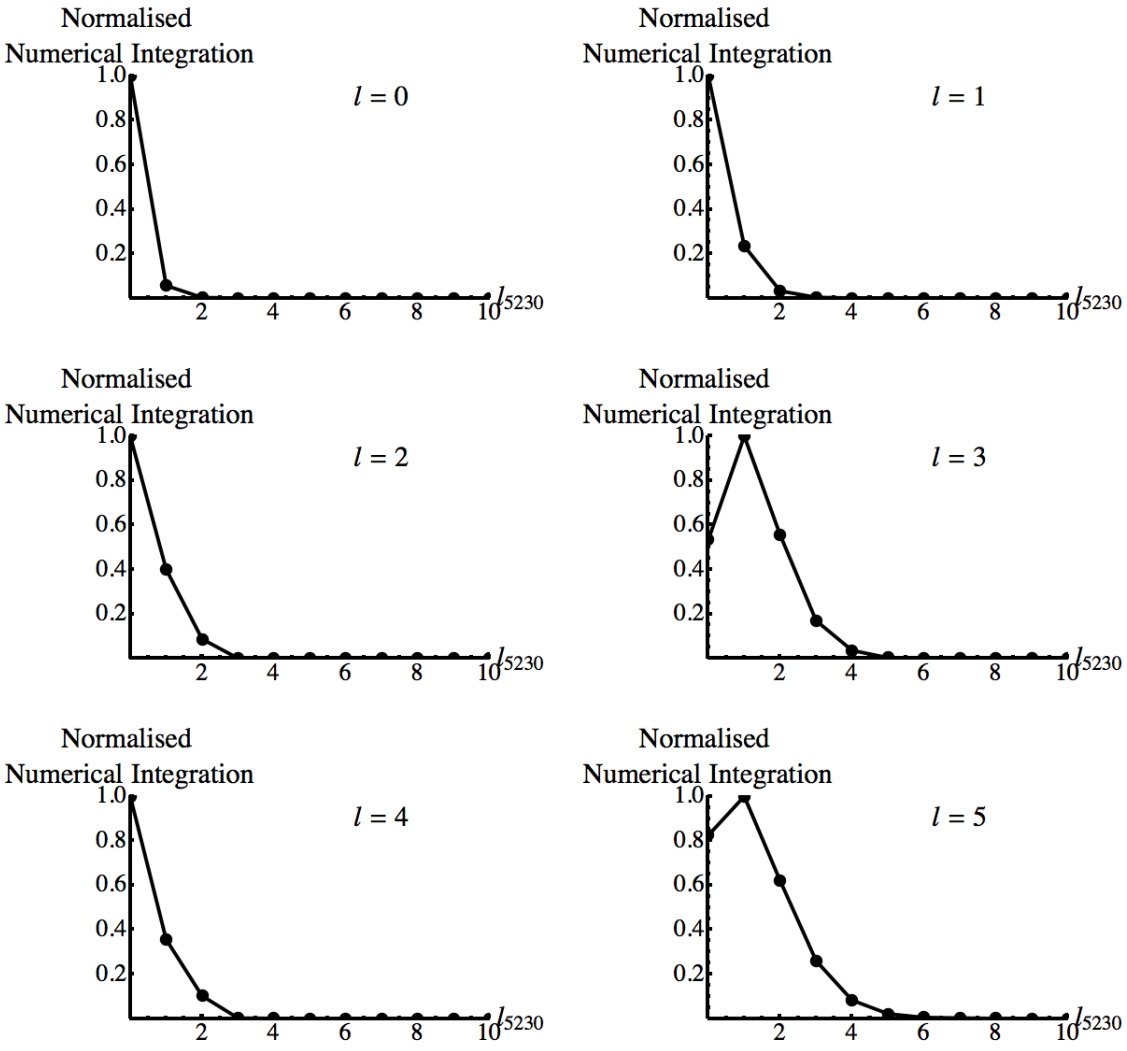

Figure 5.18: Normalised numerical integration of the four beam aplitudes for $l_{5230} = 0$ to 10 for pump modes $l = 0$ to 5. Similar to the previous results of the p index we see in most of the graphs a strong peak at $l = 0$ and diminishing overlap for greater l modes. Also as before the overlap for $l = 3$ and 5 in the pump beams shows a peak in the numerical integration for l states greater than 0.

As discussed above, experimentally we observe all OAM content being converted into the 420nm beam so similar to the prediction in p we expect

to see a large peak at $l = 0$ in the numerical integration. Again in this figure we see the first 3 modes and $l = 4$ are as expected with a large peak at $l = 0$ and quickly diminishing overlap for greater OAM states. Also again 2 modes behave differently and we see peaks, for $l = 3$ and 5, at l states greater than 0 which we know not to be possible due to the requirement for OAM conservation in the phase matched FWM process. This seems to indicate that OAM conservation and Gouy phase matching are more dominant processes than the simple 2D overlap of the 4 beam amplitudes at the focus. This highlights one of the main differences in this OAM transfer experiment to those in for example SPDC where the 2D overlap integral is a more dominant process. This Gouy phase matching dominance becomes ever more important in the analysis of the output blue modes when superpositions of OAM states are used as pump light as will be discussed in section 5.5.

5.4.1 Kerr lensing of OAM modes

A test of the Kerr lensing effects on the 780_{pump} beam was also performed for OAM pump states from $l = 1$ to 5. The results of this test as well as for $l = 0$ are shown in Fig. 5.19. In this figure we see a constant shift of between 40 to 50MHz of the position of minimum Kerr lensing when using OAM states as pump light. In addition this does not seem to vary with increasing OAM content. The reasoning behind this shift has not been fully investigated but could include the naturally less efficient conversion of LG modes to the blue meaning much less interaction with the atoms in the cell effectively causing a small stark shift of the position of two-photon resonance. Additionally the LG pump modes focus at a slightly different position in the cell. It is possible that if there was a temperature gradient across our cell that the LG modes encounter a slightly different density of atoms than that encountered by the Gaussian pump fields. Either of these differences could cause the position of minimum Kerr lensing and hence position of maximum conversion factor to differ from the Gaussian pump case.

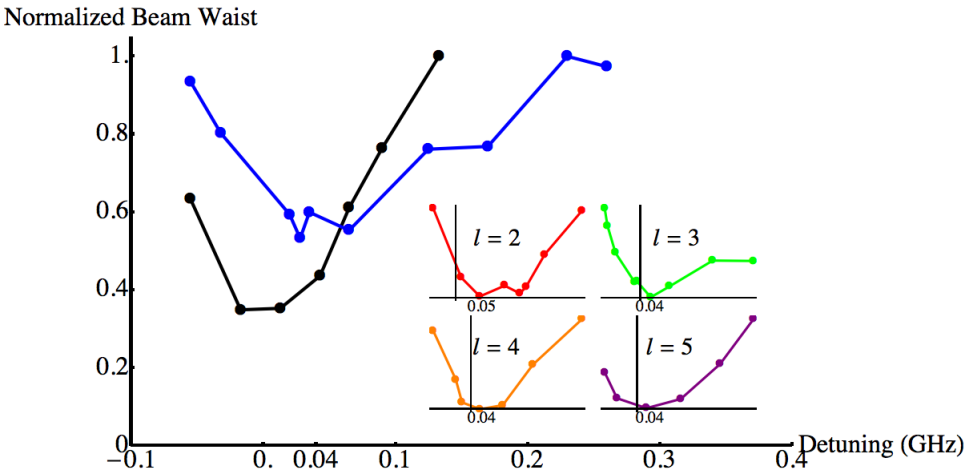

Figure 5.19: Normalised beam waist of the 780_{pump} laser as a function of detuning from two-photon resonance. Black: $l = 0$, Blue: $l = 1$, Red: $l = 2$, Green: $l = 3$, Orange: $l = 4$, Purple: $l = 5$. The position of minimum Kerr Lensing shifts by between 40 and 50 MHz for OAM pump modes.

5.5 LG Mode Superpositions in the Blue

In this part of the experiment we investigated the use of simple superpositions of Laguerre Gaussian modes, based on those shown in [39]. Specifically we take advantage of the subset of which that have a lobe like structure similar to the interference patterns generated in the pure Laguerre-Gaussian experiment. With simple superpositions we were able to investigate the phase coherence of the parametric process and show that the OAM conservation observed above is inherently quantum in nature and not merely determined by the amplitude overlap of the 4 beams. Instead we find that the interference between possible excitation amplitudes and a strong dependence on Gouy phase matching determines the most efficient output beam profiles.

In this experiment the pump modes are shaped as simple superpositions of 2 Laguerre-Gaussian modes so that the combined input field is of the form

$$E_{780}E_{776} = \frac{1}{2}(\Phi_0^l + \Phi_0^m)_{780}(\Phi_0^l + \Phi_0^m)_{776}, \tag{5.14}$$

with multiple possible absorption paths for the OAM of $2l$, $2m$, or $m + l$. Assuming no OAM transfer to the IR beam and for matching Gouy phases we expect output modes of the form

$$\begin{aligned} &E_{420} = (a_{2l}\Phi_0^{2l} + a_{2m}\Phi_0^{2m} + a_{l+m}\Phi_{p_B}^{m+l}) \\ &\text{and} \\ &E_{5230} = (b_0\Phi_0^0 + b_1\Phi_1^0), \end{aligned} \tag{5.15}$$

where the complex amplitudes a_i and b_i determine the portion of each mode in the generated beam.

The experimental setup is the same as in the Laguerre Gaussian experiment minus the tapered amplifier as it was unavailable at the time and the Mach-Zehdner interferometer was also removed as the complexity of the output OAM states ensured the OAM content could no longer be measured in this way. Table 5.2 shows the input superpositions chosen and their possible excitation paths. LG mode notation is as state previously with Φ_p^l.

Input Superposition	Possible Excitation Paths
$(\Phi_0^1 + \Phi_0^{-1})_{780,776}$	$(\Phi_0^2 + \Phi_0^{-2} + \Phi_0^0)$
$(\Phi_0^1 + \Phi_0^{-2})_{780,776}$	$(\Phi_0^2 + \Phi_0^{-4} + \Phi_0^{-1})$
$(\Phi_0^2 + \Phi_0^{-2})_{780,776}$	$(\Phi_0^4 + \Phi_0^{-4} + \Phi_0^0)$
$(\Phi_0^2 + \Phi_0^{-3})_{780,776}$	$(\Phi_0^4 + \Phi_0^{-6} + \Phi_0^{-1})$
$(\Phi_0^3 + \Phi_0^{-3})_{780,776}$	$(\Phi_0^6 + \Phi_0^{-6} + \Phi_0^0)$

Table 5.2: Input pump mode superpositions tested and their possible excitation paths in FWM

The input pump beams and output blue from the superposition experiment are shown in Fig. 5.20 along with theoretical simulations. On the top two rows in red we see the images of the input modes used and a simulation

of them. On the bottom two rows in blue we see the experimental output blue modes and the theoretical modes calculated using a fitting program. The fitting program takes the believed OAM and p content of the output modes and fits the experimental data, i.e. images of superposition modes, with the known constituent parts of the output mode and finds the relative proportion of each component that make up the output. At first glance the output modes appear to not just be a simple superposition of the possible excitation paths but have a more complex structure. We note an interesting similarity with pattern formation, where certain superpositions of OAM modes are favoured due to their overlap integral [40].

Column 3 of Table 5.3 shows the calculated composition of these output modes from the fitting program. We observe that the output mode does indeed contain only OAM states from within the possible excitation paths but also we observe a non-zero p component in the $m + l$ states. We theorize this p component to be due to the Gouy phase matching term in the z-integral of the overlap function. The Gouy phases of the possible absorption pathways and calculated output blue modes are shown in Table 5.4, these clearly show that the extra p component scales such that the Gouy phases on the output channel balance with the phases on the input channel. This Gouy phase balancing gives further evidence to the likelihood of the 5230nm mode being in the pure Gaussian state.

In addition to just considering possible excitation probabilities the interference mode $m + l$ should be excited with a probability $1/2$ whereas the modes with $2l$ and $2m$ should occur with a probability of $1/4$ each. The actual excitation probabilities deviate from this as the FWM process depends on the mode-overlap in the vapour moreso than excitation probability. As a result we see a diminishing amount of the $m + l$ lower order modes as the beam size increases due to higher order input modes.

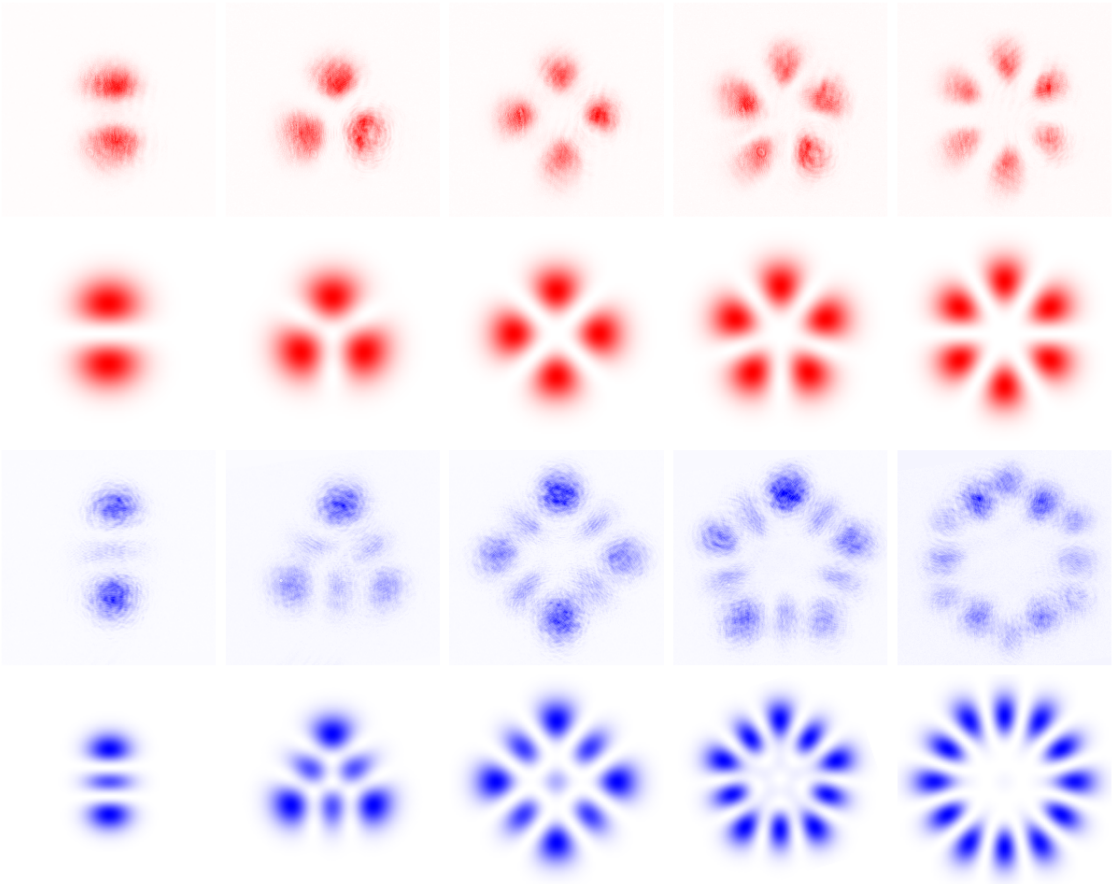

Figure 5.20: The different experimental input and output modes at the position of minimum Kerr lensing plus the ideal overlaps simulated through a numerical integration. Top Row: Experimental pump beams. (In this case the 776nm beams are displayed) 2nd row: Theoretical simulations of the input mode profiles. 3rd row: Output coherent blue beam as measured on the CCD camera at the position of minimum Kerr lensing. Bottom row: Theoretical simulations of the output blue beam using the coefficients in Table 5.3.

Input Superposition	Possible Excitation Paths	Simulated modes
$(\Phi_0^1 + \Phi_0^{-1})_{780,776}$	$(\Phi_0^2 + \Phi_0^{-2} + \Phi_0^0)$	$0.52(\Phi_0^2 + \Phi_0^{-2}) - 0.68\Phi_1^0$
$(\Phi_0^1 + \Phi_0^{-2})_{780,776}$	$(\Phi_0^2 + \Phi_0^{-4} + \Phi_0^{-1})$	$(0.66\Phi_0^2 + 0.53\Phi_0^{-4} - 0.53\Phi_1^{-1})$
$(\Phi_0^2 + \Phi_0^{-2})_{780,776}$	$(\Phi_0^4 + \Phi_0^{-4} + \Phi_0^0)$	$0.66(\Phi_0^4 + \Phi_0^{-4}) + 0.37\Phi_2^0$
$(\Phi_0^2 + \Phi_0^{-3})_{780,776}$	$(\Phi_0^4 + \Phi_0^{-6} + \Phi_0^{-1})$	$(0.7\Phi_0^4 + 0.63\Phi_0^{-6} + 0.22\Phi_2^{-1})$
$(\Phi_0^3 + \Phi_0^{-3})_{780,776}$	$(\Phi_0^6 + \Phi_0^{-6} + \Phi_0^0)$	$0.70(\Phi_0^4 + \Phi_0^{-4}) - 0.11\Phi_3^0$

Table 5.3: Input pump mode superpositions, their possible excitation paths through FWM and the theoretical simulated modes based on those observed experimentally.

	Excitation Path	Simulated modes
	$\Phi_0^1\Phi_0^1 + \Phi_0^{-1}\Phi_0^{-1} + \Phi_0^1\Phi_0^{-1}$	$0.52(\Phi_0^2 + \Phi_0^{-2}) - 0.68\Phi_1^0$
Gouy Phase:	$2 + 2 + 2$	$2 + 2 + 2$
	$\Phi_0^1\Phi_0^1 + \Phi_0^{-2}\Phi_0^{-2} + \Phi_0^1\Phi_0^{-2}$	$(0.66\Phi_0^2 + 0.53\Phi_0^{-4} - 0.53\Phi_1^{-1})$
Gouy Phase:	$2 + 4 + 3$	$2 + 4 + 3$
	$\Phi_0^2\Phi_0^2 + \Phi_0^{-2}\Phi_0^{-2} + \Phi_0^2\Phi_0^{-2}$	$0.66(\Phi_0^4 + \Phi_0^{-4}) - 0.53\Phi_2^0$
Gouy Phase:	$4 + 4 + 4$	$4 + 4 + 4$
	$\Phi_0^2\Phi_0^2 + \Phi_0^{-3}\Phi_0^{-3} + \Phi_0^2\Phi_0^{-3}$	$(0.0.70\Phi_0^4 + 0.63\Phi_0^{-6} - 0.22\Phi_1^{-1})$
Gouy Phase:	$4 + 6 + 5$	$4 + 6 + 5$
	$\Phi_0^3\Phi_0^3 + \Phi_0^{-3}\Phi_0^{-3} + \Phi_0^3\Phi_0^{-3}$	$0.70(\Phi_0^6 + \Phi_0^{-6}) - 0.11\Phi_3^0$
Gouy Phase:	$6 + 6 + 6$	$6 + 6 + 6$

Table 5.4: Excitation paths of the input pump modes and the simulated output modes based on those observed experimentally. Additionally here the Gouy phases of the individual components are shown to help illustrate its role in determining the output modes.

5.6 Summary

The data gathered during the blue light experiment has shown that the optical Kerr effect, or Kerr lensing, in a Rb vapour has a very strong response with the 780nm pump mode at relatively low detunings from ideal two-photon resonance. We see both positive lensing changing the size of the observed beam and negative lensing introducing distortions into the mode pattern causing the excitation of p modes in a portion of the beam profile. We currently have no full description as to the source of these distortions. They may be caused by the k-vector mismatch within the 780nm beam as negative lensing is applied at the focus inside the cell. We have also observed a shift in the position of minimum Kerr lensing when pump modes with Orbital Angular Momentum are introduced into the experiment. Ideally to fully model this process more data of the beam waist dependence on detuning would be taken in the future.

When the pump beams are shaped as Laguerre-gaussian modes and their simple superpositions we observe the complete conversion of all input OAM into the 420nm output of Four-Wave Mixing. Although unobserved we assume the 5230nm mode to have no OAM component due to the law of conservation of momentum. We also assume $p = 0$ in this beam as even though in some cases it has a favourable amplitude overlap in two dimensions we observe the effect of Gouy phase matching to have a larger effect in the efficiency of the output modes. We believe this is true due the longer length of our nonlinear medium compared to other frequency translation experiments. In the future a quartz cell may be used in the blue light setup in order to facilitate observation of the 5230nm beam so these suspicions can be confirmed.

The physical process by which OAM is transfered through the atomic levels has not yet been established. In [41] the transfer of orbital angular momentum is due to the generation of a population grating. Such a grating

varying in space would be the equivalent of a refractive index diffracting the incident light beams.

We have determined that Gouy phase matching plays a large role in the output mode patterns through analysis of the output mode patterns produced when the pump modes are shaped as simple superpositions of LG modes with a lobe like structure.

The work in this experiment may provide useful information for future experiments in phase dependent atomic level populations planned here at Glasgow University. In these experiments the atomic populations in a four level atom will be controlled by the phases of 4 input beams.

References

[1] A. C. Busacca, C. L. Sones, R. W. Eason, and S. Mailis. First-order quasi-phase-matched blue light generation in surface-poled ti:indiffused lithium niobate waveguides. *Applied Physics Letters*, 84(22):4430–4432, 2004.

[2] A. Jechow, A. Heuer, and R. Menzel. Highly efficient tunable blue light generation using an external cavity enhanced gain guided broad area laser diode. In *Semiconductor Laser Conference, 2008. ISLC 2008. IEEE 21st International*, pages 93–94, 2008.

[3] Dorel Guzun, Yong qing Li, and Min Xiao. Blue light generation in single-pass frequency doubling of femtosecond pulses in {KNbO3}. *Optics Communications*, 180(4-6):367 – 371, 2000.

[4] J Gao, X Yu, F Chen, X D Li, R P Yan, Z Zhang, J H Yu, and Y Z Wang. Pulsed 456 nm deep-blue light generation by acousto-optical q-switching and intracavity frequency doubling of nd:gdvo 4. *Laser Physics Letters*, 5(8):577, 2008.

[5] Koustubh Danekar, Ali Khademian, and David Shiner. Blue laser via ir resonant doubling with 71% fiber to fiber efficiency. *Opt. Lett.*, 36(15):2940–2942, Aug 2011.

[6] J. T. Schultz, S. Abend, D. Döring, J. E. Debs, P. A. Altin, J. D. White, N. P. Robins, and J. D. Close. Coherent 455 nm beam production in a cesium vapor. *Opt. Lett.*, 34(15):2321–2323, Aug 2009.

[7] Alexander M. Akulshin, Russell J. McLean, Andrei I. Sidorov, and Peter Hannaford. Coherent and collimated blue light generated by four-wave mixing in rb vapour. *Opt. Express*, 17(25):22861–22870, Dec 2009.

[8] T. Meijer, J. D. White, B. Smeets, M. Jeppesen, and R. E. Scholten. Blue five-level frequency-upconversion system in rubidium. *Opt. Lett.*, 31(7):1002–1004, Apr 2006.

[9] A. S. Zibrov, M. D. Lukin, L. Hollberg, and M. O. Scully. Efficient frequency up-conversion in resonant coherent media. *Phys. Rev. A*, 65:051801, Apr 2002.

[10] A M Akulshin, A A Orel, and R J McLean. Collimated blue light enhancement in velocity-selective pumped rb vapour. *Journal of Physics B: Atomic, Molecular and Optical Physics*, 45(1):015401, 2012.

[11] A. Vernier, S. Franke-Arnold, E. Riis, and A. S. Arnold. Enhanced frequency up-conversion in rb vapor. *Opt. Express*, 18(16):17020–17026, Aug 2010.

[12] Yong qing Li and Min Xiao. Enhancement of nondegenerate four-wave mixing based on electromagnetically induced transparency in rubidium atoms. *Opt. Lett.*, 21(14):1064–1066, Jul 1996.

[13] Lene Vestergaard Hau, S. E. Harris, Zachary Dutton, and Cyrus H. Behrooz. Light speed reduction to 17 metres per second in an ultracold atomic gas. *Nature*, 21(397):594–598, February 1999.

[14] Quentin Glorieux, Jeremy B. Clark, Alberto M. Marino, Zhifan Zhou, and Paul D. Lett. Temporally multiplexed storage of images in a gradient echo memory. *Opt. Express*, 20(11):12350–12358, May 2012.

[15] A. Szilagyi, A. Hordvik, and H. Schlossberg. A quasi phase matching technique for efficient optical mixing and frequency doubling. *Journal of Applied Physics*, 47(5):2025–2032, 1976.

[16] Y. Sasaki and Y. Ohmori. Phase matched sum frequency light generation in optical fibers. *Applied Physics Letters*, 39(6):466–468, 1981.

[17] F. Zernike. Temperature-dependent phase matching for far-infrared difference-frequency generation in insb. *Phys. Rev. Lett.*, 22:931–933, May 1969.

[18] Martin E. Smithers and Eugene Y. C. Lu. Quantum theory of coupled parametric down-conversion and up-conversion with simultaneous phase matching. *Phys. Rev. A*, 10:1874–1880, Nov 1974.

[19] N. Boeuf, D. Branning, I. Chaperot, E. Dauler, S. Guerin, G. Jaeger, A. Muller, and A. L. Migdall. Calculating characteristics of noncollinear phase matching in uniaxial and biaxial crystals. *Optical Engineering*, 39:1016–1024, April 2000.

[20] D. Budker, W. Gawlik, D. F. Kimball, S. M. Rochester, V. V. Yashchuk, and A. Weis. Resonant nonlinear magneto-optical effects in atoms. *Rev. Mod. Phys.*, 74:1153–1201, Nov 2002.

[21] Wenjiang Nie. Optical nonlinearity:phenomena, applications, and materials. *Advanced Materials*, 5(7-8):520–545, 1993.

[22] Hai Wang, David Goorskey, and Min Xiao. Enhanced kerr nonlinearity via atomic coherence in a three-level atomic system. *Phys. Rev. Lett.*, 87:073601, Jul 2001.

[23] A. S. Arnold, J. S. Wilson, and M. G. Boshier. A simple extended-cavity diode laser. *Review of Scientific Instruments*, 69(3):1236–1239, 1998.

[24] L. Allen, M. W. Beijersbergen, R. J. C. Spreeuw, and J. P. Woerdman. Orbital angular momentum of light and the transformation of laguerre-gaussian laser modes. *Phys. Rev. A*, 45:8185–8189, Jun 1992.

[25] A. Mair, A. Vaziri, G. Welhs, and A. Zelinger. Entanglement of the orbital angular momentum states of photons. *Nature*, 412:313–316, Jul 2001.

[26] D. P. Caetano, M. P. Almeida, P. H. Souto Ribeiro, J. A. O. Huguenin, B. Coutinho dos Santos, and A. Z. Khoury. Conservation of orbital angular momentum in stimulated down-conversion. *Phys. Rev. A*, 66:041801, Oct 2002.

[27] J. Courtial, K. Dholakia, L. Allen, and M. J. Padgett. Second-harmonic generation and the conservation of orbital angular momentum with high-order laguerre-gaussian modes. *Phys. Rev. A*, 56:4193–4196, Nov 1997.

[28] Y. Ueno, Y. Toda, S. Adachi, R. Morita, and T. Tawara. Coherent transfer of orbital angular momentum to excitons by opticalfour-wave mixing. *Opt. Express*, 17(22):20567–20574, Oct 2009.

[29] J. Strohaber, M. Zhi, A. V. Sokolov, A. A. Kolomenskii, G. G. Paulus, and H. A. Schuessler. Coherent transfer of optical orbital angular momentum in multi-order raman sideband generation. *Opt. Lett.*, 37(16):3411–3413, Aug 2012.

[30] Sonja Franke-Arnold, Stephen M. Barnett, Miles J. Padgett, and L. Allen. Two-photon entanglement of orbital angular momentum states. *Phys. Rev. A*, 65:033823, Feb 2002.

[31] Clara I. Osorio, Gabriel Molina-Terriza, and Juan P. Torres. Correlations in orbital angular momentum of spatially entangled paired photons generated in parametric down-conversion. *Phys. Rev. A*, 77:015810, Jan 2008.

[32] Peter M. Vaughan and Rick Trebino. Optical-parametric-amplification imaging of complex objects. *Opt. Express*, 19(9):8920–8929, Apr 2011.

[33] R. Pugatch, M. Shuker, O. Firstenberg, A. Ron, and N. Davidson. Topological stability of stored optical vortices. *Phys. Rev. Lett.*, 98:203601, May 2007.

[34] Vincent Boyer, Alberto M. Marino, Raphael C. Pooser, and Paul D. Lett. Entangled images from four-wave mixing. *Science*, 321(5888):544–547, 2008.

[35] M. F. Andersen, C. Ryu, Pierre Cladé, Vasant Natarajan, A. Vaziri, K. Helmerson, and W. D. Phillips. Quantized rotation of atoms from photons with orbital angular momentum. *Phys. Rev. Lett.*, 97:170406, Oct 2006.

[36] J. F. S. Brachmann, W. S. Bakr, J. Gillen, A. Peng, and M. Greiner. Inducing vortices in a bose-einstein condensate using holographically produced light beams. *Opt. Express*, 19(14):12984–12991, Jul 2011.

[37] A. M. Marino, V. Boyer, R. C. Pooser, P. D. Lett, K. Lemons, and K. M. Jones. Delocalized correlations in twin light beams with orbital angular momentum. *Phys. Rev. Lett.*, 101:093602, Aug 2008.

[38] G. D. Boyd and D. A. Kleinman. Parametric interaction of focused gaussian light beam. *Journal of Applied Physics*, 39:3597, Feb 1969.

[39] S. Franke-Arnold, J. Leach, M. J. Padgett, V. E. Lembessis, D. Ellinas, A. J. Wright, J. M. Girkin, P. Ohberg, and A. S. Arnold. Optical ferris wheel for ultracold atoms. *Opt. Express*, 15(14):8619–8625, Jul 2007.

[40] G. Grynberg, A. Maitre, and A. Petrossian. Flowerlike patterns generated by a laser beam transmitted through a rubidium cell with single feedback mirror. *Phys. Rev. Lett.*, 72:2379–2382, Apr 1994.

[41] S. Barreiro and J.W.R. Tabosa. Conservation of orbital angular momentum of light in coherent four-wave mixing in cold atoms. pages 66–66, 2003.

6 | Conclusion

This thesis presents two main areas of work using Spatial Light Modulators to shape resonant light beams for use in atom optics experiments.

The first work presented here builds on the work of previous PhD student Dr Aline Vernier in building the Rubidium 87 Magneto Optical Trap at the University of Glasgow. In this thesis the background theory and experimental optimization of this MOT is presented with particular focus on preparing the MOT for use in a SPontaneous force Optical Trap. Several magnetic and optical factors are optimized in the MOT including trapping coils magnetic field strength and trap beam detuning. We obtain a maximum number of atoms of 4×10^8 at a density of 4×10^{10} atoms cm^{-3} at a temperature of 116μK.

The second part of this work covers the development and optimization of anf ultra-high density dynamic dark SPontaneous Force Optical Trap. This thesis reports on the progress of finding the optimum intensity profile for use in the SPOT as well as an anti shaping technique to isolate our Depump and Repump beams from one another. The SLM is also used to great advantage over previous works in this area by dynamically switching between beam geometries, a technique we believe to be unique in this area. A maximum peak density of 2.5×10^{12} atoms cm^{-3} was achieved with 1.2×10^8 atoms. This represents 2 orders of magnitude increase in density from MOT to SPOT. Especially of interest to us when creating this ultra high density trap was the effect of heating on the atoms which is usually present in other compression

efforts. Instead however we have found that our dynamically made SPOT does not heat the atom cloud and in fact causes a slight cooling effect bringing the atoms down to a temperature of 76μK. We believe this new trap could prove useful in many applications in atom optics such as a more efficient route to BEC retaining more atoms from the initial MOT stage and future experiments to be performed at Glasgow on phase dependencies in a four level atomic interferometer.

The last part of this thesis focusses on the use of an SLM to shape two pump beams simultaneously into Laguerre-Gaussian beams and their simple superpositions for use in a frequency translation experiment. In this experiment two beams at 780nm and 776nm were used on a two-photon transition to create 5230nm and 420nm in a phase-matched loop. In the first part of this work our attention was focussed on the distribution of Orbital Angular Momentum from pure LG modes to the output wavelengths. It was found that for simple Laguerre-Gaussian beams and also their simple superpositions as input, all OAM is converted into the 420nm beam. Through the use of simple LG beams superpositions we have discovered that the conversion efficiency is dictated by a number of factors such as the Boyd Criterium (matched rayleigh ranges), phase-matching, and momentum conservation. Additional experiments using superpositions of LG modes have shed light on the surprisingly strong effect of Gouy phase matching in dictating the produced modes through Four Wave Mixing.

A | AOM Types and Frequencies

A.1 AOM Driving Electronics and Computer Control

The control electronics in our AOM setups consist firstly of a voltage controlled oscillator (VCO), such as the ZX95-100-S+ from Mini-Circuits and similar models for other frequencies. The VCO's are either driven by a table top voltage source or an analogue output from the National Instruments DAQ card, NI USB-6218. The VCO signal is sent to a mixer such as the ZP-3LH+ from Mini-Circuits. The signal is mixed with a TTL signal generated by the USB DAQ card connected to the control computer for the experiment. Finally the signal is amplified by at least 24dB and used to drive an AOM.

AOM	**Usual Frequency**	**Use**
Crystal Technologies Inc 3080-122	58.1MHz	Trap beam double pass
Crystal Technologies Inc 3080-122	54.8MHz	Depump switching and frequency shift
NEOS AOM 24080	78.4	Repump switching and frequency shift
ISLE Optics LM120	78.4MHz	RProbe switching and frequency shift
ISLE Optics LM130	133.2MHz	Probe switching and frequency shift

Table A.1

Trans-spectral orbital angular momentum transfer via four wave mixing in Rb vapor

G. Walker,[1] A. S. Arnold,[2] and S. Franke-Arnold[1]
[1] *School of Physics and Astronomy, SUPA, University of Glasgow, Glasgow G12 8QQ, UK and*
[2] *Dept. of Physics, SUPA, University of Strathclyde, Glasgow G4 0NG, UK*
(Dated: June 15, 2012)

We report the transfer of phase structure, and in particular of orbital angular momentum, from near-infrared pump light to blue light generated in a four-wave-mixing process in ^{85}Rb vapour. The intensity and phase profile of the two pump lasers at 780 nm and 776 nm, shaped by a spatial light modulator, influences the phase and intensity profile of light at 420 nm which is generated in a subsequent coherent cascade. In particular we oberve that the phase profile associated with orbital angular momentum is transferred entirely from the pump light to the blue. Pumping with more complicated light profiles results in the excitation of spatial modes in the blue that depend strongly on phase-matching, thus demonstrating the parametric nature of the mode transfer. These results have implications on the inscription and storage of phase-information in atomic gases.

Phase-matched nonlinear optical processes include a wide range of phenomena including spontaneous parametric down-conversion (SPDC), four-wave mixing (FWM), and stimulated Raman scattering. They can be studied in dielectrics as well as in atomic media. Phase-matching, if applied to the longitudinal component of the wavevector, results in momentum correlations between the relevant light fields but it also allows the transfer of phase information. The spatially varying phase of Laguerre-Gauss (LG) modes is particularly appealing when investigating phase-dependent effects, as these eigenmodes of propagation are characterised by an axial vortex line which can easily be visualised. LG modes have an azimuthal phase structure of $\exp(il\varphi)$ associated with an orbital angular momentum (OAM) of $l\hbar$ per photon [1]. Conservation and storage of OAM has been observed in a number of processes including the entanglement of OAM modes in SPDC [2, 3], second harmonic generation [4], or FWM in semiconductors [5]. For SPDC it has been shown that phase-matching applied to waves with a transverse phase-structure is responsible for the conservation of OAM [6] as long as all modes are observed [7]. More generally, parametric amplification of complex images has been realised using non-linear crystals [8].

In atom optics, unlike in solid state processes, nonlinear effects are highly efficient and require only low light intensities. FWM and other closed loop processes have enabled the transfer of phase information to room temperature atomic vapours [9, 10], and optical OAM has been used to manipulate the quantum state of Bose-Einstein condensates via Raman transitions [11, 12]. In these processes, the OAM of light was transferred to the atomic media. In a recent experiment, correlated OAM beams, were generated in a FWM process utilising Raman transitions between different hyperfine states of the same optical transition [13]. Here we report a FWM process that transfers the OAM of the pump light – via the atomic medium – to light at the opposite end of the visible spectrum.

We recently demonstrated the highly efficient generation of up to 1.1mW of coherent 420 nm blue light by enhanced frequency up-conversion in Rb vapour [14], while similar experiments have been performed by a number of other groups in Rb [15–17] and Cs [18]. The blue light generation relies on two near-infrared (NIR) pump lasers at 780 nm ($5S_{1/2}$–$5P_{3/2}$) and 776 nm ($5P_{3/2}$–$5D_{5/2}$). The atoms can subsequently decay in a cascade via $6P_{3/2}$, generating coherent infrared (5.23 μm) and blue (420 nm) light (^{85}Rb level scheme in Fig 1). We investigate phase-matching in the context of the FWM process by illuminating the atomic medium with pump light in various LG modes and some of their simple superpositions.

Any image, including the profile of our pump and generated light beams, can be described in terms of a superposition of LG modes $\Phi_p^l(x,y,z)$, where p and l denote the number of radial nodes and the winding number, respectively. The normalised LG modes are given by:

$$\Phi_p^l = \sqrt{\frac{2p!}{\pi\,(|l|+p)!}}\,\frac{1}{w(z)}\left(\frac{\sqrt{2}r}{w(z)}\right)^{|l|} L_p^{|l|}\!\left[\frac{2r^2}{w^2(z)}\right] \mathrm{e}^{il\varphi} \times \mathrm{e}^{-r^2/w^2}\,\mathrm{e}^{+i(2p+|l|+1)\arctan(z/z_R)}\mathrm{e}^{-ikz}. \quad (1)$$

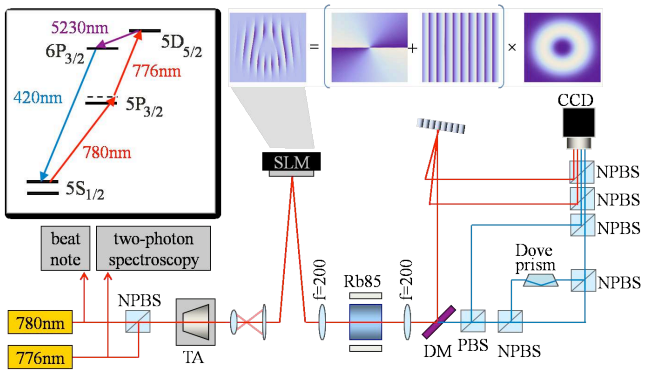

FIG. 1: Experimental set-up, with abbreviations: N/PBS (non-/polarizing beamsplitter), DM (dichroic mirror), TA (tapered amplifier), SLM (spatial light modulator) and CCD (charge-coupled device). Inset: ^{85}Rb FWM level scheme.

Here $L_p^{|l|}$ is an associated Laguerre polynomial and $w(z) = w_0\sqrt{1+z^2/z_R^2}$ for a beam waist w_0, with a Rayleigh range $z_R = \pi {w_0}^2/\lambda$. For simplicity we restrict ourselves to images represented by pure LG modes and their simple superpositions in order to show that intensity and phase information can be transferred via a FWM process from the pump light to the generated blue light.

All theoretical considerations are based on a simple phase-matching approach, without including a full description of the propagation equations, and in particular effects due to absorption and Kerr lensing of driving and generated fields which become important in the vicinity of single photon resonances [14].

FWM leads to the generation of blue and infrared light under four photon resonance. The efficiency of the process is determined by the overlap of the four light amplitudes of the two pump lasers and the generated blue (B) and infrared (IR) light, $E^*_{780}E^*_{776}E_{\rm B}E_{\rm IR}$. In our experiment, the mode profiles of the input lasers are chosen by diffraction off a spatial light modulator (SLM), and we only investigate pump modes with $p = 0$. Any output mode profile can be represented as a suitable superposition of LG modes with a given waist w_0.

The probability amplitude to generate a specific combination of a blue and an infrared photon in modes $\Phi^{l_{\rm B}}_{p_{\rm B}}$ and $\Phi^{l_{\rm IR}}_{p_{\rm IR}}$ is given by the overlap with the pump profiles,

$$C^{l_{\rm B},l_{\rm IR}}_{p_{\rm B},p_{\rm IR}} = \int_{-L/2}^{L/2}\int_0^R\int_0^{2\pi} \rho\, \Phi^{l_{780}}_{p_{780}}{}^*\, \Phi^{l_{776}}_{p_{776}}{}^*\, \Phi^{l_{\rm B}}_{p_{\rm B}}\, \Phi^{l_{\rm IR}}_{p_{\rm IR}}\, d\varphi\, d\rho\, dz, \tag{2}$$

where L is the length of the vapour cell and R the numerical aperture of the system. The probability that blue and IR photons are in the respective modes is then $|C^{l_{\rm B},l_{\rm IR}}_{p_{\rm B},p_{\rm IR}}|^2$. We note an interesting similarity with pattern formation, where certain superpositions of OAM modes are favoured due to their overlap integral [19].

Inserting the LG modes (1), and integrating over the azimuthal angle leads to

$$\int_0^{2\pi} {\rm e}^{i(l_{776}+l_{780}-l_{\rm B}-l_{\rm IR})\varphi} d\varphi = 2\pi\delta_{l_{776}+l_{780}-l_{\rm B}-l_{\rm IR}},$$

where δ is the Kronecker delta. This restricts the output modes to those for which the OAM is conserved,

$$l_{776} + l_{780} = l_{\rm B} + l_{\rm IR}.$$

A further condition for the output modes results because the largest conversion efficiency requires matched Gouy phases, which is mathematically linked to the integration over z in (2). For Gaussian beams the well-known Boyd criterium [20] states that the conversion efficiency in frequency translation processes is maximised when the Rayleigh ranges z_R of all involved beams are equal. In usual SPDC set-ups, the Rayleigh range far exceeds the crystal length, removing the need for Gouy phase matching, whereas the length of our vapour cell is many Rayleigh ranges (25 mm). Applied to our FWM scheme, the Boyd criterium implies $w_{\rm B} = w_{780}\sqrt{420/780}$, $w_{\rm IR} = w_{780}\sqrt{5230/780}$, making the IR beam waist about 3.5 times larger than that of the blue beam. However, in general the Gouy phase depends on the mode number, and for LG modes it is given by $(2p+|l|+1)\arctan(z/z_R)$. For matched Rayleigh ranges, and assuming zero order radial modes for the pump light, this results in maximum efficiency if

$$|l_{780}| + |l_{776}| = |l_{\rm B}| + |l_{\rm IR}| + 2p_{\rm B} + 2p_{\rm IR}.$$

The IR beam is unobserved in the experiment, but OAM conservation and Gouy phase matching indicate it is mainly generated in the fundamental Gaussian mode. The components of the blue light in a given mode $\Phi^{l_{\rm B}}_{p_{\rm B}}$ are found by evaluating the overlap integral (2) for all allowed mode combinations. This becomes important when investigating pump light in superposition modes.

A simplified setup of the experiment is shown in Fig.1. Pump light at 780 nm and 776 nm was generated by external cavity diode lasers [21], overlapped at a non-polarising beamsplitter and fibre-coupled to a tapered amplifier (TA). The maximum output power of approximately 500 mW allowed strong nonlinear coupling, and the fibre coupled TA output ensured clean Gaussian pump modes.

The frequency of the 780 nm light was determined from its beatnote with another 780 nm laser locked to the $F = 3$ to $F' = 3, 4$ cross-over transition. The 776 nm frequency was measured with counter-propagating two photon spectroscopy in a further heated Rb cell, where the absorption of the 776 nm laser could be determined relative to the saturated absorption trace of the 780 nm laser. The frequency could then be set manually by adjusting the voltage across a piezo electric device controlling the external grating in Littrow configuration.

The overlapped pump lasers were converted to LG modes or superpositions thereof by diffraction off a suitable hologram displayed on an SLM (Hamamatsu X10468). The computer generated holograms consist of the required phase of the desired mode superimposed with that of a linear diffraction grating, generating a fork dislocation as indicated in Fig. 1 for a Φ^2_0 mode. Although the SLM operates on phase only, the intensity can be shaped by modulating the amplitude of the grating. The spatially sculpted pump light was focussed into a Rb cell heated to 120°C (a vapour pressure of 9×10^{-4}mbar) and after the cell was split from the generated blue light by a dichroic mirror. The generated IR light was absorbed by the cell windows. The remaining NIR pump beams were separated using a diffraction grating followed by a propagation distance of ≈ 2.5 m.

The dense rubidium vapour acts as a strong nonlinear material and the beams are subject to Kerr lensing – the change of refractive index with input intensity. This is

particularly apparent in the 780 nm beam shows strong self-focussing and defocussing depending on the detuning. As this can negatively affect the amplitude overlap of the four light fields, especially when using spatially shaped pump lasers, all data has been taken at two-photon resonance and at minimum Kerr lensing. In a preliminary experiment we have verified that detunings of $\Delta_{780} = -\Delta_{776} = 1.6$GHz [14] indeed yield minimal Kerr lensing for Gaussian pump modes, but shift to slightly higher frequencies for higher order LG modes. Using a simple diffraction grating, rather than a fork hologram, we monitored the transmission of the Gaussian pump lasers through the Rb vapour cell, and adjusted the pump frequency combination to yield minimal Kerr lensing which is particularly noticable for the 780 nm transition. Once set the pump frequencies stayed stable throughout the experiment.

For the first part of the work, both input laser beams were shaped as LG beams with $p = 0$ and the same azimuthal number $l_{\rm NIR} = l_{780} = l_{776}$ which was varied between 0 and 5. An example of both pump output profiles shaped as Φ_0^1 is displayed in Figs. 2a and b. In order to visualise both the intensity and phase profile of the generated blue light, a third of the light was monitored on a CCD camera (Fig. 2c). The remaining blue light passed through a Mach-Zehnder interferometer containing a Dove prism in one of the arms. The Dove prism flips the image in this interferometer arm, thereby effectively reversing the OAM of the light. For blue light with a particular OAM $l_{\rm B}$, the resulting interference pattern then contains a superposition of modes with $\pm l_{\rm B}$ [22], exhibiting the characteristic $2l_{\rm B}$ lobes shown in Fig. 2d.

The blue intensity and interference profile resulting from input modes $l_{\rm NIR} = 0$ to 5 is shown in Fig. 3. Comparing the intensity profile with the theoretical profile of pure LG modes, we find that each blue mode has an OAM number of $l_{\rm B} = 2l_{\rm NIR}$. This is confirmed by the interference fringes, which display 0 to 20 lobes. This indicates that the IR light is generated in the mode Φ_0^0, which has the largest overlap with the NIR input modes. All of the OAM is transferred into the blue beam with no observable contribution in other OAM states.

In the second part of our work we investigated the phase coherence of the parametric process, showing that OAM conservation is inherently quantum in nature. For the pure LG modes one may argue that the blue output modes are solely determined by the intensity overlap with the input light. Instead we find that interference between the excitation amplitudes determines the output modes. This becomes apparent by shaping the pump beam profiles as superpositions of two LG modes, with OAM values l and m [22]. The combined input field is

$$E_{780}E_{776} = \frac{1}{2}(\Phi_0^l + \Phi_0^m)_{780}(\Phi_0^l + \Phi_0^m)_{776},$$

with multiple absorption paths in the initial two-photon absorption, allowing a potential OAM transfer of $2l$, $2m$, or $m + l$. Again, assuming that no OAM is transmitted to the infrared beam, $E_{\rm IR} = (\Phi_0^0)_{\rm IR}$, and for modes with matching Gouy phases, we expect a blue output mode

$$E_{\rm B} = \left(u_{2l}\Phi_0^{2l} + u_{2m}\Phi_0^{2m} + u_{l+m}\Phi_{|m|+|l|-|m+l|/2}^{m+l}\right)_{\rm B}, \quad (3)$$

where the complex amplitudes u_i depend on the mode-overlap as calculated from (2).

For this part of the experiment the TA was removed from the set-up to further limit the amount of Kerr lensing. We also omitted the Mach-Zehnder interferometer, because phase structure is inherently present in the overlap of different superposition modes.

Fig. 4 shows the observed profile of the pump modes set to 5 different superpositions (in column a), and the generated blue light (in column c). Simulations of the pump modes and the anticipated blue modes are shown in columns b) and d). Here, the anticipated composition of the blue light was evaluated by demanding OAM conservation and Gouy phase matching (3), and is shown in blue text.

We find good agreement between experiment and simulation, confirming the importance of OAM conservation and matched Gouy phases for the studied FWM process. In particular we find that the generated mode patterns cannot be explained simply from the intensity overlap of pump and generated light, but that phase-matching and amplitude interference play a crucial role. We always observe a non-zero p component in the mode corresponding to a transfer of $l + m$ units of OAM from pump to blue

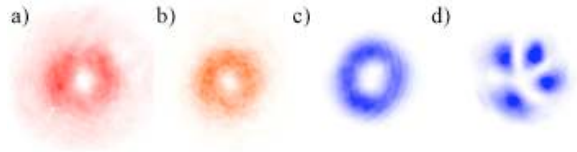

FIG. 2: Evidence of OAM transfer: Example CCD data at maximum blue intensity and minimum Kerr effects for Φ_0^1 input modes at 780 nm (a) and 776 nm (b). Resulting intensity profile (c) and interferogram (d) at 420 nm. Both c) and d) are consistent with a blue Φ_0^2 mode.

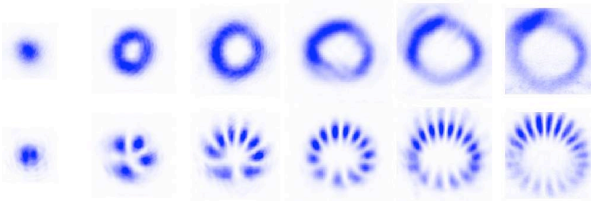

FIG. 3: OAM transfer from IR pump light with $l_{\rm NIR} = 0 \rightarrow 5$ to blue light at 420 nm beams, with intensity profile (top) and interferograms (bottom) consistent with $l_{\rm B} = l_{780} + l_{776}$.

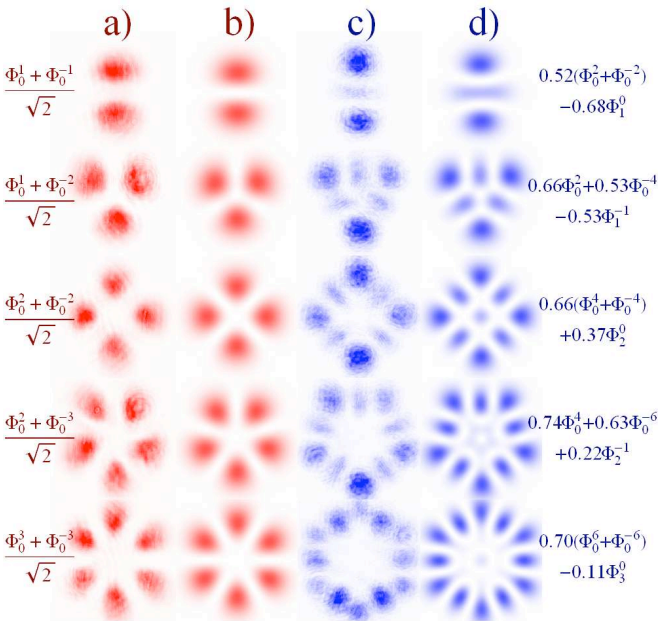

FIG. 4: Phase transfer of superposition modes: Experimental realisation of the pump superposition modes detailed as red text (a) and corresponding observed blue output modes (c). Theoretical simulation of pump modes (b) and anticipated output modes detailed as blue text (d).

light, corresponding to an excitation of $l\hbar$ on the 780 nm transition and $m\hbar$ on the 776 nm transition, or vice versa. Just considering the excitation probabilities, the interference mode $m+l$ should be excited with a probability of 1/2, whereas the modes with $2l$ and $2m$ should occur with a probability of 1/4 each. The actual excitation probability deviates from this, as the FWM process depends on the mode-overlap in the vapour.

In conclusion we have observed the transfer of the combined OAM of the NIR pump light to the coherent blue light at 420 nm via FWM in a ^{85}Rb vapour, leaving the unobserved IR transition in the fundamental Gaussian mode. We have demonstrated this for pump beams in LG modes with $l_{\mathrm{NIR}} = 0 \rightarrow 5$, which generated blue LG modes with $l_{\mathrm{B}} = 2l_{\mathrm{NIR}}$. We explain the fact that the OAM is not split between the generated blue and IR light by the large difference in waists, which maximises the mode overlap in the FWM process for all OAM in the blue.

Through the use of simple superpositions of LG beams as input modes we have illustrated the parametric nature of the process. We have noted that Gouy phase matching of LG modes determines not only the ideal beam waists of the generated modes, but also favours modes that conserve mode number. We have successfully predicted the output modes as those which obey OAM conservation and have matched Gouy phases. A more detailed description would require the propagation of the light modes, in particular in cases where Kerr lensing is not negligible, and experimental access to the generated IR light.

The observed effects are not restricted to light carrying OAM but should apply to all phase information inherent in the pump light. The described process should allow the conversion of phase information from a given input frequency to a completely different frequency.

We are grateful for useful discussions with Erling Riis and preliminary experiments by Aline Vernier. SFA acknowledges financial support by the European Commission via the FET Open grant agreement Phorbitech FP7-ICT-255914.

[1] L. Allen, M. W. Beijersbergen, R. J. C. Spreeuw, and J. P. Woerdman, Phys. Rev. A **45**, 8185 (1992).
[2] A. Mair, A. Vaziri, G. Weihs, and A. Zeilinger, Nature **412**, 313 (2001).
[3] D. P. Caetano, M. P. Almeida, P. H. Souto Ribeiro, J. A. O. Huguenin, B. Coutinho dos Santos, and A. Z. Khoury, Phys. Rev. A **66**, 041801 (2002).
[4] J. Courtial, K. Dholakia, L. Allen, and M. J. Padgett, Phys. Rev. A **56**, 4193 (1997).
[5] Y. Ueno, Y. Toda, S. Adachi, R. Morita, and T. Tawara, Opt. Express **17**, 20567 (2009).
[6] S. Franke-Arnold, S. M. Barnett, M. J. Padgett, and L. Allen, Phys. Rev. A **65**, 033823 (2002).
[7] C. I. Osorio, G. Molina-Terriza, and J. P. Torres, Phys. Rev. A **77**, 015810 (2008).
[8] P. M. Vaughan and R. Trebino, Opt. Express **19**, 8920 (2011).
[9] R. Pugatch, M. Shuker, O. Firstenberg, A. Ron, and N. Davidson, Phys. Rev. Lett. **98**, 203601 (2007).
[10] V. Boyer, A. M. Marino, R. C. Pooser, and P. D. Lett, Science **321**, 544 (2008).
[11] M. F. Andersen, C. Ryu, P. Cladé, V. Natarajan, A. Vaziri, K. Helmerson, and W. D. Phillips, Phys. Rev. Lett. **97**, 170406 (2006).
[12] J. F. S. Brachmann, W. S. Bakr, J. Gillen, A. Peng, and M. Greiner, Opt. Express **19**, 12984 (2011).
[13] A. M. Marino, V. Boyer, R. C. Pooser, P. D. Lett, K. Lemons, and K. M. Jones, Phys. Rev. Lett. **101**, 093602 (2008).
[14] A. Vernier, S. Franke-Arnold, E. Riis, and A. S. Arnold, Opt. Express. **18**, 17020 (2010).
[15] A. S. Zibrov, M. D. Lukin, L. Hollberg, and M. O. Scully, Phys. Rev. A **65**, 051801 (2002).
[16] T. Meijer, J. D. White, B. Smeets, M. Jeppesen, and R. E. Scholten, Opt. Lett. **31**, 1002 (2006).
[17] A. M. Akulshin, R. J. McLean, A. I. Sidorov, and P. Hannaford, Opt. Express **17**, 22861 (2009).
[18] J. T. Schultz, S. Abend, D. Doring, J. E. Debs, P. A. Altin, J. D. White, N. P. Robins, and J. D. Close, Opt. Lett. **34**, 2321 (2009).
[19] G. Grynberg, A. Maître, and A. Petrossian, Phys. Rev. Lett. **72**, 2379 (1994).
[20] G. D. Boyd and D. A. Kleinman, J. Appl. Phys. **39**, 3597 (1968).
[21] A. S. Arnold, J. S. Wilson, and M. G. Boshier, Rev. Sci. Instrum. **69**, 1236 (1998).
[22] S. Franke-Arnold *et al.*, Opt. Express **15**, 8619 (2007).